

DYNAMICAL SIGNATURES OF DARK MATTER SUBSTRUCTURES ON TIDAL STREAMS

by

Wayne Ngan

A thesis submitted in conformity with the requirements
for the degree of Doctor of Philosophy
Graduate Department of Astronomy and Astrophysics
University of Toronto

© Copyright 2015 by Wayne Ngan

Abstract

Dynamical Signatures of Dark Matter Substructures on Tidal Streams

Wayne Ngan

Doctor of Philosophy

Graduate Department of Astronomy and Astrophysics

University of Toronto

2015

Despite the success of the Λ CDM model at describing the universe on large scales, the model’s predictions are at odds with observations on sub-galactic scales. In particular, the model predicts that a Milky-Way-sized dark matter halo should contain substructures in the form of low mass subhalos. However, there has yet to be convincing evidence that these subhalos exist.

One promising method to probe the abundance of subhalos is by their dynamical effects on tidal streams, which are elongated remnants of tidally disrupted stellar systems as they orbit around the host galaxy. Previous theoretical studies have shown that subhalos can induce longitudinal density variations (or “gaps”) along streams. Although gaps have indeed been observed in some streams, it remains unclear whether those gaps correspond to those expected from subhalos. Previous simulations used idealized models, which did not account for realistic effects that may also induce gaps along streams. In this thesis we investigate a number of these effects.

In the first chapter, we simulate streams with self-gravity, in which we successfully model the gaps caused by epicyclic overdensities, intrinsic to the orbit of a stream, rather than subhalo perturbations. We show that the two kinds of gaps are distinguishable in their length distributions.

In the second chapter, we simulate self-gravitating streams inside a realistic halo that is constructed from a high-resolution cosmological simulation. We find that streams with similar orbital apo- and pericenters can have very different morphologies which cannot be modelled in idealized halos.

In the third chapter, we simulate a collection of self-gravitating streams inside the same realistic halo in order to quantify the difference between using an idealized halo and a realistic halo. We show that the shape of the halo has a large effect on the dispersal of streams. Nevertheless, we find that many of those streams still remain cold and thin. This suggests that upcoming stellar surveys are likely to discover more streams that are suitable for probing the abundance of subhalos.

Acknowledgements

I would like to thank my thesis supervisor Prof. Ray Carlberg for his support over the past five years. What started as a discussion of the department's research topics led me to working with Ray for a very interesting short project, which afterwards became the topic of my PhD thesis. I learned a lot from Ray who has been a great mentor and an inspiration.

Aside from my supervisor, I would also like to thank the other members of my supervisory committee: Prof. Bob Abraham and Prof. John Dubinski, as well as the members of my qualifier and defense committees: Prof. Jo Bovy, Prof. Barth Netterfield, Prof. Howard Yee, and finally my external examiner Prof. Julio Navarro who was able to come all the way from the University of Victoria to attend my defense in person. I would especially like to thank John who first suggested the SCF method which is the backbone of two chapters in this thesis.

Those two chapters would not have been possible without the contributions by my collaborators in the Johns Hopkins University: Prof. Alex Szalay, Prof. Rosie Wyse, and Dr. Brandon Bozek. During my two-month long visits to JHU, they kindly provided me with the VL-2 data, advice, and hospitality. I had a great time in Baltimore.

All parallel computations in my research are performed using Sunnyvale at CITA and GPC at SciNet. I am grateful to Prof. Ue-Li Pen who continued to share his computational resources in SciNet with me after we finished a short project prior to my thesis work.

Contents

1	Introduction	1
1.1	The Dark Matter Problem	1
1.2	The Triumphs of the Λ CDM Model on Large Scales	1
1.3	The Problems of the Λ CDM Model on Small Scales	3
1.4	Tidal Streams	4
1.5	Thesis outline	5
2	Using Gaps in N-body Tidal Streams to Probe Missing Satellites	7
2.1	Motivation	8
2.2	Simulations	8
2.2.1	Models	8
2.2.2	Software and Parameters	9
2.2.3	Stream Properties	11
2.3	Method	14
2.3.1	Subhalo Mass Ranges	14
2.3.2	Gap Finding	16
2.4	Results and discussion	19
2.4.1	Gap Morphology	19
2.4.2	Gap Counting	22
2.4.3	Gap Spectrum	22
2.4.4	Observational Considerations	30
2.4.5	Subhalo Mass Limits	37
2.4.6	Other Effects	38
2.5	Chapter Summary	39
3	Simulating Tidal Streams in a High-resolution Dark Matter Halo	42
3.1	Motivation	43
3.2	Method	44
3.2.1	SCF Method	44
3.2.2	Subhalo Finding	46
3.2.3	Modeling the smooth halo	47
3.2.4	Adding Subhalos	48
3.3	Stream simulations	52
3.3.1	Progenitor and Orbit	52

3.3.2	Simulation Details	53
3.4	Results and Discussion	53
3.4.1	Decomposition Order	53
3.4.2	Densities along the Streams	58
3.5	Chapter Summary	67
4	Dispersal of Tidal Debris in a Milky-Way-sized Dark Matter Halo	71
4.1	Motivation	72
4.2	Method	72
4.2.1	VL-2 Halo and Subhalo Potentials	72
4.2.2	Spherical Halo Potential	73
4.2.3	Subhalo Finding	74
4.2.4	Stream Progenitor and Orbits	76
4.2.5	Simulation Details	77
4.3	Results	79
4.3.1	Effects of the Underlying Halo	79
4.3.2	Dispersal of Tidal Debris	81
4.3.3	The Densest Streams in the VL-2 Halos	83
4.3.4	Streams in the Local Volume	86
4.4	Chapter Summary	90
5	Conclusions and Future Work	95
5.1	Conclusions	95
5.2	Future Work	96
	Bibliography	98

List of Tables

2.1	Thirteen Subhalo Mass Ranges in Our Simulations. The upper limit cuts off at $10^8 M_\odot$ for all ranges. Columns from left to right: lower mass limit, total number and total mass in subhalos (Equation 2.3), number and mass in subhalos used in simulation after reduction by orbit (see the text).	16
3.1	Main Halo and Subhalos in the $z = 0$ Snapshot of VL-2. The total number of particles (N), total masses (M), scale radii (r_s), and virial radii (r_{vir}) of three nominal halos extracted by the halo finder, which found a total of 11,523 subhalos inside the virial radius of the main halo.	47

List of Figures

2.1	The progenitor’s orbit (dotted line) used in this chapter. The orbital plane is confined to the xy -plane. The black pixels centered at $(x, y) \approx (-30, 0)$ kpc represent an 8 Gyr old stream.	10
2.2	Top: fraction of mass enclosed in 0.103 kpc of the star cluster while orbiting the dark matter halo without any subhalos. Middle: rate of change of mass enclosed in 0.103 kpc of the star cluster (solid black) and radial position of the star cluster’s orbit (red). This shows that the star cluster experiences bursts of mass loss almost immediately after each pericentric passage. Bottom: length of the stream. This shows that the stream gets stretched and compressed depending on its orbital phase. The red and blue vertical lines correspond to the snapshots where the star cluster is at the pericenters and apocenters of its orbit, respectively. These times are selected to demonstrate the bias discussed in Section 2.4.4.	12
2.3	Tangential velocity dispersion and FWHM width along the stream at 8 Gyr. The progenitor is centered at 0 kpc, where positive and negative positions represent the leading and trailing branches of the stream, respectively. The structures in velocity dispersion and width are due to the eccentricity of the stream, as traced by the orbital distance along the stream.	13
2.4	Distribution of orbital action variables (J_r, L_z) for our stream at 8 Gyr without any subhalos. Along the entire stream with the progenitor masked out, 50,000 unbound particles were randomly selected to be placed on this map. Each pixel in this map represents the density of particles in that bin. The two symmetric lobes are the two branches of the stream. Similar plots can be found in Eyre & Binney (2011), and a plot in scaled energy and angular momentum in Yoon et al. (2011).	15
2.5	Five example filter scales for the match filter used in Carlberg et al. (2012), which has the functional form $f(t) = (t^6 - 1) \exp(-1.2321t^2)$. With a physical scale s , the integral of $f(2x/s)$ vanishes inside $-1.5s < x < 1.5s$. The roots of each filter are located at $\pm s/2$ so that the gap length is simply the distance between the roots. We search for gaps at 12 logarithmically filter scales from 0.1 to 5 kpc in order to minimize the chance of detecting the same gap at multiple scales.	18

2.6	Surface density of the smooth stream from 7 to 8 Gyr projected onto the xy -plane. The stream is then aligned to Cartesian coordinates where the horizontal axis is the offset position along the stream from the progenitor, and the vertical axis is the radial offset from the galactocentric distance of the progenitor. This is done by tracing a best fit line along the stream. For each segment in the line, the particles in between the end points of the segment are rotated such that the Galactic center points toward the $+y$ direction in this plot. Note that the vertical axis has been scaled 30 times the larger than the horizontal axis.	20
2.7	Stream with $5.8 \times 10^6 < M/M_\odot < 10^8$ subhalos from 7 to 8 Gyr, aligned to Cartesian coordinates similar to the smooth stream in Figure 2.6. Compared to the smooth stream, this Λ CDM stream shows much more structures at various scales. In general, whether by EOs (mostly inside ± 5 kpc) or by subhalo perturbations, gaps have complicated morphologies and do not even have straight edges across the width of the stream.	21
2.8	Linear densities along the smooth stream, integrated for the whole thickness of the stream, from 3 to 8 Gyr. The progenitor is centered at 0 kpc and is masked out. Shaded columns are gaps identified at 99% confidence at the scale depicted by the columns' widths.	23
2.9	Linear densities and gaps identified at 99% in the smooth stream, but integrated for only a cylinder of diameter 0.08 kpc along the central line of the stream.	24
2.10	Linear densities and gaps identified at 99% in the Λ CDM stream with subhalo masses $6.5 \times 10^4 < M/M_\odot < 10^8$, integrated for the whole thickness of the stream.	25
2.11	Linear densities and gaps identified at 99% in the Λ CDM stream with subhalo masses $6.5 \times 10^4 < M/M_\odot < 10^8$, integrate for only a cylinder of diameter 0.08 kpc along the central line of the stream.	26
2.12	Analytical (Carlberg, 2012) and simulated gap spectra. The gaps are collected from 13 simulations with independent sets of subhalos selected differentially from the mass ranges in Table 2.1. In the top panel, all gaps identified (including EOs) are included in the measured gap spectra. In the bottom panel, the gaps located within 5 kpc away from the progenitor are eliminated, and the stream lengths and ages are adjusted. The gap spectra here roughly follow the analytical prediction, but with large deviations as this is only one realization. Later in this chapter we show the median gap spectra from many realizations.	29
2.13	Analytical (Carlberg, 2012) and simulated gap spectra. The gaps are collected from single simulations which include the full ranges of subhalos. The lower limit of the mass range is labeled in each panel, and the upper limit is $10^8 M_\odot$ in all cases. In the top three panels, all gaps identified (including EOs) are included in gap spectrum. In the bottom three panels, the gaps located within 5 kpc away from the progenitor are eliminated, and the stream lengths and ages are adjusted. Compared to Figure 2.12, the simulated gap spectra here no longer follow the analytical prediction because of overlapping between the gaps.	31

2.14	Top: time evolution of the number of gaps longer than 0.34° . Each colored line represents the median of 10 realizations of an identical subhalo distribution (with $10^8 M_\odot$ as upper mass limit), and the black thick line represents the smooth stream. Bottom: the vertical dashed lines are visual guides which show that the variation of the number of gaps are correlated with the orbital phase of the stream progenitor. These plots show that the cumulative number of gaps in a stream on average is increasing in time, but instantaneously the number of gaps observable can have an even stronger dependence on the orbital phase of the stream than on the stream’s dynamical age or subhalo masses.	33
2.15	Density profiles and gaps detected at 99% confidence for the Λ CDM stream with subhalos of masses $1.5 \times 10^5 < M/M_\odot < 10^8$ at 8 Gyr, projected onto the sky. Each panel represents a stream whose number of particles have been reduced by the factor indicated and binned at 0.1° throughout. Without reduction (top panel), the stream contains about 80,000 particles. The stream retains most of its gaps even after particle reduction by a factor of eight.	35
2.16	Gap spectra from simulated streams after sky projection. Each line in the panels on the left are the median of 10 spectra of the same Λ CDM stream but with ten identical subhalos distribution of masses $1.5 \times 10^5 < M/M_\odot < 10^8$. The panels on the right are the spectra of the smooth stream. The spectra of the Λ CDM stream show presence of gaps longer than 1° , whereas the spectra of the smooth stream quickly drops off. Colored solid (dashed) lines are spectra obtained when the stream is undergoing pericentric (apocentric) passage. Each row represents the spectra after the numbers of particles in the streams have been reduced by the factor labeled. The bottom panels indicate that a high S/N detection of the stream is important for understanding the origins of gaps, otherwise the gap formation rates can be systematically biased depending on the stream’s orbital phase.	36
3.1	Comparing the magnitude of accelerations obtained from SCF ($n_{max} = l_{max} = 0$) against directly summing up the accelerations from all particles in the smooth halo. The accelerations are measured at 94,797 randomly distributed positions inside a spherical shell of $r = [15, 40]$ kpc. Top, middle, and bottom panels are the errors plotted against the (r, θ, ϕ) in spherical coordinates of the test positions.	49
3.2	Same as Figure 3.1, but with $n_{max} = l_{max} = 10$. The accelerations are accurate to $\sim 1\%$ level everywhere. Note the change in vertical scale from Figure 3.1.	50
3.3	Same as Figure 3.2, but with $n_{max} = l_{max} = 20$. The top panel shows some correlation between the force error and radial position. This correlation is expected from basis functions whose radial components are polynomials. Nevertheless, the errors remain at the 1% level, so the correlation is not a concern.	51
3.4	The cumulative distribution of the error at all the points in Figures 3.1–3.3. The $\sim 1\%$ level error is achieved more than 99% of the time for orders 10 and 20, but the errors for order 0 are much larger.	52
3.5	Two stream orbits in an SCF potential of the smooth halo using order 10 with initial positions at $(x, y, z) = (30, 0, 0)$ kpc, but with $(v_x, v_y, v_z) = (0, 120, 0)$ km s^{-1} (“Orbit 1”; top panel) and $(0, 41.0, 113)$ km s^{-1} (“Orbit 2”; bottom panel). Both are tube orbits with apo- and pericenters that roughly correspond to the inferred values of GD-1.	54

3.6	Radial coordinates of two progenitor orbits shown in Figure 3.5. Top and bottom panels show Orbits 1 and 2, respectively. These two plots show that their orbits have converged at order 10.	56
3.7	Four streams that start with the same initial conditions with Orbit 1 in the smooth halo that is constructed using different decomposition orders. The streams' overall profiles on large scales are similar, but the density fluctuations on small scales are different.	57
3.8	Rate of change in the number of particles enclosed in 0.1 kpc from the center of the progenitor as a function of time in Orbit 1. Every spike in mass loss is associated with a pericentric passage. Even though the major mass loss events occur at the same time at the same rate among all orders, the minor events do not.	58
3.9	Sky-projected surface density of the stream in Orbit 1 in the smooth halo. The projection is seen from a hypothetical observer situated in the galactic center. Since the stream is extremely narrow compared to the size of its orbit, the curvature of the stream on the sky has been subtracted, and the progenitor has been shifted to have position at 0° . Note that the width of the stream (Δw on the y-axis) is about 50 times smaller than the length of the stream.	60
3.10	Linear density corresponding to the same stream shown in Figure 3.9. The progenitor at position 0° has been masked out. Epicyclic overdensities appear as the first few spikes within about 10° on either side of the progenitor (especially noticeable at 8.2 Gyr when the stream is compressed).	61
3.11	Same as Figure 3.9, but in a lumpy halo with 3807 subhalos.	62
3.12	Linear density corresponding to the same stream shown in Figure 3.11. Compared to the smooth halo case (Figure 3.10), in a lumpy halo the stream appears clumpier with more local minima in density everywhere in the tails of the stream.	63
3.13	Sky-projected surface density of Stream 2 in the smooth halo. The projection is seen from a hypothetical observer situated in the galactic center. Compared to Figure 3.9, the streams here contain diffuse ends sometimes as wide as the length of the stream. Rather than tracing a line and subtracting their curvatures on the sky, the streams shown here are simply shifted so that the progenitors have $\phi = \theta = 0$, and then rotated so they appear roughly horizontal.	65
3.14	Linear density corresponding to the same stream shown in Figure 3.13. A line has only been traced along the regions up to 20° away from the progenitor. The progenitor at position 0° has been masked out. The density profiles show prominent density spikes near the progenitor, similar to Stream 1, but the profiles quickly fall off to the diffuse regions without many intrinsic features.	66
3.15	Same as Figure 3.13, but in the lumpy halo. The stream overall appears similar to the case in the smooth halo, but the diffuse ends of the stream are even more prominent, and sometimes even wider than the narrow part of the stream itself.	68
3.16	Linear density corresponding to the same stream shown in Figure 3.15. Similar to the case in the smooth halo, linear density is only appropriate at the regions near the progenitor where the stream is narrow. Aside from the density spikes near the progenitor, the density profile is smooth and featureless.	69

4.1	Enclosed masses of the two smooth halos used in this study. The mass of the VL-2 is computed by directly summing the masses of all the particles inside r , and the mass of the spherical halo is obtained analytically from the NFW profile. Their masses agree to within 10% for $r \lesssim 30$ kpc.	74
4.2	Eccentricities of the random orbits of the 100 streams used in each halo potential. The “outer” set contains 50 orbits whose galactocentric distances r are bounded by $10 \text{ kpc} < r < 30 \text{ kpc}$ for 10 Gyr. The “inner” set contains another 50 orbits bounded by $r < 30 \text{ kpc}$, but $r_{min} < 10 \text{ kpc}$ in 10 Gyr. The sets of orbits in the VL-2 and spherical potentials are different, but they have identical eccentricity distribution.	77
4.3	Fractions of particles enclosed in a radius 0.16 kpc of the progenitors as functions of time. Each line represents the median of 50 streams at each instant of time, where the dashed and the thick dash-dotted lines represent the lumpy halos with subhalo mass ranges indicated in solar masses. Top and bottom panels show the inner and outer sets of streams, respectively. In each case, the mass loss is primarily caused by the tidal stripping at the progenitors’ pericentric approaches, and not by subhalo shocking.	78
4.4	Hammer-Aitoff equal-area projections of 100 streams on the sky at 6 Gyr as seen from the galactic center. Each panel shows the combined surface density of particles in 0.3° cells. Top and bottom rows show the streams in a smooth spherical halo and a lumpy spherical halo with $M_{sub} > 10^7 M_\odot$, respectively. Left and right columns show the same maps, but their gray scales are adjusted to exaggerate the diffuse and dense cells, respectively. All stream orbits are chosen to have maximum galactocentric distances at less than 30 kpc (see text for details). The orbital initial conditions of the 100 streams are the same in top and bottom panels, but the streams travel in different orbits due to the influence of the subhalos. The case where $M_{sub} > 5 \times 10^6 M_\odot$, not shown here, produces similar maps to the bottom panels.	80
4.5	Similar to Figure 4.4, but the underlying halo is the VL-2 halo at redshift zero. Compared to the spherical halo in Figure 4.4, the streams in the VL-2 halo appear much more dispersed, especially in smooth halo (top panels). Note that the orbits of the streams in this figure are selected by the same criteria and result in the same eccentricity distribution as the orbits in Figure 4.4.	81
4.6	Cumulative fractions of the streams as functions of cell occupancy in the VL-2 and the spherical NFW halos. Each line represents the median of 50 streams in each of the “inner” and “outer” sets. The inner set contains streams whose orbits have $r < 30 \text{ kpc}$ and $r_{min} < 10 \text{ kpc}$, whereas the outer set contain streams whose orbits are bounded by $10 \text{ kpc} < r < 30 \text{ kpc}$. The thin dashed line and thick dashed-dotted lines represent lumpy halos with subhalo mass ranges indicated in solar masses. The stream particles are assigned to the nearest grid cell at 0.1 kpc on each side. The dense tail at 3 Gyr for the outer stream is the remains of the progenitors that have not been completely dissolved yet (Figure 4.3).	83

4.7	Six of the densest streams at 9 Gyr in the VL-2 halo. Each stream is projected onto the sky using Hammer-Aitoff equal-area projection as seen from the galactic center. Both latitudinal and longitudinal grid lines in all panels are spaced at 5° apart. Eccentricities e for the streams in the lumpy halo (C, D, E, F) are quoted for the streams' orbits without subhalos. Note that the color scale is the log of the number of particles in each bin at 0.1° on each side. In the smooth halo, streams A and B remain narrow and are compressed during pericentric passages, which enhance their densities. In the lumpy halo, the densest points of a stream can either be a narrow segment (C and E) or clumping due to subhalo perturbations (D and F).	85
4.8	Spherical volumes of $d = 3$ kpc in radius packed in a way such that each volume is centered at 8 kpc away from the galactic center. The radius of the volumes is chosen to represent the largest distance which reliable three dimensional velocities can be observed, and the number of spheres are chosen such that the volumes can be packed together as densely as possible without significant overlapping.	87
4.9	Sky projection of stream segments as seen from the center of one of the $d = 3$ kpc volumes in Figure 4.8 at 6 Gyr inside the VL-2 lumpy halo with $M_{sub} > 10^7 M_\odot$. Each color identifies the particle members of each stream. A total of 9 streams (with at least 20 particles) are found inside this volume.	88
4.10	Cumulative fractions of spherical volumes as functions of the number of stream segments (with at least 20 particles) inside each volume. Note that in this study we only simulated 100 streams. The number of streams in observations will depend on the actual number of streams and their kinematical distributions in reality. Top and bottom panels use 25 volumes at $d = 3$ kpc each and 15 volumes at $d = 4$ kpc each, respectively. Solid and dashed lines represent the smooth and lumpy halos with $M_{sub} > 10^7 M_\odot$, respectively. The $M_{sub} > 5 \times 10^6 M_\odot$ case produces similar results to the $M_{sub} > 10^7 M_\odot$ case shown.	89
4.11	Projections of the 3D velocities of the 9 streams shown in Figure 4.9 with the same colors for each stream. The scatter of ~ 200 km s $^{-1}$ in the mean velocities of each stream is due to the variety in orbits. Clearly even very dispersed streams (eg. the dark blue stream in Figure 4.9) appear localized in velocity space of the local volume.	91
4.12	Distributions of the velocity dispersions in all stream segments inside all 25 $d = 3$ kpc volumes inside the lumpy VL-2 halo with $M_{sub} > 5 \times 10^6 M_\odot$. Top, middle, and bottom panels show the smallest, second largest, and the largest principal components (ie. square roots of the eigenvalues of the covariance matrix) of the 3D velocity distribution, respectively.	92

Chapter 1

Introduction

1.1 The Dark Matter Problem

In the 20th century, careful observations of stars and galaxies revealed a tantalizing surprise—there was not enough mass to gravitationally hold stars onto galaxies, and galaxies onto clusters. This led to a radical speculation that if Newtonian gravity holds on galactic scales, there must exist an exotic form of matter that neither emits nor absorbs electromagnetic radiation of any wavelength, making it impossible to be observed directly with conventional telescopes. This exotic form of matter, now known as dark matter, provides the “extra gravity” which was not accounted for when observing the luminous matter such as stars and galaxies alone. Understanding dark matter has since become one of the biggest challenges in fundamental physics.

Although dark matter has remained enigmatic for decades since its discovery, some theoretical progress has been made. In particular, the model of *cold dark matter* has been widely successful at predicting the large scale distribution of galaxies (Blumenthal et al., 1984; Davis et al., 1985; Bardeen et al., 1986). Together with the observational evidence of the cosmological constant Λ responsible for accelerating the expansion of the universe (Riess et al., 1998; Perlmutter et al., 1999), the Λ -cold-dark-matter (Λ CDM) model of the Universe has widely become a “standard model” of the Universe.

1.2 The Triumphs of the Λ CDM Model on Large Scales

The Λ CDM model is successful in that it makes many predictions that have been confirmed by observations, especially in the era of “precision cosmology” where cosmological parameters can be measured at the percent level. The model contains a number of parameters; for example Ω_m and Ω_Λ represent the amounts of matter and dark energy in the universe, respectively. Below is two independent methods, among many others, that illustrate the power of the model.

Cosmic Microwave Background (CMB)

Observations of the sky in microwave frequencies revealed an apparently isotropic background of radiation that corresponds to a black body temperature of a few Kelvins above absolute zero (Penzias & Wilson, 1965). This background radiation, now known as the CMB, was predicted to be a relic of the hot and

dense beginning of the big bang. As the universe expands and cools, electrons recombine with protons and decouple from photons, and this transitions the universe from being opaque to transparent.

At the turn of the century, various experiments such as COBE¹, WMAP², and Planck³ measured the CMB in much greater precisions, and found that the background radiation contains fluctuations on the order of 10^{-5} . Moreover, the distribution of the fluctuations in angular scales, or the angular power spectrum, has also been measured (see Hu & Dodelson 2002 for a review). The Λ CDM model predicts that prior to recombination, the photon-baryon fluid underwent acoustic oscillations inside dark matter potential wells, and that the angular power spectrum would exhibit “wiggly” features that represent the various phases of the acoustic oscillations during recombination (Hu & Sugiyama, 1995, 1996). The observed angular power spectrum agrees with this prediction made by the Λ CDM model to exquisite precision (e.g. Hinshaw et al., 2003; Spergel et al., 2003; Planck Collaboration et al., 2014).

Large Scale Structures of Matter

Results from galaxy surveys such as 2dF⁴ and SDSS⁵ showed that galaxies are not distributed randomly in the universe, but they tend to organize themselves into clusters which are in turn organized into filamentary structures (Springel et al., 2006, and references therein). Similar to the angular power spectrum of the CMB, a power spectrum can also be obtained by the fluctuations of the galaxy number densities in spatial scales. Assuming that galaxies are reasonable tracers of the underlying distribution of dark matter, then the galaxy power spectrum can also be thought of as the dark matter power spectrum.

The Λ CDM model predicts that large scale structures form hierarchically from the smallest scales which subsequently merge into larger scales by gravitational interaction. The observed matter power spectrum agrees with the prediction by the Λ CDM model, both analytically on large scales and numerically on galactic scales (Cole et al., 2005; Tegmark et al., 2004; Springel et al., 2005). In particular, the same wiggles found in the CMB angular power spectrum can also be found in the matter power spectrum (Cole et al., 2005; Eisenstein et al., 2005).

1.3 The Problems of the Λ CDM Model on Small Scales

Despite the Λ CDM model’s success on large scales, some of the model’s theoretical predictions on sub-galactic scales—especially as computational power, and the resolution in simulations, increase—have yet to be confirmed by observations. Competing solutions to the following problems can be roughly classified into two types—astrophysical and physical. Astrophysical solutions, on one hand, are based on the complication of baryonic processes which have yet to be understood in detail. Since baryons are only about 20% as abundant as dark matter in the universe, it was common for past simulations to neglect baryons whose radiation and gas physics are much more complicated than the purely gravitational physics of cold dark matter. However, recent simulations that include baryons show that radiation and gas physics can indeed have a significant effect on dark matter via the gravitational coupling between baryons and dark matter. Physical solutions, on the other hand, postulate that our understanding of cold dark matter may be incomplete. Simulations show that alternative dark matter solutions, such as

¹<http://lambda.gsfc.nasa.gov/product/cobe/>

²<http://map.gsfc.nasa.gov/>

³<http://sci.esa.int/planck/>

⁴<http://www.2dfgrs.net/>

⁵<http://www.sdss.org/>

warm dark matter (Barkana et al., 2001; Bode et al., 2001; Benson et al., 2013; Schneider et al., 2013) and self-interacting dark matter (Spergel & Steinhardt, 2000) produce structures that are inherently different than cold dark matter.

The cusp-core problem is the disagreement between dwarf galaxies’ theoretical and observationally inferred density profiles. Theoretical simulations predict that dwarf galaxies’ density profiles should asymptotically increase towards the galaxies’ central regions (Navarro et al., 1997), whereas observations imply that the density profiles flatten into “cores” (de Blok et al., 2003; Swaters et al., 2003). Astrophysical effects such as supernova feedback (Pontzen & Governato, 2012) and infalling baryons (Cole et al., 2011) have been invoked to show that baryons can rearrange the dark matter distribution in the centers of dwarf galaxies in order to transform cusps to cores. On the other hand, the collisional nature of self-interacting dark matter has been shown to produce cores instead of cusps (Vogelsberger et al., 2012, 2014).

The “too big to fail” problem is the disagreement between the theoretical and observed numbers of bright satellite galaxies around the Milky Way (Boylan-Kolchin et al., 2011). Theoretical simulations predict that a Milky-Way-sized galaxy should be surrounded by more dark matter subhalos that are denser and more massive than those subhalos which host the Milky Way’s brightest dwarf spheroidal galaxies. It has been argued that the solution to the problem is closely related to the cusp-core problem (Madau et al., 2014; Ogiya & Burkert, 2015). The central densities of the subhalos were originally inferred by circular velocities in cuspy dark matter-only profiles. In simulations that produce cores in subhalos, circular velocities are lower and thus compatible with the observed values.

The missing satellites problem is the disagreement between the theoretical and observed numbers of low mass satellite systems in the Milky Way (Klypin et al., 1999; Moore et al., 1999). Theoretical simulations predict the existence of many low mass dark matter subhalos, which are remnants of the incomplete mergers of smaller systems as they hierarchically merge into a Milky-Way-sized dark matter halo. However, the observational counterparts of these satellites systems have yet to be found. This thesis focuses on the development of an observational probe to measure the abundance of subhalos which are still “missing.”

A variety of astrophysical solutions have been proposed to solve the missing satellite problem. For example, reionization radiation or stellar feedback can essentially heat up the gas inside subhalos to hinder star formation (Bullock et al., 2000; Benson et al., 2002; Kopolov et al., 2009; Macciò et al., 2010), making them difficult to be observed directly. Warm dark matter and self-interacting dark matter as mentioned above, and even inflationary models with non-scale invariance (Kamionkowski & Liddle, 2000) all offer mechanisms that suppress structure formation on small scales. The difference between the astrophysical and physical solutions is the abundance of subhalos. Even though star formation quenching may explain why galaxies do not form in subhalos, the existence of subhalos itself—a fundamental prediction of the Λ CDM model—remains to be tested.

1.4 Tidal Streams

The original methods to discover dark matter were based on dark matter’s dynamical influences on luminous sources such as stars and galaxies. To measure the abundance of dark matter subhalos, we follow the same approach and look for the subhalos’ dynamical influence on very specific luminous sources—tidal streams (or simply “streams” throughout much of this thesis). Tidal streams are remnants of stellar systems such as globular clusters or dwarf galaxies that were tidally disrupted by a massive host. When the stars become unbound from the progenitor, they trace an elongated tail which wraps around the massive host.

Tidal remnants have long been useful probes for studying the gravitational potential of the Milky Way (e.g., Johnston, 1998; Helmi et al., 2003; Law et al., 2005; Belokurov et al., 2006; Bonaca et al., 2014). In particular, Ibata et al. (2002) and Johnston et al. (2002) first used simulations to show that the encounters between the stream stars and subhalos can dynamically heat up the stream, which can be used to probe the presence of subhalos. Moreover, a key influence that subhalos have on streams is that the stream stars near the point of the encounter get scattered into different orbits by the perturbation, causing an abrupt decrease in stellar density, or a “gap”, in that region of an otherwise smooth stream. Using the abundance of subhalos obtained from high-resolution simulations (Madau et al., 2008; Springel et al., 2008), it has been predicted that streams in the Milky Way described by the Λ CDM model should contain many gaps (Yoon et al., 2011; Carlberg, 2012; Carlberg et al., 2012; Carlberg & Grillmair, 2013).

Recent surveys have discovered the tidal debris of many disrupted stellar systems (Grillmair, 2010, 2014; Koposov et al., 2014; Martin et al., 2014; Bernard et al., 2014). In particular, the streams that are dynamically cold and thin—likely the debris of globular clusters—are especially useful since they are much simpler to model compared to streams that originate from dwarf galaxies (Lux et al., 2013). Two streams of particular interest to us are Pal-5 (Odenkirchen et al., 2001) and GD-1 (Grillmair & Dionatos, 2006). Both streams are detected as long, narrow tidal tails with length-to-width ratio of ~ 100 . These two streams are interesting as they show varying densities along the streams. It is not clear whether those density variations correspond to subhalo perturbations, as some studies have found that intrinsic mechanisms such as epicyclic overdensities (Küpper et al., 2008, 2010, 2012) and Jeans instabilities (Comparetta & Quillen, 2011) can also produce gap-like features which can be confused with gaps induced by subhalo perturbations. Therefore, extensive studies using simulations are required to understand gap formation in streams, and to test whether the gaps observed in streams are consistent with the prediction by the Λ CDM model.

1.5 Thesis outline

This thesis is organized into three main chapters. Each chapter consists of the content in an article which has either been accepted or is being prepared for submission to a peer-reviewed journal⁶.

Chapter 2 (Ngan & Carlberg, 2014) applies the basic methods used throughout this thesis work, which is to simulate tidal streams with and without subhalos to isolate the effects of subhalos on streams. We use N-body simulations to model the tidal disruption of a star cluster in a Milky-Way-sized dark matter halo, which results in a narrow stream comparable to (but slightly wider than) Pal-5 or GD-1. The mean Galactic dark matter halo is modeled by a spherical Navarro-Frenk-White (NFW) potential

⁶At the time of submission of this thesis, Chapters 2 and 3 have been accepted as two individual articles, and Chapter 4 is being prepared for submission.

with subhalos predicted by the Λ CDM cosmological model. The distribution and mass function of the subhalos follow the idealized results from the Aquarius simulation. We use a matched filter approach to look for “gaps” in tidal streams at 12 length scales from 0.1 kpc to 5 kpc. Finally, we project the simulated streams onto the sky to investigate issues when interpreting gaps in observations.

Chapter 3 (Ngan *et al.*, 2015) extends the earlier work of Chapter 2 and uses the results from a high-resolution dark matter halo simulation, rather than an idealized profile, as the underlying potential for the streams. We simulate tidal streams in the presence and absence of substructures inside the zero-redshift snapshot of the Via Lactea II (VL-2) simulation. A halo finder is used to remove and isolate the subhalos found inside the high-resolution dark matter halo of VL-2, and the potentials for both the main halo and all the subhalos are constructed individually using the self-consistent field (SCF) method. This allows us to make direct comparison of tidal streams between a smooth halo and a lumpy halo without assuming idealized profiles or triaxial fits. We simulate the kinematics of a star cluster starting with the same orbital position but two different velocities.

Chapter 4 uses the same dark matter halo potential developed in Chapter 3 to simulate a larger collection of streams to illustrate the difference between a realistic and an idealized potential. We simulate the tidal disruption of a collisionless N-body globular star cluster in 100 different orbits constrained to have galactocentric radii less than 30 kpc in four dark matter halos: (a) spherical halo with no subhalos, (b) spherical halo with subhalos, (c) realistic halo with no subhalos, and (d) realistic halo with subhalos. This allows us to isolate and study how the halo’s shape and substructures affect the dispersion of tidal debris in general, rather than focusing on one or two streams.

Chapter 2

Using Gaps in N-body Tidal Streams to Probe Missing Satellites

Abstract

We simulate the formation of a thin stream similar to Pal-5 or GD-1 using a self-gravitating star cluster inside a Milky-Way-sized dark matter halo. The halo is modelled both as a “smooth” halo which is simply a spherical Navarro-Frenk-White (NFW) potential, and a “lumpy” halo which is the same as the former but with the addition of subhalos consistent with the results from the Aquarius simulation. We use a matched filter approach to look for underdensities along the streams in those two cases. We find that, in addition to the subhalos’ perturbations, epicyclic overdensities (EOs) due to the coherent epicyclic motions of particles in a stream also produce gap-like signals near the progenitor. We measure the gap spectra—the gap formation rates as functions of gap length—due to both subhalo perturbations and EOs, which have not been accounted for together by previous studies. When the simulated streams are projected onto the sky, we find that gap spectra from low signal-to-noise observations can be biased by the orbital phase of the stream. This indicates that the study of stream gaps will benefit greatly from high-quality data from future missions.

2.1 Motivation

In this chapter, we measure the gap formation rate and study the length distribution of gaps by modeling a self-gravitating N-body stream in two cases: (1) in a smooth halo and (2) in a lumpy halo that has subhalos. The resulting streams can then be compared directly to isolate the effects caused by subhalos. In addition to subhalos, gaps can also form in streams due to other intrinsic effects such as epicyclic overdensities (EOs; Küpper et al., 2008, 2010, 2012) and Jeans instabilities (Comparetta & Quillen, 2011). As we show in this chapter, the length distribution of gaps caused by subhalos can be distinguished from those formed by EOs.

This chapter is organized as follows. Section 2.2 describes the details of our simulations, including the subhalo abundances and density profiles that we adapt, and the details of the star cluster and the resulting model stream. Section 2.3 focuses on the method of detecting gaps in a simulated stream. The method of using match filters is inspired by analyses for observations, but modified here to analyze simulations. Section 2.4 contains detailed discussion of our key results, including the phenomenology of gaps and comparisons with previous analytical predictions and observations. Section 2.5 is a summary of our results.

2.2 Simulations

2.2.1 Models

The host galaxy is modeled as a dark matter halo, as well as a set of subhalos which orbit around the halo’s potential. A Milky-Way-sized halo is modeled with a static spherical Navarro-Frenk-White (NFW) profile (Navarro et al., 1997) with $v_{max} = 210 \text{ km s}^{-1}$ located at $r_{max} = 30 \text{ kpc}$. Each individual subhalo is modeled by a spherical Hernquist profile (Hernquist, 1990)

$$\Phi_i(r) = \frac{GM_i}{h_i + r} \quad (2.1)$$

for simplicity, compared to Einasto profiles which produce better fits in simulations but are more complicated to compute (Springel et al., 2008). We use the formula found in Carlberg (2009), which approximates the results from both Springel et al. (2008) and Neto et al. (2007), where h_i is independent of galactocentric position, and is related to M_i by

$$h(M) = 6 \text{ kpc} \times \left(\frac{M}{10^{10} M_\odot} \right)^{0.43}. \quad (2.2)$$

We use the mass and spatial distributions of the subhalos from the results of the Aquarius simulations (Springel et al., 2008), where the mass function is independent of the spatial distribution. The mass function is a power law

$$\frac{dN}{dM} = 3.26 \times 10^{-5} M_\odot^{-1} \left(\frac{M}{2.52 \times 10^7 M_\odot} \right)^{-1.9}, \quad (2.3)$$

and the spatial distribution follows an Einasto profile

$$n(r) \propto \exp \left\{ -2.95 \left[\left(\frac{r}{199 \text{ kpc}} \right)^{0.678} - 1 \right] \right\}. \quad (2.4)$$

The mass ranges of the subhalos that are used in our simulations are summarized in Table 2.1 and discussed in Section 2.4.5. The subhalos' velocities are initialized with a Gaussian distribution where the velocity dispersion is the solution to the isotropic Jean's equation (Binney & Tremaine, 2008) using the halo's potential. The subhalos orbit around this potential as test masses.

The progenitor of the stream, which is an approximation to a globular star cluster, is initialized using 10^6 particles of equal mass as a King model with $w = 4.91$, where w is the ratio between the depth of the potential and central velocity dispersion of the cluster. The cluster has a total mass of $4.29 \times 10^4 M_\odot$, and a core radius of 0.01 kpc. This results in a zero-density radius of 0.103 kpc. Each N-body particle in the system interacts with the dark matter halo's and subhalos' potentials. With the Galactic center at the origin, the satellite is initially put at $(x, y, z) = (30, 0, 0)$ kpc and velocity $(v_x, v_y, v_z) = (0, 140, 0)$ km s^{-1} . The resulting orbit, as shown in Figure 2.1, is confined to the xy -plane with eccentricity 0.33, peri- and apogalacticon at $r_p = 15$ kpc and $r_a = 30$ kpc, respectively. The azimuthal and radial periods are about 0.70 Gyr and 0.47 Gyr, respectively.

2.2.2 Software and Parameters

We use GADGET-2 (Springel, 2005) for our N-body simulations. Since the public distribution¹ does not have functionality for external potentials, we modify the code such that in every time step, an external acceleration term which accounts for the potentials of the halo and all the subhalos is added to the accelerations of all the particles after their N-body interactions are computed.

Each of our simulations lasts 10 Gyr, and we impose a maximum time step of 1 Myr. The particle softening is 5 pc. Each simulation produces 500 snapshots, one every 20 Myr, and each consists of the positions and velocities of the N-body particles and subhalos.

2.2.3 Stream Properties

The star cluster is modeled as an N-body system which forms a stream as the cluster is disrupted by the tidal field of the massive host. When the cluster is isolated, the energies of the individual particles are conserved to a few percent over 10 Gyr. Using the softening as minimal impact distance, the relaxation timescale in the core is $\gtrsim 110$ Gyr, which is much greater than the orbital period at $\lesssim 1$ Gyr. Figure 2.2 shows the mass enclosed inside 0.103 kpc of the star cluster's center while orbiting in the absence of subhalos. Because the stream is repeatedly stretched and compressed longitudinally along the eccentric orbit, the mass enclosed by a fixed radius is not always decreasing in time. The middle panel of Figure 2.2 shows that the mass loss in the progenitor follows immediately after each pericentric passage as the periodic bursts have exactly the same period as the radial period of the orbit.

Figure 2.3 shows the velocity dispersion and transverse FWHM of our simulated stream without any subhalos. The stream is chosen so that its properties are of the same orders of magnitude as Pal-5 (Dehnen et al., 2004; Odenkirchen et al., 2009) and GD-1 (Koposov et al., 2010; Willett et al., 2009). In the derivation in Carlberg (2012), the gap formation rate is expressed as a function of galactocentric distance of the orbit and width of the stream. For our simulated stream, we adopt average values of 22 kpc and 0.3 kpc, respectively, over the entire stream.

In a time independent and spherical potential $\Phi(r)$, three interesting conserved quantities are the

¹<http://www.mpa-garching.mpg.de/gadget/>

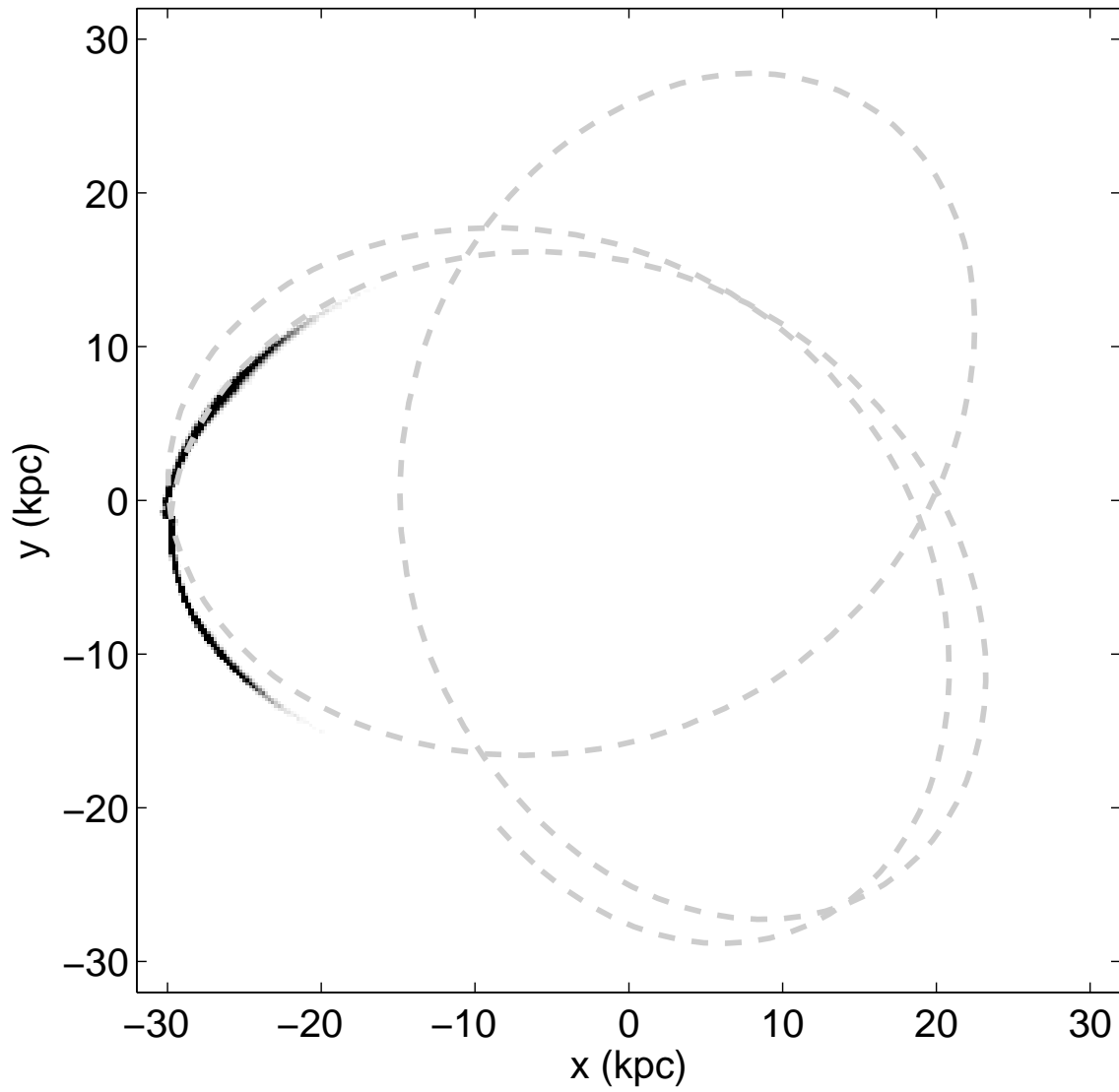


Figure 2.1: The progenitor's orbit (dotted line) used in this chapter. The orbital plane is confined to the xy -plane. The black pixels centered at $(x, y) \approx (-30, 0)$ kpc represent an 8 Gyr old stream.

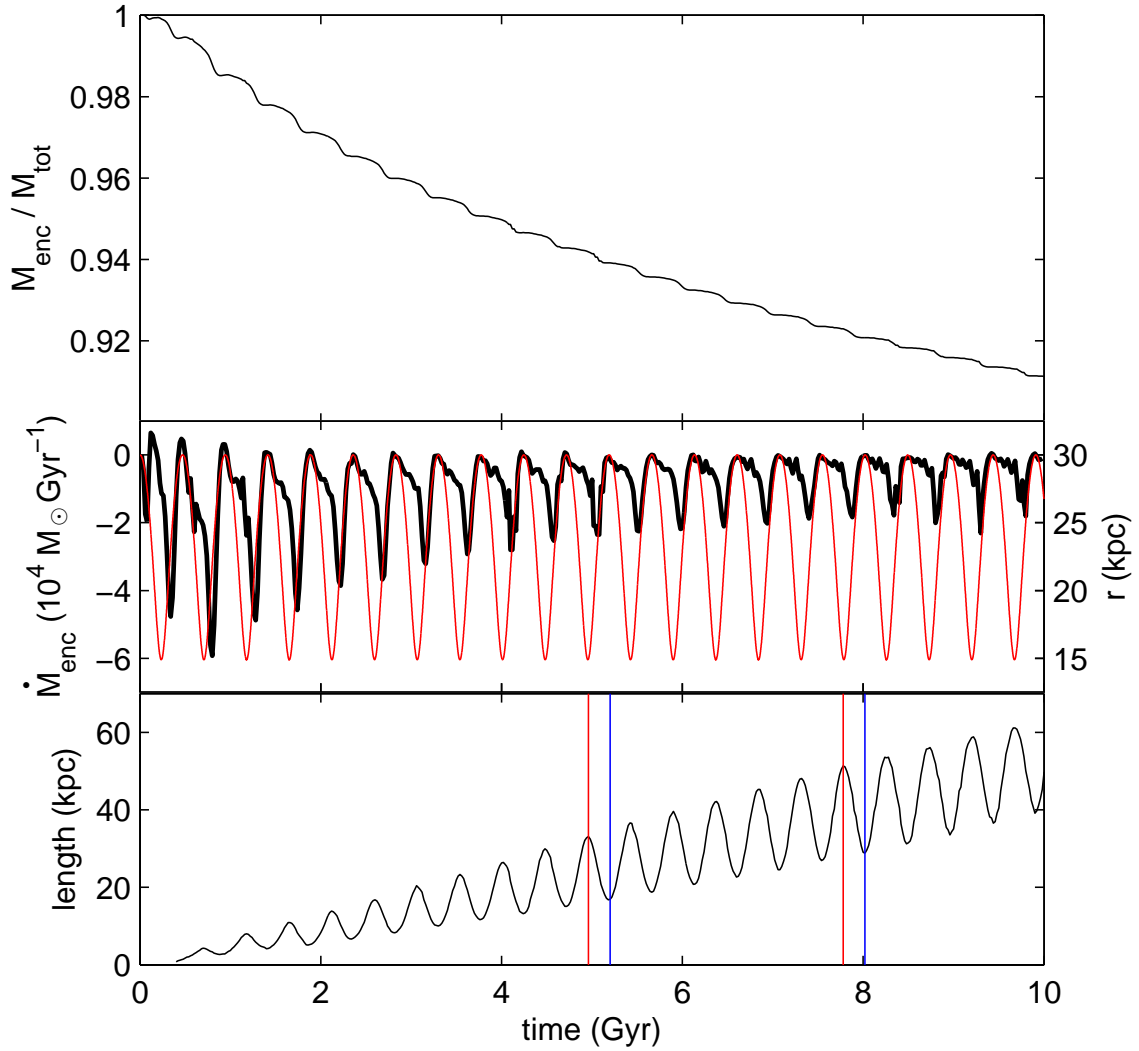


Figure 2.2: Top: fraction of mass enclosed in 0.103 kpc of the star cluster while orbiting the dark matter halo without any subhalos. Middle: rate of change of mass enclosed in 0.103 kpc of the star cluster (solid black) and radial position of the star cluster’s orbit (red). This shows that the star cluster experiences bursts of mass loss almost immediately after each pericentric passage. Bottom: length of the stream. This shows that the stream gets stretched and compressed depending on its orbital phase. The red and blue vertical lines correspond to the snapshots where the star cluster is at the pericenters and apocenters of its orbit, respectively. These times are selected to demonstrate the bias discussed in Section 2.4.4.

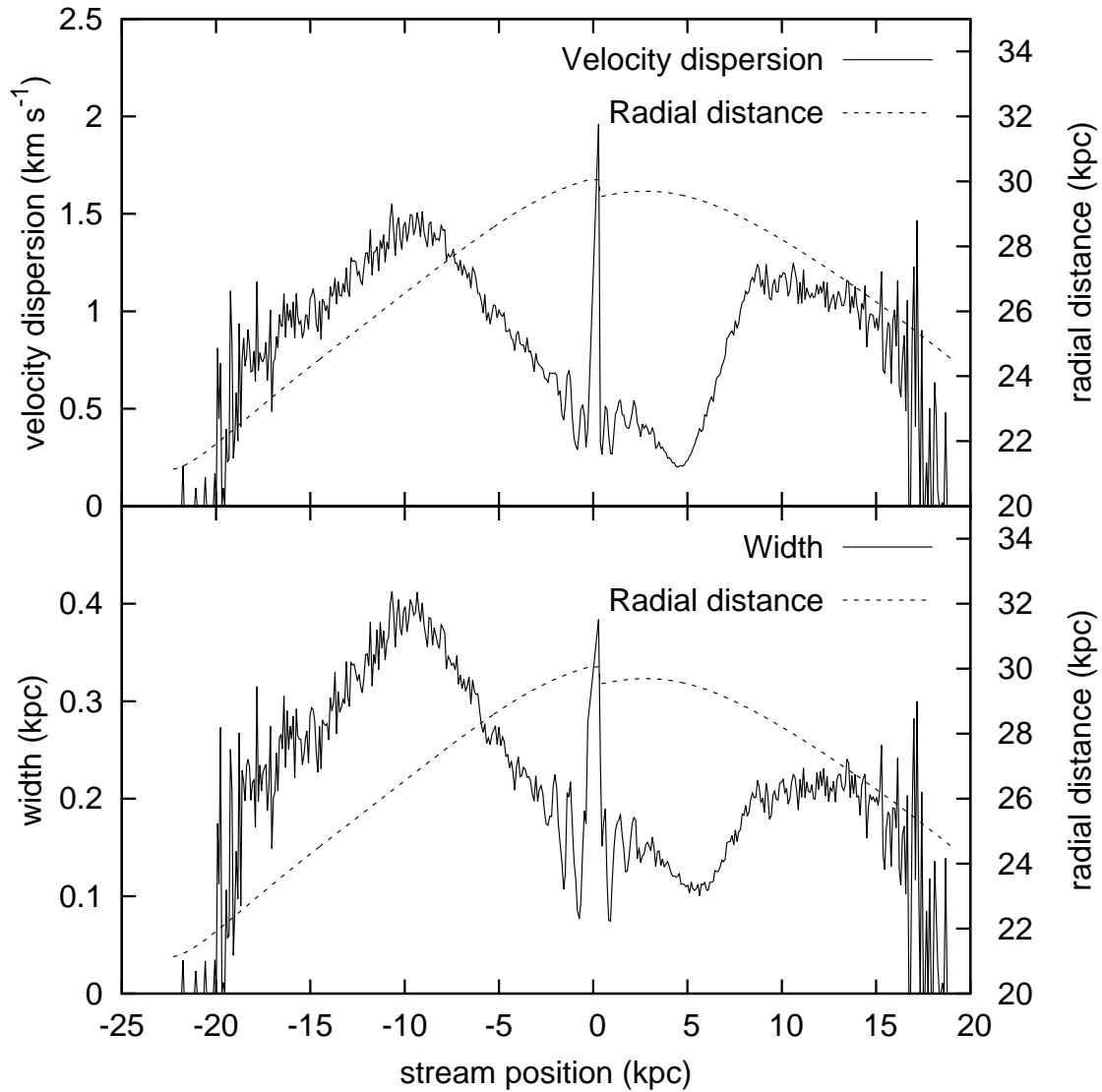


Figure 2.3: Tangential velocity dispersion and FWHM width along the stream at 8 Gyr. The progenitor is centered at 0 kpc, where positive and negative positions represent the leading and trailing branches of the stream, respectively. The structures in velocity dispersion and width are due to the eccentricity of the stream, as traced by the orbital distance along the stream.

radial, azimuthal, and latitudinal actions where

$$J_r = \frac{1}{\pi} \int_{r_p}^{r_a} dr \sqrt{2E - 2\Phi(r) - \frac{L^2}{r}} \quad (2.5)$$

$$J_\phi = L_z \quad (2.6)$$

$$J_\theta = L - |L_z| \quad (2.7)$$

respectively (Binney & Tremaine, 2008), where r_a and r_p are the apo- and pericentric distances of the orbit, respectively. Since our stream's orbital plane is the xy -plane, $J_\theta \approx 0$ (though not exactly 0 because the stream has a finite thickness), so we only consider J_r and L_z . For simplicity, we ignore the progenitor and only consider the particles which have already escaped from the cluster, so when computing J_r we assume that the potential due to the progenitor's potential is negligible.

J_r and L_z are useful since their dispersions are the origins of the stream's average width. For example, in the epicyclic approximation (Binney & Tremaine, 2008) where κ and a are the epicyclic frequency and amplitude, respectively, the radial motion can be written as

$$r(t) = a \cos(\kappa t + \psi) \quad (2.8)$$

where ψ is an arbitrary phase angle. Then it can be shown that

$$J_r = \frac{1}{2\pi} \oint p_r dr \propto \int \dot{r} dr \propto \kappa a^2 \quad (2.9)$$

$$L_z = R_g^2 \Omega \quad (2.10)$$

where Ω and R_g are the orbital frequency and radius of the guiding center, respectively. Clearly, dispersions in both a and R_g can affect the width of the stream. Therefore, conserved quantities J_r and L_z are especially valuable in understanding the width of the stream. Figure 2.4 shows the distributions in (J_r, L_z) when the stream is 8 Gyr old. The two lobes at higher and lower L_z are the trailing and leading branches of the stream, respectively. The absolute dispersions in J_r and L_z are on the same order of magnitude, in rough agreement with the formula $\Delta J_r / \Delta L \sim (r_a - r_p) / \pi r_p$ (Eyre & Binney, 2011). In Section 2.4.1, we will show how the spread in actions affects the morphology of stream gaps.

Plots similar to Figure 2.4 can be found in Eyre & Binney (2011) where they used angle-action variables extensively to study the relation between the stream and the orbit. A similar plot can also be found in Yoon et al. (2011), but in scaled energy and angular momentum which were first used by Johnston (1998) to describe the dynamics of tidal streams.

2.3 Method

2.3.1 Subhalo Mass Ranges

Yoon et al. (2011) divided their subhalo mass spectrum into separate mass ranges in order to resolve the contributions from each mass range. Using the same approach, we divide the subhalos from 6.5×10^4 to $10^8 M_\odot$ into 13 mass ranges (Table 2.1). Each mass range contains incrementally more subhalos, starting from the higher mass end toward the lower mass end. In the higher mass end, the mass ranges are chosen such that the increase in subhalo masses are roughly the same. In the lower mass end, the

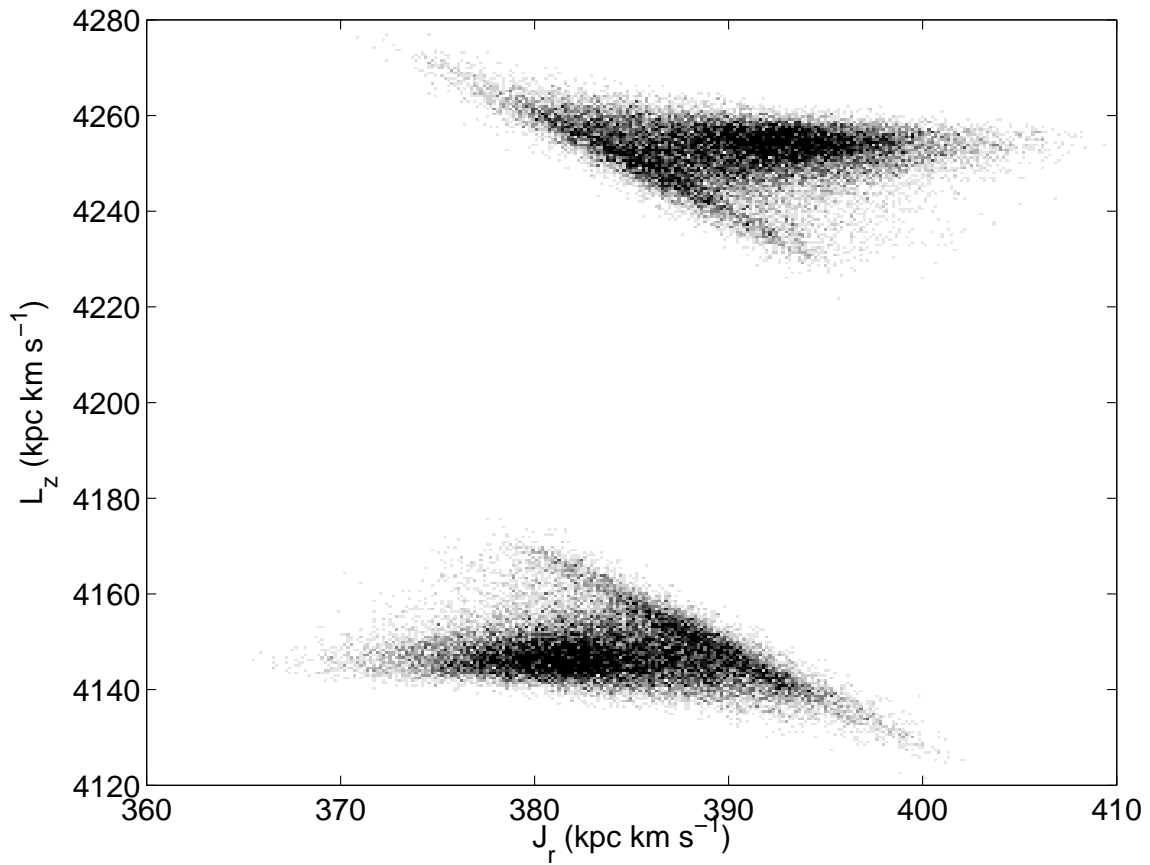


Figure 2.4: Distribution of orbital action variables (J_r, L_z) for our stream at 8 Gyr without any subhalos. Along the entire stream with the progenitor masked out, 50,000 unbound particles were randomly selected to be placed on this map. Each pixel in this map represents the density of particles in that bin. The two symmetric lobes are the two branches of the stream. Similar plots can be found in Eyre & Binney (2011), and a plot in scaled energy and angular momentum in Yoon et al. (2011).

m_{low}/M_{\odot}	N	M/M_{\odot}	N_{orbit}	M_{orbit}/M_{\odot}
5.3×10^7	203	1.5×10^{10}	30	2.2×10^9
2.7×10^7	593	2.9×10^{10}	98	4.7×10^9
1.3×10^7	1,392	4.4×10^{10}	220	6.9×10^9
5.8×10^6	3,160	5.9×10^{10}	476	9.1×10^9
2.5×10^6	7,038	7.3×10^{10}	1,101	1.1×10^{10}
1.0×10^6	16,394	8.8×10^{10}	2,576	1.4×10^{10}
3.6×10^5	41,515	1.0×10^{11}	6,539	1.6×10^{10}
2.1×10^5	67,599	1.1×10^{11}	10,563	1.7×10^{10}
1.5×10^5	91,601	1.1×10^{11}	14,337	1.8×10^{10}
1.1×10^5	121,181	1.2×10^{11}	18,872	1.8×10^{10}
9.0×10^4	145,220	1.2×10^{11}	22,578	1.9×10^{10}
7.5×10^4	171,163	1.2×10^{11}	26,586	1.9×10^{10}
6.5×10^4	194,726	1.2×10^{11}	30,253	1.9×10^{10}

Table 2.1: Thirteen Subhalo Mass Ranges in Our Simulations. The upper limit cuts off at $10^8 M_{\odot}$ for all ranges. Columns from left to right: lower mass limit, total number and total mass in subhalos (Equation 2.3), number and mass in subhalos used in simulation after reduction by orbit (see the text).

mass ranges are chosen such that the increase in subhalo numbers are roughly the same.

In each set of subhalos, we reduce their numbers by eliminating those whose orbits are always inside the perigalacticon and outside the apogalacticon of the progenitor’s orbit. The largest subhalo in our simulations has a length scale of ~ 1 kpc (Equation 2.2), so all the subhalos with perigalacticon (apogalacticon) larger (smaller) than that of the progenitor’s orbit by ~ 2 kpc will interact minimally with the stream. This allows us to safely eliminate the subhalos with perigalacticon larger than 32 kpc, and apogalacticon smaller than 13 kpc.

We run 14 simulations—1 “smooth stream” without any subhalos, and 13 “ Λ CDM streams” containing the subhalos in the mass ranges in Table 2.1—with identical initial conditions and dark matter halo potential. This allows us to resolve the effects of the lower mass subhalos whose existence are in question.

2.3.2 Gap Finding

Gaps are manifested as local minima in the linear density along the stream. To obtain the linear density along a stream in an eccentric orbit, we first fit the stream with two degree-6 polynomials—one each for the leading and trailing streams—in polar coordinates centered at the Galactic center. The points along each line are spaced at 0.002 radians apart. Between each pair of adjacent points a cylinder of radius 1 kpc is drawn which lies lengthwise along the pair of points. The linear density is then the number of particles inside this cylinder divided by the length of the cylinder. This spacing is chosen so that gaps as wide as the stream are well resolved.

The method used to find gaps in stream densities is inspired by the technique first used by Carlberg et al. (2012) to find gaps in observations. They used matched filters of the estimated shape of a density gap at various length scales to look for positions in the stream which potentially contain gap signals. The filter consists of a local minimum which is the underdensity of stars, and two local maxima on both sides of the minimum due to conservation of mass (Figure 2.5). This method is similar to the wavelets

approach, where the integral of the filter function is constructed to vanish inside a certain domain. The potential gap signals are then easily identified as local maxima in the convolution between the filter and the signal.

To obtain the significance of each potential gap signal against noise, Carlberg et al. (2012) produced bootstrap samples from the sky background. With the simulations in this chapter, we can estimate noise levels using the smooth stream. Note that the “smooth stream” itself is not totally smooth. As we will show in Section 2.4.2, there are large density fluctuations near the progenitor due to the coherent epicyclic motion of the particles, as first explained by Küpper et al. (2008). When the particles become unbound from the progenitor, they pile up near the base of their cycloid trajectories, creating epicyclic overdensities (hereafter EO) along the stream. Although this intrinsic process to mimic gaps can be confused with gaps caused by subhalos, EOs are only apparent within $\lesssim 5$ kpc away from the progenitor in our streams (Figures 2.8 and 2.9). The details of the dynamics of EOs is beyond the scope of this chapter, but this effect can be understood in terms of orbital actions. EOs occur due to coherent epicyclic motions of the particles, which nevertheless have finite dispersions in orbital actions (Figure 2.4) and are not perfectly coherent. Therefore, although the escaping particles’ orbits stay roughly coherent in the first few clumps, their orbits eventually drift out of phase as they travel along the stream. This explains why the density peaks of EOs further downstream are not as apparent as the peaks closer to the progenitor (Just et al., 2009; Küpper et al., 2010).

After masking 10 kpc of the smooth stream centered at the progenitor, the rest of the smooth stream is simply noise. Our method to find gaps in a given stream can be summarized as follows.

1. Compute

$$C_s(x) = \frac{1}{s} \int_{x-1.5s}^{x+1.5s} [\rho(x') - \bar{\rho}_s(x)] f\left(\frac{2(x-x')}{s}\right) dx' \quad (2.11)$$

where $f(t) = (t^6 - 1) \exp(-1.2321t^2)$ is a matched filter function (Carlberg et al., 2012; Carlberg & Grillmair, 2013), and s is the filter scale. $\bar{\rho}_s(x)$ is the mean of $\rho(x)$ inside $[x - 1.5s, x + 1.5s]$, the domain in which the integral of $f(2x/s)$ itself vanishes. Each potential gap signal would appear as a local maximum in $C_s(x)$. This convolution is computed at 12 logarithmically spaced filter scales from 0.1 to 5 kpc (Figure 2.5), and then all the local maxima of each stream are sorted by C_s .

2. Repeat the above step using the smooth stream, but with ± 5 kpc from the progenitor masked along the stream. The set of local maxima in $\tilde{C}_s(x)$ from this convolution is the noise, which are also sorted by \tilde{C}_s .
3. Each local maximum in the signal set are compared against the noise set. A signal element at any position along either branch of the stream that ranks higher than 99% in the noise set is identified as a gap.

Inevitably, this method may detect the same gap at 99% confidence at different scales but in very close proximity. To avoid over-counting, we employ the following scheme to eliminate overlapping gaps. First, we define an overlap as two gaps whose C_s local maxima are identified at $C_{s_1}(x_1)$ and $C_{s_2}(x_2)$ that are within s_1 away from each other along the stream, where $s_2 < s_1$. When this occurs, the gap with higher C_s eliminates the lower.

Our gap detection method requires no prior knowledge whether a given gap is an EO or a subhalo perturbation, both of which can be identified as a series of over- and under-densities. When we count

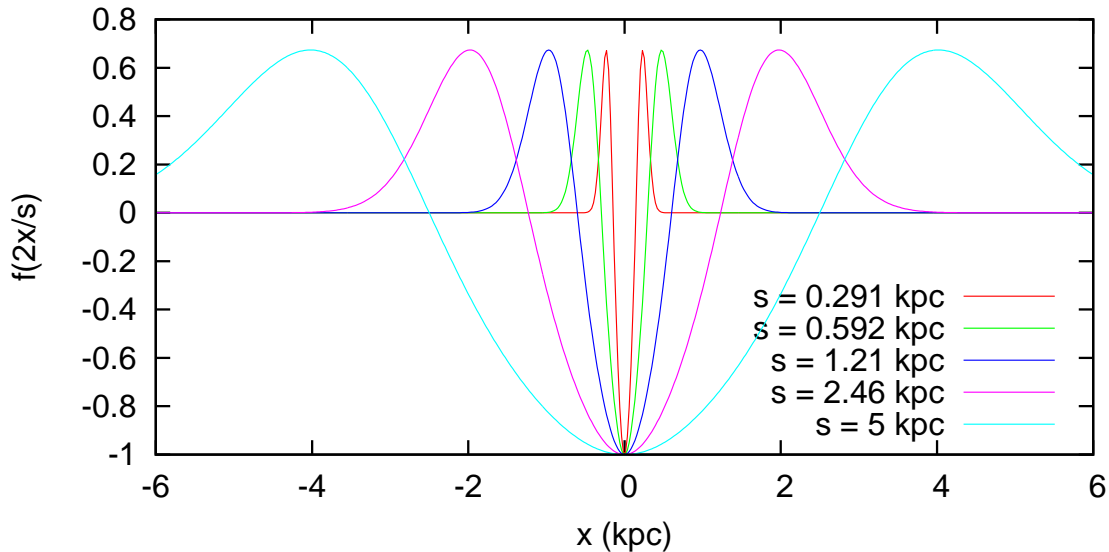


Figure 2.5: Five example filter scales for the match filter used in Carlberg et al. (2012), which has the functional form $f(t) = (t^6 - 1) \exp(-1.2321t^2)$. With a physical scale s , the integral of $f(2x/s)$ vanishes inside $-1.5s < x < 1.5s$. The roots of each filter are located at $\pm s/2$ so that the gap length is simply the distance between the roots. We search for gaps at 12 logarithmically filter scales from 0.1 to 5 kpc in order to minimize the chance of detecting the same gap at multiple scales.

the number of gaps in the end, EOs will be included. One key result of our study is that gaps due to EOs are distributed very differently in lengths compared to gaps due to subhalo perturbation.

2.4 Results and discussion

2.4.1 Gap Morphology

According to Yoon et al. (2011), gaps in general are diagonal and not perpendicular to the stream due to a gradient in angular momentum (hence a gradient in orbital velocities) across the width of the stream, which can shear a gap longitudinally. Figure 2.4 allows us to estimate the shearing effect in our streams using the distributions in angular momenta. For each branch of the stream, the FWHM spread in angular momentum is about $\Delta L \sim \Delta L_z \sim 10 \text{ kpc km s}^{-1}$. For a narrow stream at $r = 22 \text{ kpc}$, the spread in velocity is $\Delta v = \Delta L/r \sim 0.5 \text{ km s}^{-1}$. Therefore, a gap that spans the width of the stream will be sheared by less than 1 kpc per Gyr.

Figures 2.6 and 2.7 show the time evolution of the smooth stream and a Λ CDM stream, respectively, from 7 to 8 Gyr. The EOs near the progenitor appear to shear by different amounts at different times, but this is due to the radial oscillation in the orbit where the radial period is $\sim 0.5 \text{ Gyr}$. Upon closer inspection of Figure 2.7, we also note that not only do subhalo gaps have complicated morphologies, but their orientations flip back and forth in a radial period due to the spread in J_r . Nevertheless, comparing panels of the same radial phase at one radial period apart, the end points of each gap across the width of the stream do not shift by any appreciable amount. Rather, the morphologies of the subhalo gaps are

already apparent as each gap first appears.

If the linear density of a stream is calculated by integrating the entire thickness of the stream in traversing slices along the stream, then the contrast of the gap will be reduced. This is because the edges of the gaps are not perfectly straight across the width of the stream, so dividing the stream into slices will smear out the density contrast. To investigate how much the smearing will affect gap detection, we calculate the linear densities in two ways. (1) Integrating cylindrical slices of radius 1 kpc along the stream, hereafter the “whole width,” where 1 kpc was chosen to cover the entire thickness of the whole stream. (2) Integrating only the cylindrical slices of radius 0.04 kpc centered along the best fit line of each branch of the stream, hereafter the “central width,” where 0.04 kpc is chosen to mimic the GD-1’s observed width of 0.08 kpc (Carlberg & Grillmair, 2013). This central width then encloses about 30%–40% of the mass of the whole width, depending on its orbital phase where, for example, the stream is radially compressed during pericentric passage.

2.4.2 Gap Counting

Figures 2.8–2.11 show the densities along the whole and central widths of the smooth stream and a Λ CDM stream from 3 to 10 Gyr. The streams younger than 3 Gyr are not shown as the stream is $\lesssim 10$ kpc long at those ages, so the gaps are dominated by very prominent EOs. Moreover, the stream itself does not yet have a large enough cross section to produce enough gaps for meaningful statistics. In each panel, the shaded columns represent the gaps that are found on the scale of the columns’ widths. Although these gaps are identified as being 99% significant, the density contrasts of the gaps have not been quantified. For the rest of this chapter, we assume that all gaps identified at 99% significance can be observed. Note that because the gap finding process is applied independently to each snapshot, the shaded columns do not necessarily represent the time evolutions of individual gaps. Instead, the shaded columns show the general distributions of gaps – both in space and in gap lengths.

Our gap finding method has a number of problems. In the smooth stream (Figures 2.8 and 2.9), our method by construction identifies 1% of the noise as gaps. This is why there can be spurious gaps detected well beyond 5 kpc away from the progenitor, even though EOs tend to form very close to the progenitor. Also, the overall profile of the stream density can sometimes be confused as a gap as well. One example is a gap at 4 kpc at 5 Gyr in Figure 2.10, where a smooth density gradient from 3 to 8 kpc is mistaken as the right half of a long gap. At the 95% confidence limit, both kinds of false positives are quite common and can often be identified by eye. For the results below, we show gaps that are 99% significant, which minimizes the occurrence false positives.

2.4.3 Gap Spectrum

Carlberg (2012) modelled streams as circular rings of particles and used various approximations such as number density, mass function, velocity distribution of subhalos to predict the encounter rate between subhalos and a given stream. Following that approach, Carlberg & Grillmair (2013) derived an analytical relation between gap formation rate R_{\cup} which is the cumulative number of gaps longer than length l per unit stream length per unit time as a function of gap length (hereafter the “gap spectrum”) such that

$$R_{\cup}^{\text{ideal}} = 0.060 \hat{r}^{0.44} l^{-1.16} \text{ kpc}^{-1} \text{ Gyr}^{-1} \quad (2.12)$$

where $\hat{r} \equiv r/30$ kpc, and we adapt $r = 22$ kpc for the average galactocentric radius of the stream. In

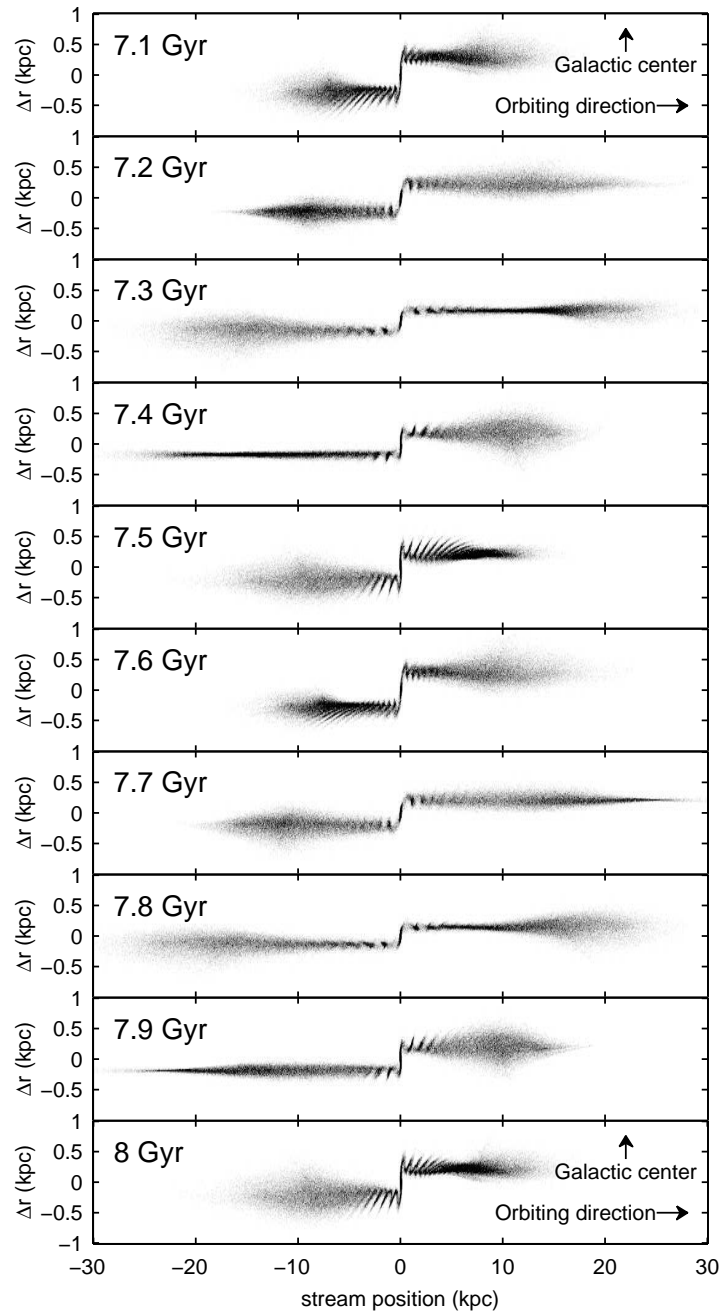


Figure 2.6: Surface density of the smooth stream from 7 to 8 Gyr projected onto the xy -plane. The stream is then aligned to Cartesian coordinates where the horizontal axis is the offset position along the stream from the progenitor, and the vertical axis is the radial offset from the galactocentric distance of the progenitor. This is done by tracing a best fit line along the stream. For each segment in the line, the particles in between the end points of the segment are rotated such that the Galactic center points toward the $+y$ direction in this plot. Note that the vertical axis has been scaled 30 times the larger than the horizontal axis.

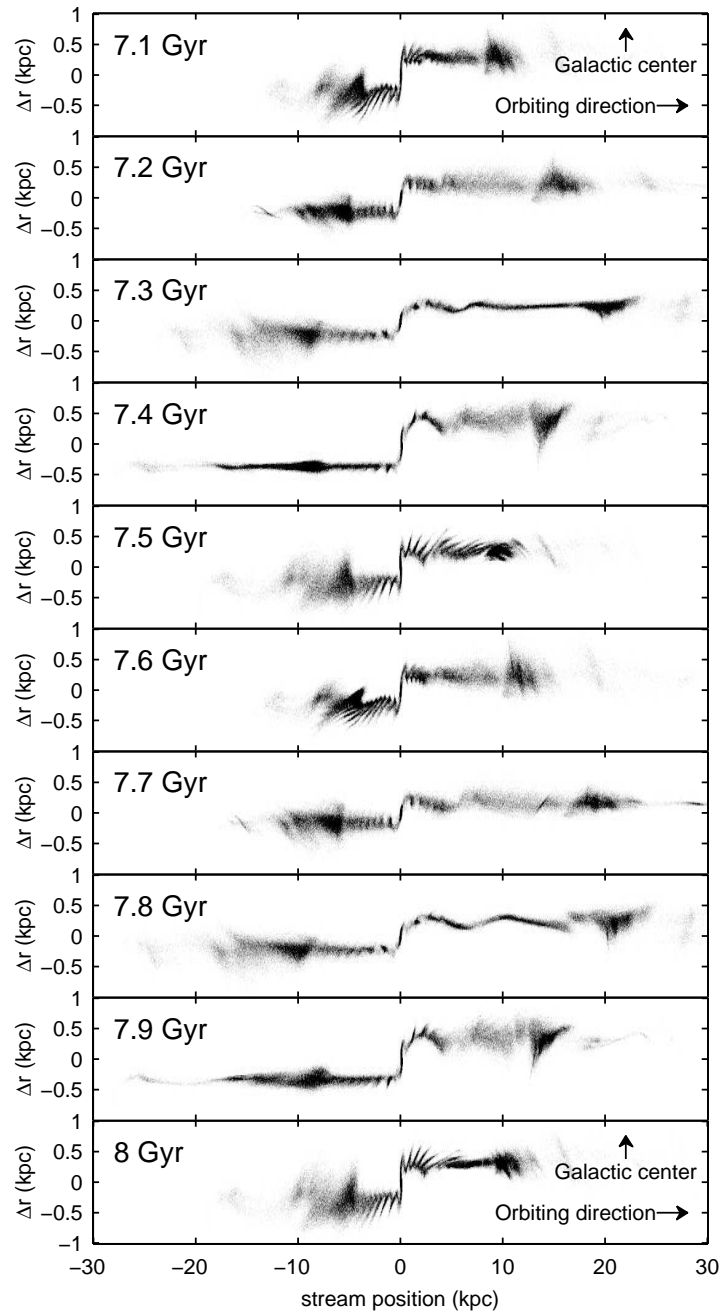


Figure 2.7: Stream with $5.8 \times 10^6 < M/M_\odot < 10^8$ subhalos from 7 to 8 Gyr, aligned to Cartesian coordinates similar to the smooth stream in Figure 2.6. Compared to the smooth stream, this Λ CDM stream shows much more structures at various scales. In general, whether by EOs (mostly inside ± 5 kpc) or by subhalo perturbations, gaps have complicated morphologies and do not even have straight edges across the width of the stream.

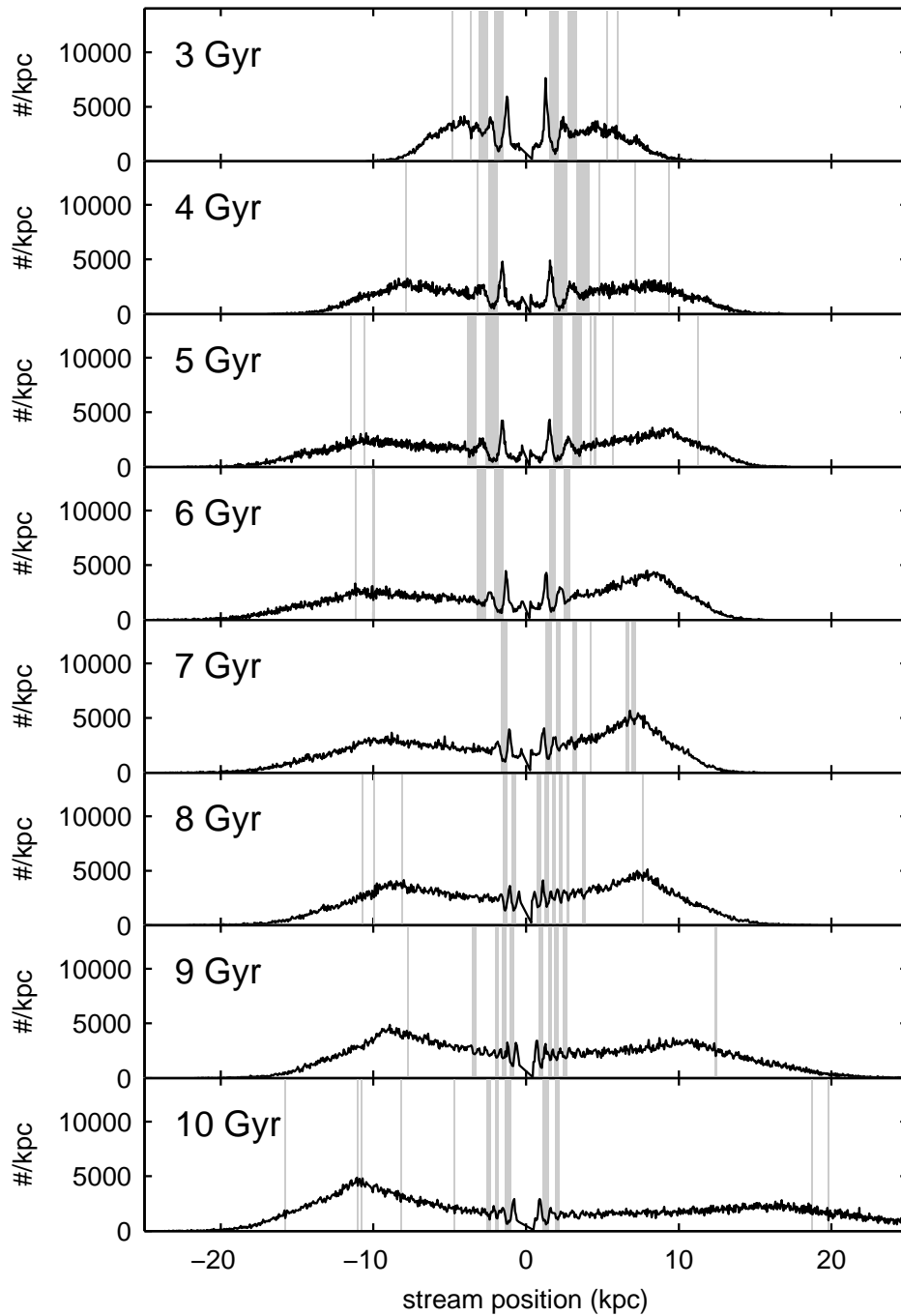


Figure 2.8: Linear densities along the smooth stream, integrated for the whole thickness of the stream, from 3 to 8 Gyr. The progenitor is centered at 0 kpc and is masked out. Shaded columns are gaps identified at 99% confidence at the scale depicted by the columns' widths.

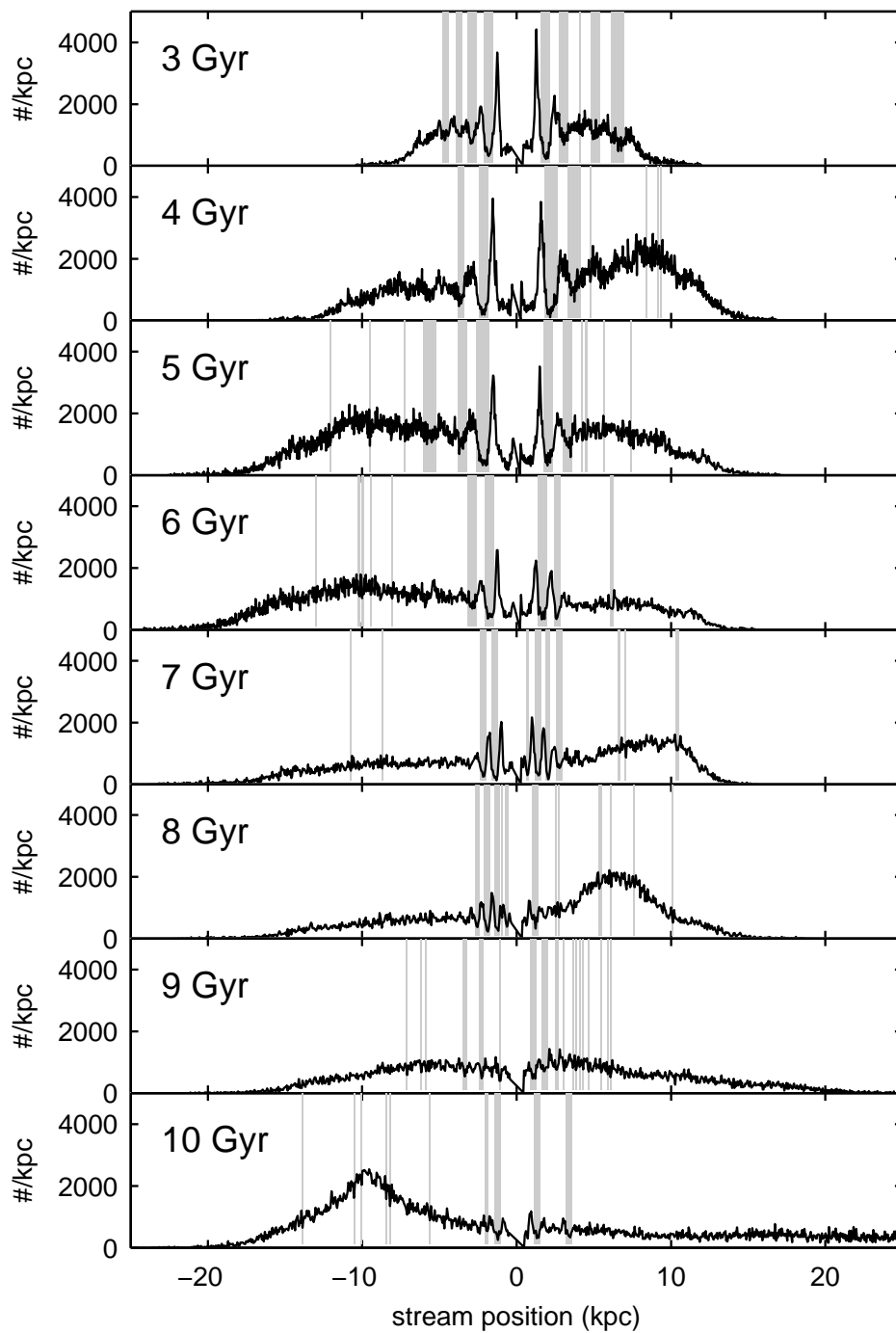


Figure 2.9: Linear densities and gaps identified at 99% in the smooth stream, but integrated for only a cylinder of diameter 0.08 kpc along the central line of the stream.

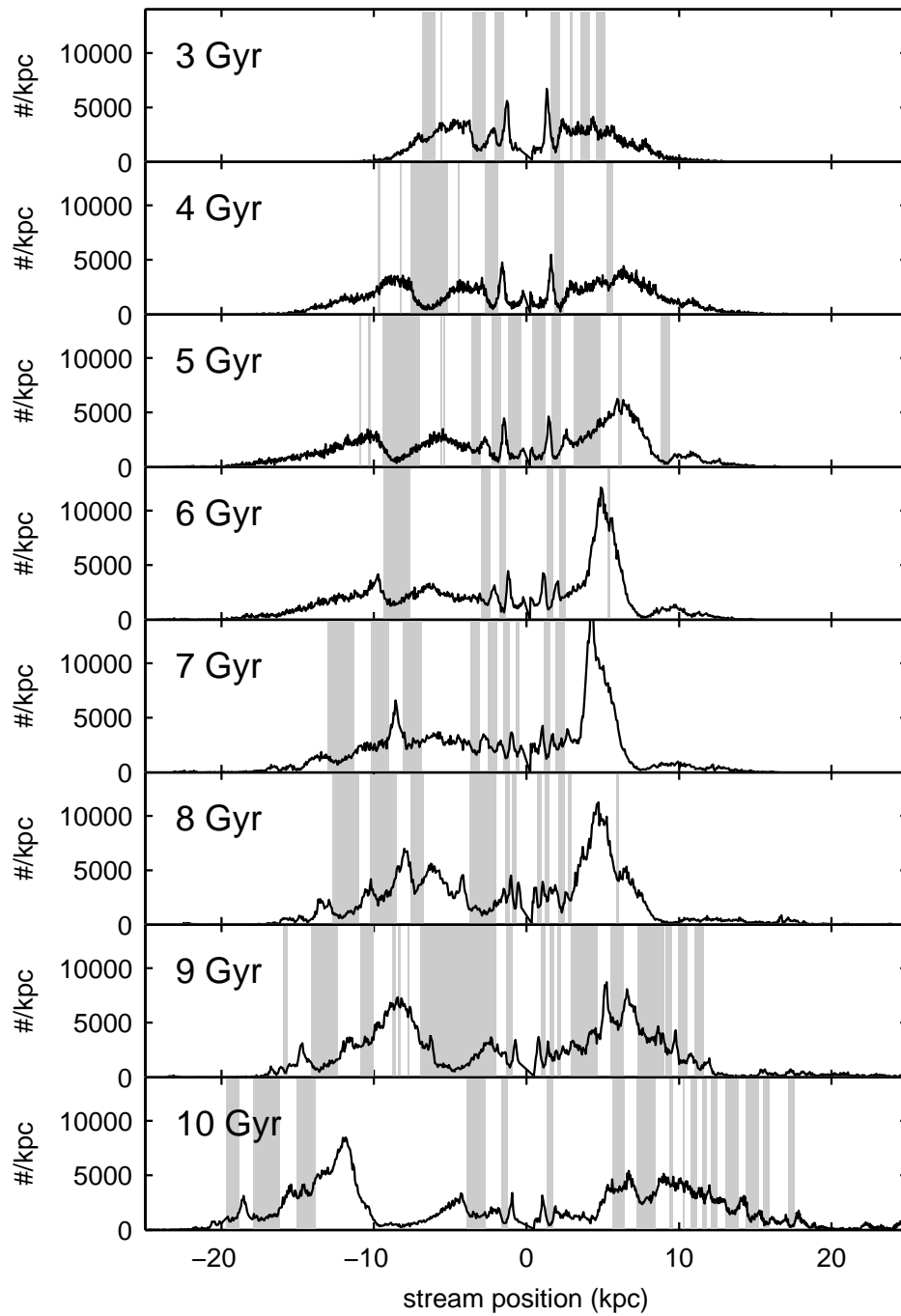


Figure 2.10: Linear densities and gaps identified at 99% in the Λ CDM stream with subhalo masses $6.5 \times 10^4 < M/M_{\odot} < 10^8$, integrated for the whole thickness of the stream.

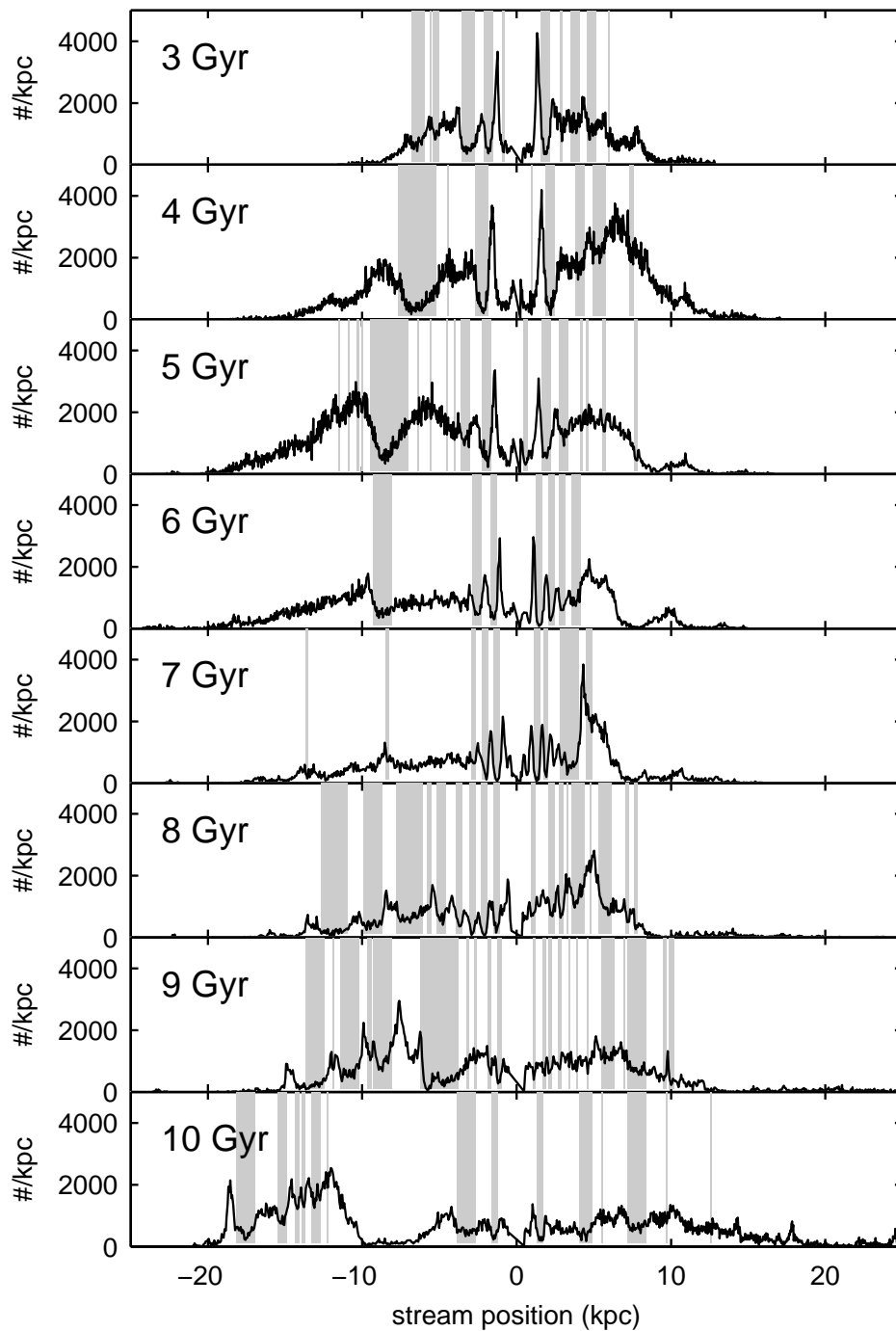


Figure 2.11: Linear densities and gaps identified at 99% in the Λ CDM stream with subhalo masses $6.5 \times 10^4 < M/M_{\odot} < 10^8$, integrate for only a cylinder of diameter 0.08 kpc along the central line of the stream.

this section we aim to study the validity of Equation (2.12) in our self-consistent stream. We set the “length” of each gap as the scale s of the matched filter which identified the gap (Section 2.3.2)

Smooth Stream without Subhalos

Figures 2.8 and 2.9 show the gaps identified in the smooth stream integrated using the whole thickness and central thickness, respectively. Clearly, the gaps due to EOs are clustered at $\lesssim 5$ kpc on both sides of the progenitor, and all the gaps have very similar sizes. The measured R_{\cup} would peak at short gaps and quickly drops off beyond $l \gtrsim 1$ kpc. Equation (2.12) is meant to describe an idealized gap spectrum produced by subhalos and not by EOs; however, as we show later in this chapter, the locations and sizes of EOs are key to distinguishing the gaps caused by EOs from those by subhalos.

Λ CDM Stream with Independent Sets of Subhalos

As an ideal case, Equation (2.12) ignores the visibility of gaps when the same position of a stream suffers impacts by multiple subhalos at different times. For instance, after one major impact by a massive subhalo which results in a long and high contrast density gap at an early time, subsequent impacts by less massive subhalos in that same region at a later time may not be visible.

Gap overlapping can be minimized by the following experiment. We run 13 separate simulations with the same initial conditions as the star cluster, but the subhalo masses are selected differentially from Table 2.1. In other words, the first simulation has subhalo of masses from $5.3 \times 10^7 M_{\odot}$ to $10^8 M_{\odot}$ (30 subhalos), the second from $2.7 \times 10^7 M_{\odot}$ to $5.3 \times 10^7 M_{\odot}$ (68 subhalos), and so on until the last simulation which has subhalos from $6.5 \times 10^4 M_{\odot}$ to $7.5 \times 10^4 M_{\odot}$ (3667 subhalos). This allows each stream to interact with an independent set of subhalos of a very small range of masses. Overlapping can still occur within the same simulation for each set of subhalos (hence a small number of gaps can still be eliminated), but to a much lesser extent than using integrated mass ranges.

Figure 2.12 shows the measured gap spectrum from the gaps collected from all 13 simulations using independent sets of subhalos. In the top panel which includes all gaps, the measured gap spectrum matches Equation (2.12) reasonably well. However, this is a coincidence as the gaps contain EOs which are not described by Equation (2.12). In an attempt to eliminate EOs, in the bottom panel of Figure 2.12, the gaps that are located within 5 kpc away from the progenitor are eliminated. When computing the gap formation rates in these cases, the number of gaps are divided by a stream length which is reduced by 10 kpc and a stream age which reduced by 2 Gyr (i.e., the age of the stream when it is 10 kpc long). This allows us to facilitate a fair comparison of gap spectra against the cases which include all gaps in the entire stream. Comparing the two panels in Figure 2.12, we can see the masking of the 10 kpc around the progenitor reduces the abundance of shorter gaps. This is expected since that region of the stream contains mostly EOs which occur at scales $\lesssim 1$ kpc. In general it is difficult to tell whether a given gap within 5 kpc is due to EOs or subhalos, so in the process some subhalo gaps near the progenitor may have been eliminated as well.

Whether Equation (2.12) is a good description of the gap spectrum in a general stream likely requires more simulations with varying orbital parameters. Nevertheless, it is apparent that the gap spectrum does not depend strongly on the age or the integrating width for the linear density of the stream. However, it is still an ideal case since a stream realistically interacts with all the subhalos at the same time. As we show in the following section, gap overlapping can significantly alter the gap spectrum.

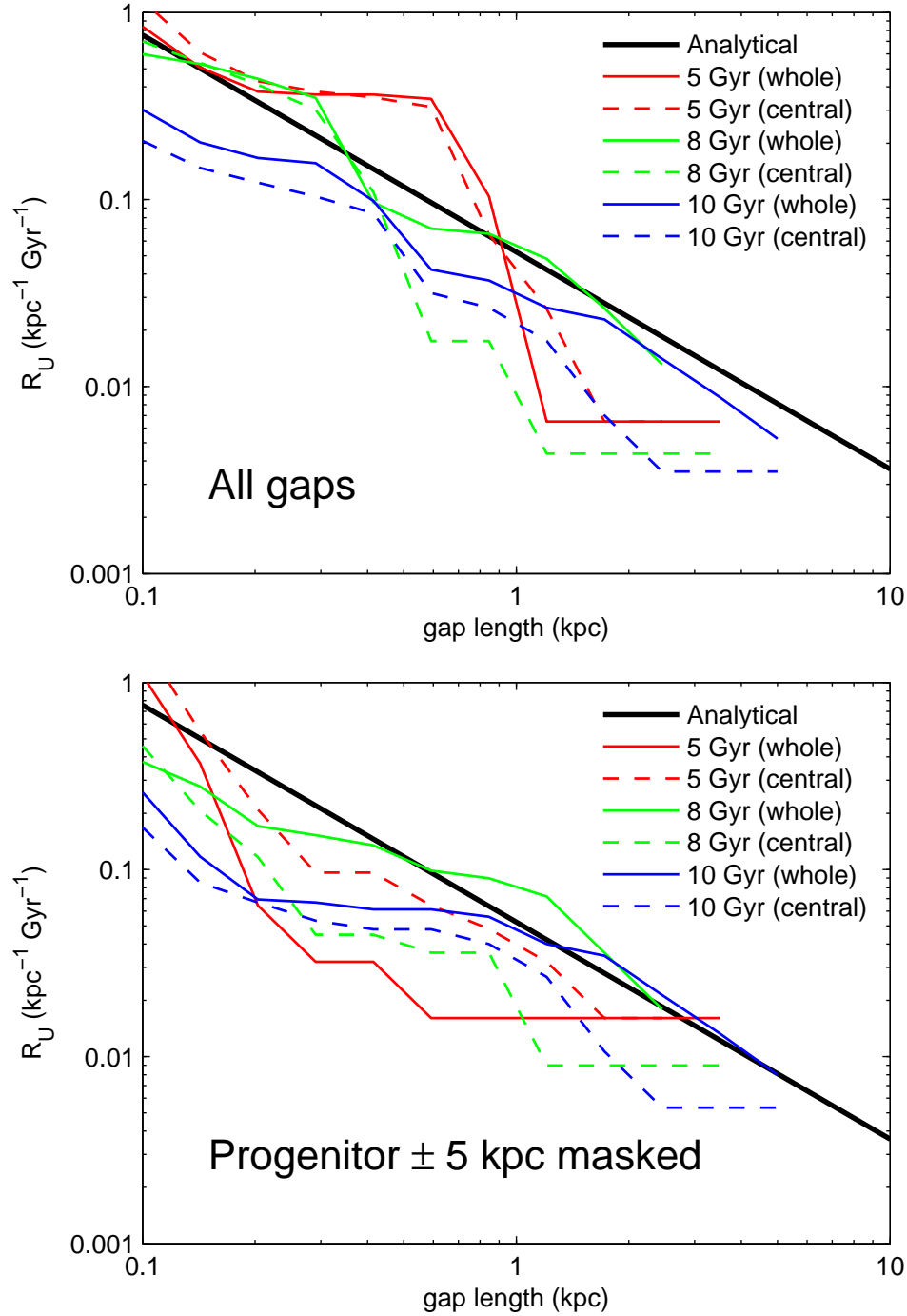


Figure 2.12: Analytical (Carlberg, 2012) and simulated gap spectra. The gaps are collected from 13 simulations with independent sets of subhalos selected differentially from the mass ranges in Table 2.1. In the top panel, all gaps identified (including EOs) are included in the measured gap spectra. In the bottom panel, the gaps located within 5 kpc away from the progenitor are eliminated, and the stream lengths and ages are adjusted. The gap spectra here roughly follow the analytical prediction, but with large deviations as this is only one realization. Later in this chapter we show the median gap spectra from many realizations.

Λ CDM Stream with all Subhalos

We now consider the validity of Equation (2.12) for stream gaps in the presence of all subhalos in each cumulative mass range in Table 2.1. Figure 2.13 compares the measured gap spectra of both the whole and central streams for three mass ranges, with and without the gaps within 5 kpc away from the progenitor. Clearly in all cases, the ideal gap spectrum over estimates the measured spectrum by nearly an order of magnitude due to gap overlapping.

Similar to the simulations with independent sets of subhalos (Figure 2.12), the gap spectra produced by full sets of subhalos do not have strong dependence on stream age and integrating width. The only exception is the youngest stream shown at 5 Gyr which consistently has higher R_U than the older streams. However, when the gaps near the progenitor are eliminated, the numbers of gaps at 5 Gyr in all cases decrease significantly, where the gap spectra are dominated by a single gap at 2 – 3 kpc, and a number of extremely short gaps. This is likely because the stream is still young, and the effective length of the stream (after masking 10 kpc centered at the progenitor) is only ~ 15 kpc. This eliminates a significant part of the stream, making its stream statistics unreliable.

The weak dependence of the gap spectrum on the integrating width for linear density is also worth noting. Figure 2.7 shows that gaps in general have much more complicated morphologies than straight edges across the width of the stream. The explanation for these morphologies requires detailed understanding of how subhalo perturbations manifest in a self-consistent stream, which is beyond the scope of this chapter. While Carlberg (2013) studied the dynamics of subhalo perturbations for an idealized stream, we defer the self-consistent case to a future study.

Perhaps the most surprising result is that the gap spectra do not show obvious dependence on subhalo masses. The spectra are difficult to distinguish between the mass range of subhalos which causes the gaps. This is in disagreement with Carlberg (2012) which derived a relation between the length of a gap and the mass of the subhalo that caused it such that

$$l(M) = 8.3 \left(\frac{r}{30 \text{ kpc}} \right)^{0.37} \left(\frac{M}{10^8 M_\odot} \right)^{0.41} \text{ kpc}. \quad (2.13)$$

From this formula, it is reasonable to expect the inclusion of lower-mass subhalos to show more gaps at the shorter end. In their ideal simulations, however, Carlberg (2012) did not account for the time evolution of each gap. An example can be seen in Figures 2.10 and 2.11. The gap located at about -7 kpc at 4 Gyr evolves into a much longer gap centered at about -9 kpc at 10 Gyr. Evidently Equation (2.13) requires revision for self-consistent streams before it can be used to understand the relation between gap spectra and subhalo masses.

2.4.4 Observational Considerations

We now consider the issues when interpreting gap spectra from observations. A gap spectrum for GD-1 has been observed by Carlberg & Grillmair (2013), but we emphasize that the gap spectra from our simulated streams in this chapter should not be rigorously compared to the one in Carlberg & Grillmair (2013) because our models for both the star cluster and the galaxy halo are chosen in favor of a simple interpretation, and may be missing some complications discussed in Section 2.4.6. Nevertheless, we discuss a preliminary comparison later in this section.

We first project each stream onto sky coordinates. For simplicity, we put the hypothetical observer

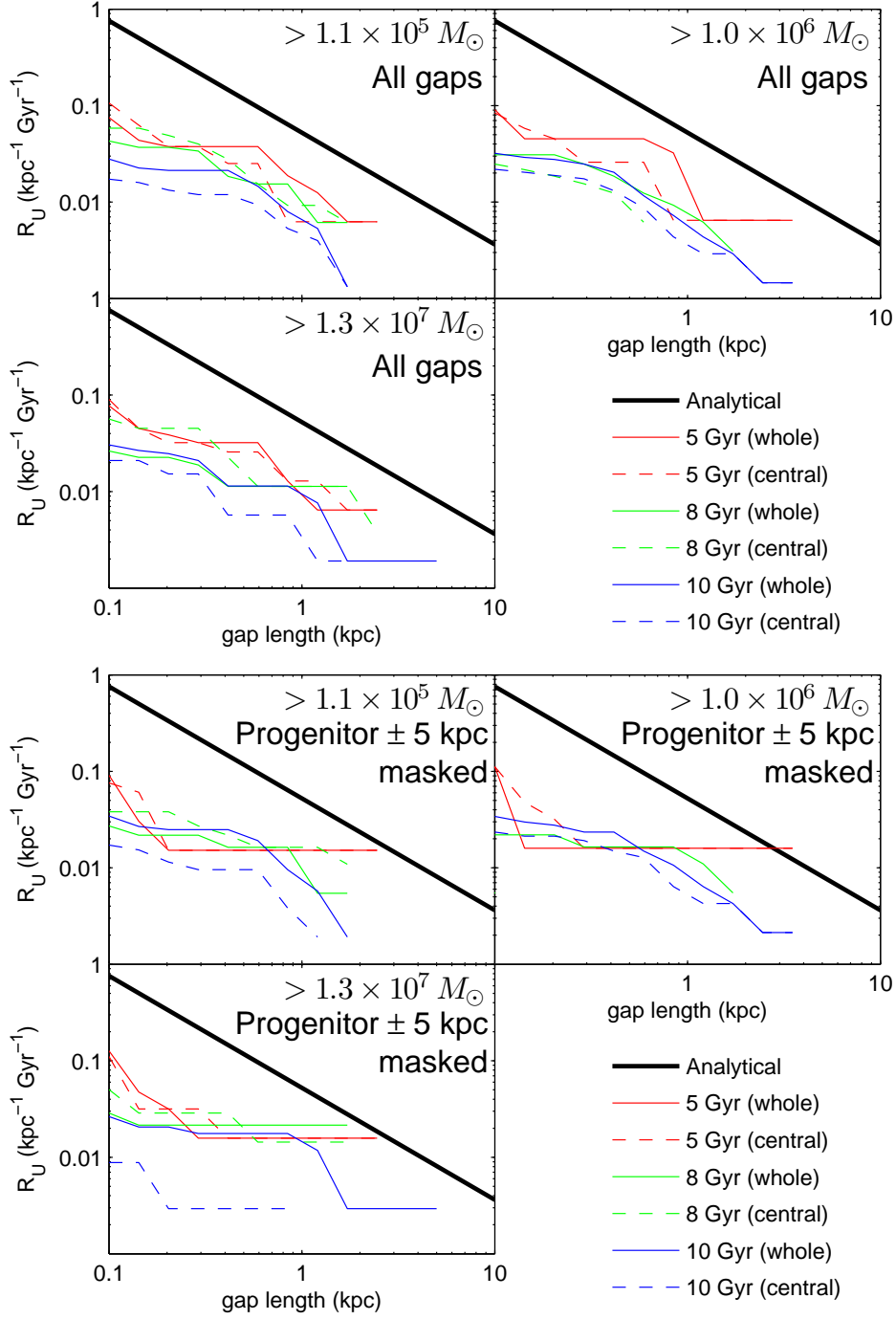


Figure 2.13: Analytical (Carlberg, 2012) and simulated gap spectra. The gaps are collected from single simulations which include the full ranges of subhalos. The lower limit of the mass range is labeled in each panel, and the upper limit is $10^8 M_\odot$ in all cases. In the top three panels, all gaps identified (including EOs) are included in gap spectrum. In the bottom three panels, the gaps located within 5 kpc away from the progenitor are eliminated, and the stream lengths and ages are adjusted. Compared to Figure 2.12, the simulated gap spectra here no longer follow the analytical prediction because of overlapping between the gaps.

at the center of the galaxy, and then project each particle onto the azimuthal and altitudinal plane in galactocentric coordinates. Since the our stream progenitor is orbiting along the xy -plane in a spherical potential, the smooth stream appears as a straight line along the azimuthal direction, and each Λ CDM stream appears only a few degrees off the azimuthal plane due to subhalo perturbations.

The density along the stream is simply the number of particles in bins of 0.1° in the azimuthal direction. The match filter approach to detect gaps remain the same as the analysis above, but the 12 filter scales (Figure 2.5) are now logarithmically spaced in angular units from 0.34° to 14° , and the noise levels are obtained from the regions at $> 10^\circ$, rather than > 5 kpc, away from the progenitor. The choice of bin size and filter scales are on the same orders of magnitude as Carlberg & Grillmair (2013), but putting the hypothetical observer at the Galactic center may affect angular sizes by factors of ~ 2 .

To ensure that the behaviors of the simulated streams are typical, we simulate each Λ CDM stream 10 times with the same initial conditions for the star cluster, but different realizations of the same subhalo distributions. At the end we take the median numbers of gaps of the 10 streams to avoid outliers.

Orbital Phase

One surprising result from Section 2.4.3 is that the gap spectrum has little to no dependence on age and subhalo masses. To investigate what this means when interpreting observations, the top panel of Figure 2.14 shows the cumulative numbers of gaps longer than 0.34° (i.e., all gaps detected in the entire stream) as a function of time. At $t > 5$ Gyr, the numbers of gaps due to subhalos vary according to the orbital phase of the stream progenitor. The “bursts” in numbers of gaps in the Λ CDM streams occur when the streams are stretched as they pass through the pericenters of their orbits. At $t < 5$ Gyr, on the other hand, this correlation does not exist for two reasons. First, our detection method (Section 2.3.2) uses the parts of the stream that are > 5 kpc (before sky projection) or $> 10^\circ$ (after sky projection) away from the progenitor in order to estimate noise. At $t < 5$ Gyr, the length of the stream varies between a few to 20 kpc, which may not be long enough to estimate noise. Second, in only 5 Gyr the stream does not yet have enough time and to interact with subhalos.

Both the total number of gaps and the dynamical age of the stream are difficult to measure, as some parts of a stream may not be observable. We define a more useful quantity S_{\cup} which is the cumulative number of gaps longer than a given gap length per unit stream length. In other words, leaving the age of the stream as an unknown, S_{\cup} differs from R_{\cup} in Section 2.4.3 by a normalization by age, and that S_{\cup} is after sky projection. In the next section we show that gaps due to EOs and subhalos have very different $S_{\cup}(l)$ distributions which are directly observable.

Signal-to-noise Ratios

Another important distinction between simulations and observations is the signal-to-noise ratio (S/N). At 5 and 8 Gyr our smooth stream is represented by about 60,000 and 80,000 particles in total, respectively (Figure 2.2). Koposov et al. (2010) estimated that the 60° visible segment of GD-1 consists of 3000 stars. At an average distance of ~ 10 kpc, the visible segment is ~ 10 kpc long. In our simulations, after 5 and 8 Gyr, the average stream lengths are about 20 and 40 kpc, respectively (Figure 2.2). This means that our simulated stream should be represented with about eight times fewer particles in order to be comparable to observations. With the progenitor masked, we reduce the number of particles in the stream by randomly sampling the stream using two, four, and eight times fewer particles than the

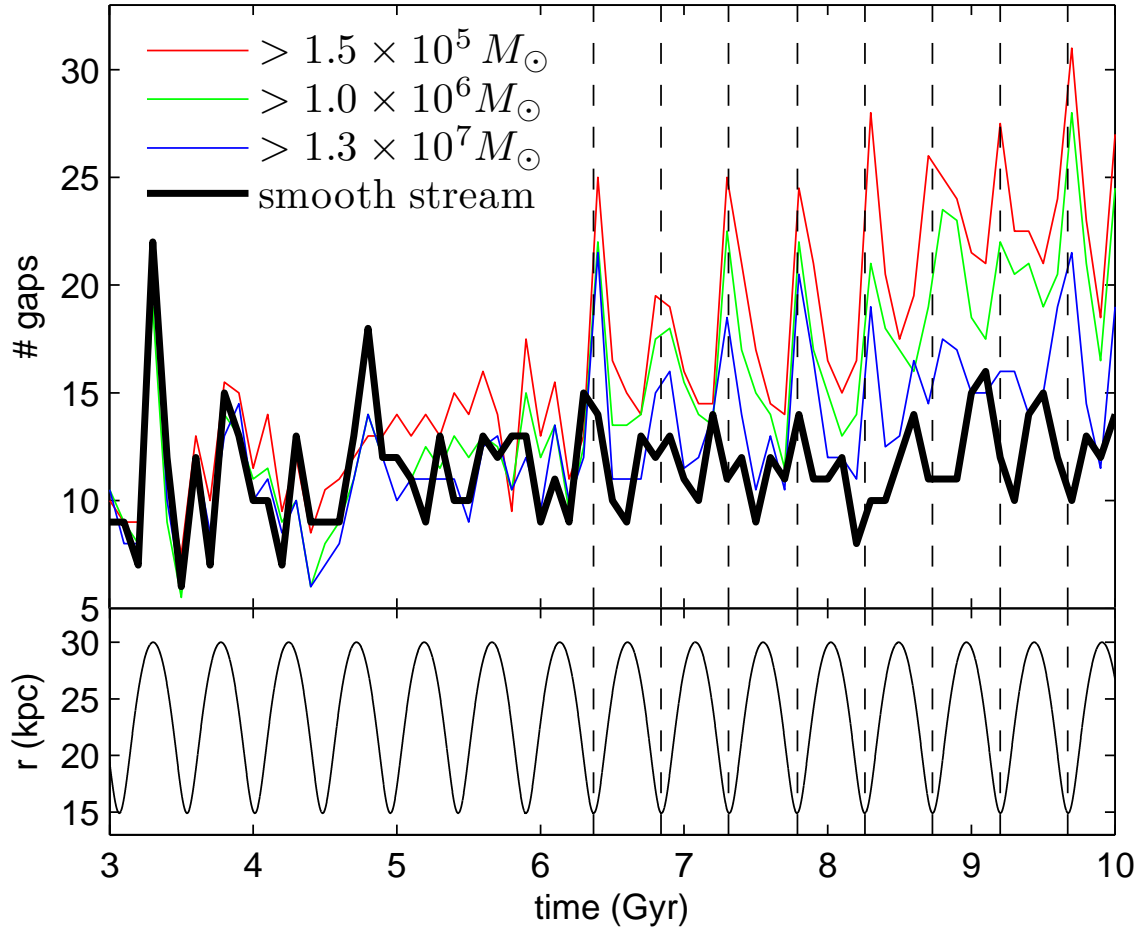


Figure 2.14: Top: time evolution of the number of gaps longer than 0.34° . Each colored line represents the median of 10 realizations of an identical subhalo distribution (with $10^8 M_\odot$ as upper mass limit), and the black thick line represents the smooth stream. Bottom: the vertical dashed lines are visual guides which show that the variation of the number of gaps are correlated with the orbital phase of the stream progenitor. These plots show that the cumulative number of gaps in a stream on average is increasing in time, but instantaneously the number of gaps observable can have an even stronger dependence on the orbital phase of the stream than on the stream’s dynamical age or subhalo masses.

original stream. The particle reduction applies to both the stream of interest and the smooth stream which is the source for estimating noise. This allows us to investigate the importance of high S/N.

Note that in our simulation each particle is equivalent to about $0.043M_{\odot}$, which is less massive than the typical stars that are detected in observations. Our simulations are not meant to be physical models of the real stream. In this section, we are only concerned about matching the numbers of particles in the simulations to the numbers of stars in the observation. As the stars escape from the progenitor, the stream’s self-gravity becomes negligible (Johnston, 1998), and the particles’ masses are no longer important.

Figure 2.15 shows the density profiles of the Λ CDM stream with subhalo masses $1.5 \times 10^5 < M/M_{\odot} < 10^8$ at 8 Gyr projected onto the sky. The panels show the gaps detected in the same stream after three levels of particle reduction. Even after reduction by a factor of eight, the stream appears to have retained most of its gaps despite a lower S/N.

In Figure 2.16, each line shows the median of ten gap spectra from the same stream but with 10 realizations of the same subhalo distribution. In each panel, the solid (dashed) lines represent the times when the progenitor is at the pericenter (apocenter) of its orbit. When the stream is compressed and stretched as it oscillates radially (see Figure 2.2), its length can differ by up to a factor of two. Careful inspection of Figures 2.14 and 2.16 shows that during pericentric passages, the numbers of gaps are at maximum, but S_{\perp} is at minimum because the stream length is also at maximum. For a Λ CDM stream at high S/N (upper left panel in Figure 2.16), the gap spectra are not sensitive to this oscillation, except with an excess of shorter gaps and fewer longer gaps, which are expected as the stream, including its longitudinal structure, is compressed during apocentric passage. At low S/N (lower left panel in Figure 2.16), however, the gap spectrum during apocentric passage is consistently higher than that during pericentric passage. This is because the length of the stream is insensitive to the S/N, but the number of gaps is not. Therefore, high S/N data for the stream is important when studying stream gaps. Otherwise, the spectrum may be over- or underestimated depending on the orbital phase.

The right panels in Figure 2.16 show the gap spectra of the smooth stream. They are also somewhat sensitive to S/N, but the most obvious difference from the spectra of Λ CDM stream is the shape of the spectra. This is especially obvious during pericentric passage where the gap spectra rapidly drop off to zero for gaps longer than $\sim 1^{\circ}$. Even during apocentric passage, the gap spectra remain flat at gap lengths $\gtrsim 1^{\circ}$. If the gaps originated from subhalo perturbations, then the gap spectrum should be steep and extend well beyond 1° .

The Case of GD-1

An interesting confusion for GD-1 in particular is that GD-1’s progenitor has not been identified. If GD-1’s progenitor has evaded observation, and the observation corresponds to a segment of the stream which is close enough to the progenitor such that EOs can be observed, then GD-1 may be a poor choice as a probe for missing satellites. However, this is unlikely because EOs are observable only in a small segment of the stream, and subhalo gaps are observable everywhere along the stream.

Another possibility is that GD-1’s progenitor may have been completely disrupted. In this case, the tidal radius of the progenitor approaches zero. Since the spacing between EOs are proportional to the tidal radius of the progenitor, this means that the EOs should also fade away as the progenitor is disrupted (Küpper et al., 2010). Therefore, despite its lack of progenitor GD-1 should be a viable probe for missing satellites.

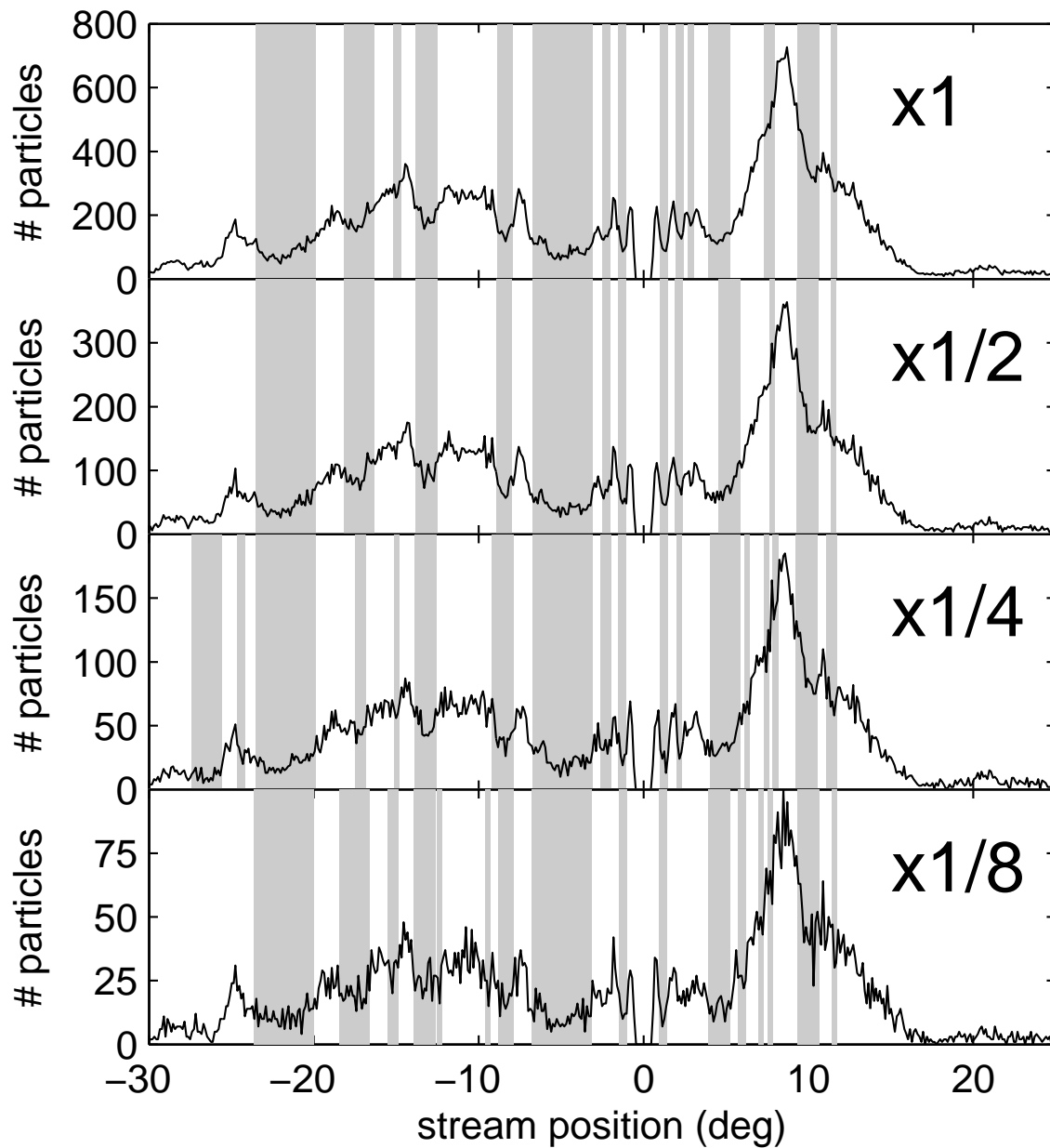


Figure 2.15: Density profiles and gaps detected at 99% confidence for the Λ CDM stream with subhalos of masses $1.5 \times 10^5 < M/M_\odot < 10^8$ at 8 Gyr, projected onto the sky. Each panel represents a stream whose number of particles have been reduced by the factor indicated and binned at 0.1° throughout. Without reduction (top panel), the stream contains about 80,000 particles. The stream retains most of its gaps even after particle reduction by a factor of eight.

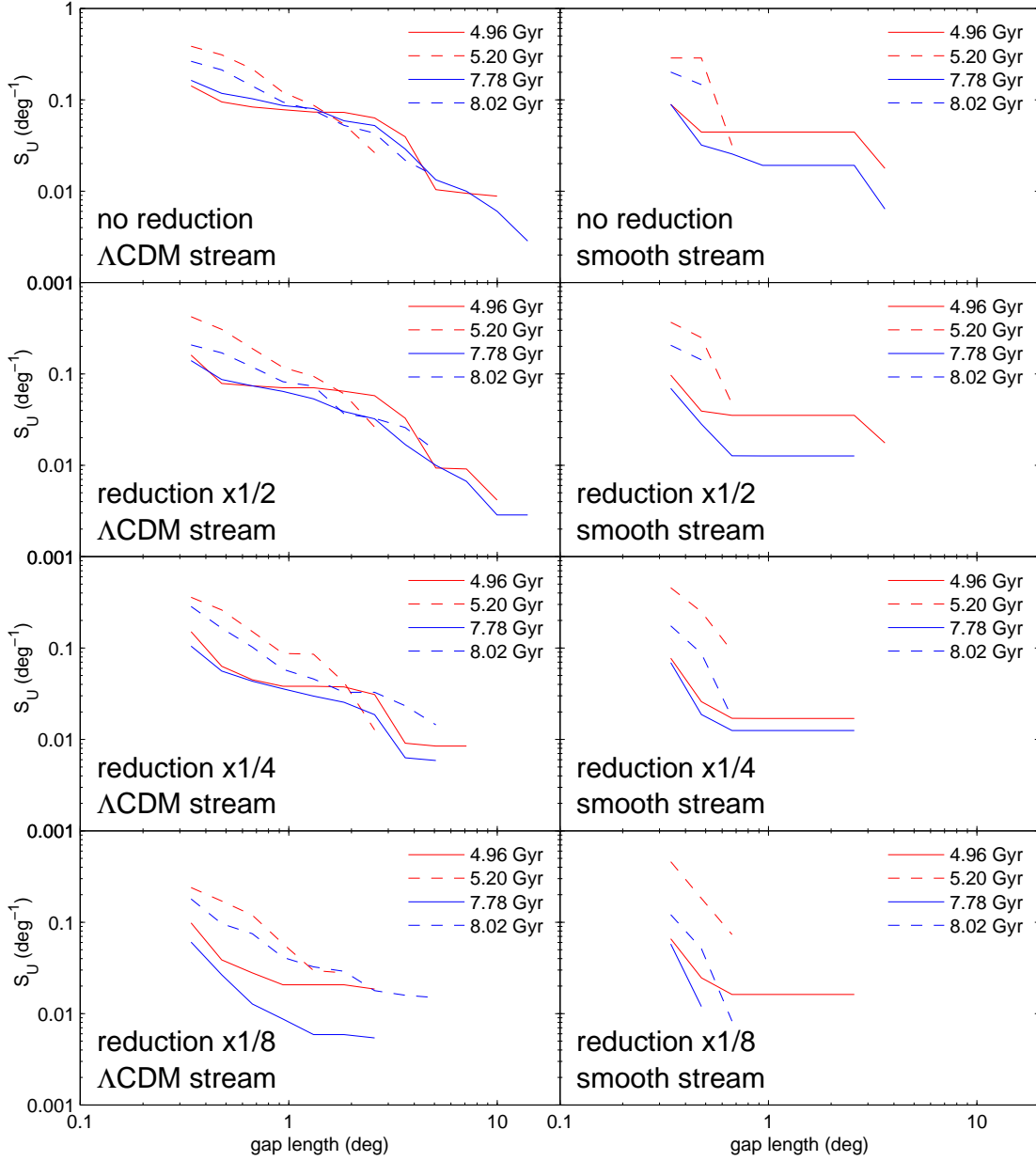


Figure 2.16: Gap spectra from simulated streams after sky projection. Each line in the panels on the left are the median of 10 spectra of the same Λ CDM stream but with ten identical subhalos distribution of masses $1.5 \times 10^5 < M/M_\odot < 10^8$. The panels on the right are the spectra of the smooth stream. The spectra of the Λ CDM stream show presence of gaps longer than 1° , whereas the spectra of the smooth stream quickly drops off. Colored solid (dashed) lines are spectra obtained when the stream is undergoing pericentric (apocentric) passage. Each row represents the spectra after the numbers of particles in the streams have been reduced by the factor labeled. The bottom panels indicate that a high S/N detection of the stream is important for understanding the origins of gaps, otherwise the gap formation rates can be systematically biased depending on the stream’s orbital phase.

The gap spectrum of GD-1 has been measured by Carlberg & Grillmair (2013). The spectrum show presence of gaps at all lengths between 0.2° and 10° , which is sufficient to rule out a smooth and spherical potential. Adopting an average length of 40 kpc (Figure 2.6) and an average distance of 22 kpc, the average stream length is $\sim 100^\circ$ as seen from the center of the galaxy. Multiplying the stream length by S_{\cup} in Figure 2.16, the number of gaps longer than 1° is on the order of a few. This roughly corresponds to the level seen in GD-1. However, to facilitate a conclusive analysis on the origin of the gaps in GD-1, we need to consider a much more realistic model which include the effects discussed in Section 2.4.6, as well as Chapters 3 and 4.

2.4.5 Subhalo Mass Limits

We consider the effects of subhalos as massive as $10^8 M_{\odot}$, since the effects of more massive subhalos are not relevant to us. Gaps caused by subhalos at these masses produce long gaps with high-density contrasts. For example, an obvious gap located at -7 kpc at 4 Gyr shown in Figures 2.10 and 2.11 are caused by a $4.5 \times 10^7 M_{\odot}$ subhalo. In fact, the perturbation by $M \gtrsim 10^8 M_{\odot}$ ($h \gtrsim 1$ kpc) subhalos can be so catastrophic that the stream is warped and divided into segments. As a result, a stream which originated from one progenitor can be observed as a few separate streams. Observations of Pal-5’s and GD-1’s gaps, on the other hand, show small-scale density fluctuations in a long, narrow stream, so these two streams are not sensitive to subhalos above $10^8 M_{\odot}$. By coincidence, this upper limit approximately coincides with the upper limit beyond which the models of warm dark matter can be no longer be distinguished from CDM. Therefore, $10^8 M_{\odot}$ is a reasonable upper limit where our simulations can be useful.

In the low-mass end, we only consider the effects of subhalos down to $\sim 6 \times 10^4 M_{\odot}$. From a separate simulation of the same stream but with only the subhalos with masses $6.5 \times 10^4 < M/M_{\odot} < 7.5 \times 10^4$, the density profile is indistinguishable from the smooth stream, and the gap statistics are identical. Furthermore, Section 2.4.3 shows that the gap spectra have very little dependence on mass. Changing the mass lower limit from $7.5 \times 10^4 M_{\odot}$ to $6.5 \times 10^4 M_{\odot}$ produced indistinguishable gap spectra. This means that subhalos less massive than $\sim 10^5 M_{\odot}$, even though they are much more abundant than those of higher masses (Equation 2.3), have minimal effects on our stream.

The Milky Way has about 160 known globular clusters (Harris, 1996), and a few hundred dwarf galaxies brighter than $L \gtrsim 10^3 L_{\odot}$ after bias corrections (see Bullock (2010) for a review). It is interesting to ask whether these known satellite systems, rather than the truly “missing” satellites, can contribute to the observed stream gaps. Typical globular clusters have masses $\sim 10^5 M_{\odot}$, which correspond to the low end of our mass spectrum of subhalos. In the same mass range, though, there are orders of magnitudes more subhalos (e.g., $\sim 10^5$ subhalos at $10^5 < M/M_{\odot} < 10^6$) than globular clusters, so globular clusters are unlikely to contribute significantly to observed stream gaps. On the other hand, dwarf galaxies are commonly found at $\gtrsim 10^7 M_{\odot}$ (Strigari et al., 2008) which is the high end of our mass spectrum of subhalos. At that mass range (~ 2000 subhalos at $M > 10^7 M_{\odot}$), the number of known dwarf galaxies are only 1 order of magnitude below the number of subhalos, so dwarf galaxies may contribute to some observed gaps. However, a common limitation in understanding the contributions from both globular clusters and dwarf galaxies is their orbits, especially when the kinematics of these satellites are not well constrained. As done in our simulations (Section 2.3.1), subhalos that do not approach the stream’s orbit will interact minimally with the stream. Table 2.1 shows that in our realizations of subhalos, only $\sim 15\%$ of them would approach to within 2 kpc of GD-1’s orbit. This means that most known satellites

may never interact with a GD-1-like stream, and that stream gaps, if they were indeed due to satellites and were not EOs, are more likely due to satellites that have never been observed.

2.4.6 Other Effects

In order to keep our results simple, the galaxy is modeled as a stationary, spherical NFW potential, the subhalos as static, test masses, and the satellite as a collisionless King model. These models ignore a number of known dynamical complications.

Two-body Relaxation: The star cluster is modeled as a collisionless system with relaxation timescale of ~ 110 Gyr. Globular clusters typically have relaxation timescales of $\lesssim 10$ Gyr (Harris, 1996, 2010 Edition), so mass loss should originate from dynamical evaporation, in addition to tidal disruption. As a result, the star cluster should be disrupted even faster than we measured in Figure 2.2. This may have an important effect on the formation of gaps, which depends on the details of the dynamics of a stream (Carlberg, 2013). The relation between gaps and mass loss mechanism will be investigated in a future study.

Dynamical Friction (DF): Both the star cluster and subhalos should suffer from DF as they orbit around the dark matter halo. Comparing the magnitudes of the accelerations due to DF and due to the orbit, $a_{DF}/a_{orbit} \sim 10^{-8} \ln \Lambda$ for both the star cluster at 22 kpc and a $10^6 M_\odot$ subhalo at 100 kpc, where $\ln \Lambda \equiv \ln(b_{max}/b_{min}) \approx 10$ is the log of the ratio of the maximum and minimum impact distances (Binney & Tremaine, 2008). Therefore, DF is negligible throughout our model.

Disk Shocking: Dehnen et al. (2004) found that the evolution of Pal-5 is driven by the tidal shocks when crossing the Galactic disk, which is not modeled in our simulations. The orbit of Pal-5 in Dehnen et al. (2004) has peri- and apogalacticon at 5.5 kpc and 19 kpc, respectively, whereas our smooth stream has peri- and apogalacticon at 15 kpc and 30 kpc, respectively. Being farther away from the the Galactic center, if our simulations contained a disk, its effect should be less severe for our simulated stream than Pal-5. Moreover, Dehnen et al. (2004) concluded that disk shocking is not responsible for the observed structure in Pal-5, while Küpper et al. (2010) concluded that EOs persist even under the influence of disk shocks, so the absence of a disk should not significantly change our conclusion. The gap formation rate with and without subhalos in the presence of a disk is beyond the scope of this chapter.

Halo Shape and Collapse History: Siegal-Gaskins & Valluri (2008) found that the shape of the halo potential can have a larger effect than subhalos have on the over all structure of a stream. However, their simulations focused on streams which originated from dwarf galaxies at $\sim 10^9 M_\odot$, as well as subhalos at $\gtrsim 10^7 M_\odot$ which is the high end of our mass spectrum of subhalos. In fact, since the initial collapse of the entire halo, the potential cannot be stationary throughout a Hubble time, which is the timescale of our simulations. In Chapter 3, we repeat a similar study using the potentials which resulted directly from high resolution the Via Lactea II simulation (Madau et al., 2008) at redshift zero. The self-consistent halo and subhalo potentials from those simulations can eliminate the idealized models in Section 2.2.1.

2.5 Chapter Summary

For the first time, we used N-body simulations to model the disruption of a collisionless star cluster which formed a narrow stream similar to Pal-5 and GD-1, and we investigated the phenomenology of gaps that originated from the perturbations by subhalos predicted in the Λ CDM cosmological model. Analytical predictions of stream gap statistics in previous studies were all based on massless particles distributed to mock realistic streams, but the dynamics of gaps have never been studied in self-consistent models. With a stream from a self-consistent model, we characterized the gap length distribution which can be used as a tool to understand the origin of stream gaps seen in observations.

The properties of the subhalos in our simulations were approximations to those in the Aquarius simulation (Springel et al., 2008). We ran 14 simulations of the same stream – 1 without any subhalos (the smooth stream), and 1 for each cumulative mass range in Table 2.1 (the Λ CDM streams). In each stream we looked for gaps using a matched filter approach previously used by Carlberg et al. (2012) and Carlberg & Grillmair (2013). We found that, in addition to subhalo perturbations, the overdensities of particles due to their epicyclic motions as the progenitor loses mass (Küpper et al., 2008) can also produce gaps. Therefore, even without subhalos, “gaps” can appear within ~ 5 kpc away from the progenitor. For the first time, our match filter approach accounted for these EOs together with the gaps due to subhalo perturbations.

Yoon et al. (2011) first noted that subhalos gaps were typically diagonal and not perpendicular to the stream due to the range in angular momenta across the width of the stream. We investigated whether this could be a hindrance to gap detection. By measuring the distribution of angular momenta in our simulated stream, we estimated that the two ends of a gap across the width of a stream were sheared by no more than a 1 kpc per Gyr. Rather, subhalo gaps show complicated morphologies which were already imprinted into the stream as soon as the gaps first occurred. In addition to integrating the entire thickness of the stream, we also considered the case where the linear density are integrated using only the central 0.08 kpc of the stream in order to minimize the impact of gaps morphologies. We found that the resulting gap rate spectra the two cases were similar. Therefore, gap morphology does not affect our conclusion.

We tested the validity of the idealized gap spectrum R_{\cup} , or the cumulative number of gaps per unit stream length per unit stream age as a function of gap length l , derived by Carlberg (2012). We found that overlapping gaps in the stream can significantly reduce R_{\cup} , and that the dependences of R_{\cup} on subhalo masses and stream age are smaller than its dependence on the stream’s orbital phase. Therefore, the stream’s orbital phase must be known when interpreting gap formation rates in observations.

We considered how to interpret gap spectra from observations by projecting the stream onto the sky, and for each Λ CDM stream we also simulated them using ten realizations of the same subhalo distributions. One observational concern is the S/N of the stream’s detection. We down-sampled our simulated streams with less particles in order to match the S/N which is similar to the GD-1 detection (Carlberg & Grillmair, 2013). Our result indicated that at GD-1’s S/N, the gap spectrum can be biased by the orbital phase of the stream. In addition, we compared gap spectra produced purely by EOs and by EOs and subhalos together in a Λ CDM halo. We showed that the gap spectra of the former are limited in gap lengths, and that the latter have a much larger variety of gap lengths. This can be a powerful method to identify the origin of gaps in streams. Therefore, high S/N data such as those from *Gaia* will be very useful for using stream gaps to constraint the abundance of subhalos.

The dynamics of stream gaps depend on the details of the dynamics of the stream itself. We adapted

a few tools such as match filter and scaling relations which were derived from idealized simulations. In a future study, we aim to use self-consistent streams to repeat experiments akin to Yoon et al. (2011), Carlberg (2012), and Carlberg (2013), where the details of individual gaps can be studied in controlled experiments, in order to revise the aforementioned tools.

Chapter 3

Simulating Tidal Streams in a High-resolution Dark Matter Halo

Abstract

We simulate self-gravitating tidal streams in the potential of Via Lactea II (VL-2)—a high resolution Milky-Way-sized dark matter halo formed in a cosmological simulation using ~ 1 billion particles. We use a halo finder to extract the subhalos identified inside the VL-2 halo, and we model the potentials of VL-2 halo itself, as well as all the subhalos, using the self-consistent field (SCF) method. This allows us to compare streams in the presence and absence of subhalos inside a realistic halo potential. For each case we simulate two streams, which originate from the same star cluster in the same initial orbital position, but with different velocities. Although these two orbits are only moderately eccentric and have similar apo- and pericentric distances, we find that the two streams have very different morphologies. We conclude that our model of the potential of VL-2 can provide insights about tidal streams that have not been explored by previous studies using idealized or axisymmetric models.

3.1 Motivation

The method in Chapter 2 and similar theoretical studies for stream gaps (Yoon et al., 2011; Carlberg, 2012, 2013; Erkal & Belokurov, 2015) share the same limitation—idealized dark matter halo profiles. Navarro et al. (1997, 2004, 2010) showed that dark matter halos can be described by universal profiles such as Navarro-Frenk-White and Einasto profiles, and the former is used by some simulations mentioned above because of its simple form. However, idealized profiles are spherically averaged best-fit results, which do not capture the actual shape of an individual halo. Both N-body simulations (Jing & Suto, 2002; Zemp et al., 2009) and the results inferred from observations of the Milky Way (Law et al., 2009) show that halos are not spherical. Siegal-Gaskins & Valluri (2008) simulated the disruption of a satellite galaxy and its resulting stream in a flattened potential both with and without substructures, and they found that even though substructures make the stream more clumpy, the shape of the halo has a larger effect on the satellite’s disruption than substructures have. Nevertheless, their underlying halo potential still follows an idealized profile, and their stream progenitor is much more massive than the streams we consider in our study. In this chapter, we focus on the disruption of a globular cluster in the realistic potential of a Milky-Way-sized dark matter halo in both the presence and absence of substructures, without using idealized profiles in either case. The realistic potential is constructed from the zero-redshift snapshot of the Via Lactea II (VL-2) simulation, which simulated the formation of a Milky-Way-sized dark matter halo using more than 10^9 particles (or about $4.1 \times 10^3 M_\odot$ per particle) in the Λ CDM cosmological context starting from redshift $z = 104$ (Diemand et al., 2008).

Similar to the previous chapter, the goal of this chapter is also to demonstrate the difference in the appearance of tidal streams in two cases: (1) a “smooth” dark matter halo without subhalos, and (2) a “lumpy” dark matter halo with the amount of substructures expected in a Λ CDM cosmology. Our simulation parameters are chosen so that the resulting streams would be comparable to GD-1 (Grillmair & Dionatos, 2006), but our simulations are not meant to be physical models of GD-1 because VL-2 is not a physical model of the the Milky Way, and we are only constructing a time-independent potential using one snapshot at redshift zero of VL-2. The details of orbital or stream dynamics in the VL-2 potential are beyond the scope of this study, as they are complicated topics that warrant much more focused studies in the future. This chapter is meant to present the method to construct realistic dark matter halo potentials in the presence and absence of substructures requiring neither idealized profiles nor triaxial fits. This allows us to isolate and investigate the effects that substructures have on a GD-1-like stream in a more realistic setting than in Chapter 2.

Since the tidal disruption of a star cluster is an ongoing process that lasts as long as the formation of the dark matter halo itself, a redshift-dependent potential using all available snapshots of VL-2 is our goal in the future. Bonaca et al. (2014) approached this by using a “live” halo, which essentially resimulated VL-2 but approximated the formation of streams. Another advantage of a live halo is that it can respond to an external system in order to account for effects such as dynamical friction. On the other hand, a live halo may be computationally expensive depending on its resolution. We did not use a live halo because our goal is not to rerun VL-2, but to construct a realistic model of the existing VL-2 halo at arbitrarily high accuracy and use this model as a background for our own N-body simulations. Moreover, our streams’ masses are low enough that they will not affect the evolution of the halo, and dynamical friction is negligible (Ngan & Carlberg, 2014).

This chapter is organized as follows. Section 3.2 describes the method of using the self-consistent field (SCF) method to construct the potential of VL-2, which is done after identifying the subhalo particles

using a halo finder. Section 3.3 summarizes the parameters for our simulations such as our choice of orbits. Section 3.4 is the key part of this chapter, which presents the goodness of the SCF, as well as the details of the simulated streams. Section 3.5 summarizes our results.

3.2 Method

3.2.1 SCF Method

Originally developed to compute collisionless N-body dynamics for galaxies (Hernquist & Ostriker, 1992), the SCF method solves the gravitational Poisson equation by basis decomposition. This method is optimized for dark matter halos since its lowest-order basis function is already an idealized profile, and the higher-order basis functions can be used to describe the radial and angular deviations from this idealized profile. The basis functions are bi-orthonormal and complete, so they can model any matter distribution as the decomposition order increases.

The approach to model the gravitational potentials in the snapshots of existing simulations of dark matter halos has been studied extensively by Lowing et al. (2011). Even with moderate decomposition orders, Lowing et al. (2011) was able to recover much of the detailed dynamics inside the halos of the Aquarius simulations (Springel et al., 2008). We follow their approach to compute the forces in the halo of the VL-2 simulation at redshift zero. In this section we briefly summarize the method.

The density $\rho(\mathbf{r})$ and gravitational potential $\Phi(\mathbf{r})$ are related by the Poisson equation $\nabla^2\Phi = 4\pi G\rho$. Given a simulation snapshot that contains ρ , SCF solves the Poisson equation by decomposing Φ and ρ such that

$$\Phi(\mathbf{r}) = \sum_{nlm} A_{nlm} \Phi_{nlm}(\mathbf{r}) \quad (3.1)$$

$$\rho(\mathbf{r}) = \sum_{nlm} A_{nlm} \rho_{nlm}(\mathbf{r}) \quad (3.2)$$

where $\mathbf{r} \equiv (r, \phi, \theta)$ is expressed in spherical coordinates for convenience. We follow the derivation of Hernquist & Ostriker (1992) which used the Hernquist profile (Hernquist, 1990) where

$$\Phi_{000} \equiv -\frac{1}{1+r} \quad (3.3)$$

$$\rho_{000} \equiv \frac{1}{2\pi r(1+r)^3} \quad (3.4)$$

are the zeroth-order basis functions. The general basis functions can be written as

$$\Phi_{nlm} \propto -\frac{r^l}{(1+r)^{2l+1}} C_n^{(2l+3/2)}(\xi) Y_{lm}(\theta, \phi) \quad (3.5)$$

$$\rho_{nlm} \propto \frac{r^l}{r(1+r)^{2l+3}} C_n^{(2l+3/2)}(\xi) Y_{lm}(\theta, \phi) \quad (3.6)$$

where Y_{lm} are the spherical harmonics, $C_n^{(\alpha)}(\xi)$ are the Gegenbauer polynomials, and $\xi \equiv (r-1)/(r+1)$. Taking advantage of the bi-orthonormality of the basis functions, each A_{nlm} can be computed based on

a given $\rho(\mathbf{r})$ by

$$A_{nlm} \propto \int \rho(\mathbf{r}) \Phi_{nlm}^*(\mathbf{r}) d\mathbf{r}. \quad (3.7)$$

The accelerations $-\nabla\Phi$ can be obtained by differentiating Equation (3.1) analytically.

In practice, a snapshot from an N-body simulation contains $\rho(\mathbf{r})$ which is represented by discrete particles, and the computations are much more easily done in real space. We refer the reader to Hernquist & Ostriker (1992) for a straightforward recipe to compute accelerations given a list of particle positions and masses. A noteworthy feature of the SCF method is that all accelerations are proportional to the terms

$$\sum_{k=1}^N m_k \tilde{\Phi}_{nl}(r_k) P_{lm}(\cos\theta_k) \begin{bmatrix} \cos(m\phi_k) \\ \sin(m\phi_k) \end{bmatrix} \quad (3.8)$$

where m_k and (r_k, θ_k, ϕ_k) are the mass and position of the k th particle, $\tilde{\Phi}_{nl}$ is the radial part of Equation (3.5), and P_{lm} are the Legendre polynomials. These linear summations over all N particles can be easily parallelized and precomputed given (n, l, m) . The decomposition is truncated at orders n_{max} and l_{max} (and m goes from 0 to l in real space), so both terms in Equation (3.8) are evaluated

$$\frac{n_{max}(l_{max} + 1)(l_{max} + 2)}{2} \quad (3.9)$$

times. After Equation (3.8) is precomputed, the accelerations can be obtained analytically.

A detailed strategy to parallelize the SCF method has been proposed by Hernquist et al. (1995) to compute N-body dynamics using the SCF method itself. Note that our problem is even simpler because we are only extracting the accelerations from an existing N-body snapshot, and the accelerations do not need to be propagated back to the bodies. The extracted accelerations serve as “external forces” for each particle of our stream simulations.

SCF offers a convenient way to account for redshift dependence. Since the model of one static potential is entirely represented by the set of coefficients A_{nlm} in Equation (3.1), these coefficients can simply be interpolated in redshift. Lowing et al. (2011) showed that the time variation of the first few coefficients at the lowest orders are relatively small, but higher-order variations may be more difficult to capture. However, this is unlikely to be a problem for us because we account for subhalos separately from the smooth halo. We defer the construction of a redshift-dependent potential to future studies.

3.2.2 Subhalo Finding

We use the AMIGA HALO FINDER¹ (AHF) to identify bound structures in the high-resolution region of VL-2. The most massive halo, hereafter the “main halo,” is the halo that hosts the subhalos and the tidal streams of interest in this study. Many particles in the main halo are also bound into additional levels of substructures. In the first level there are 11,523 “subhalos” that consist of at least 150 particles. The minimum halo mass threshold is chosen such that the average peak circular velocity for those halos ($V_{max} \sim 2.5 \text{ km s}^{-1}$) approximately corresponds to the peak circular velocity below which the subhalo abundance is suppressed by numerical limitations (Diemand et al., 2008; Diemand & Moore, 2011). This threshold choice allows for a robust sampling of the subhalo mass function.

In addition to each subhalo’s particle membership, AHF also automatically computes their intrinsic properties such as positions of the minimum potential, bulk velocities, scale radii, virial radii, etc. Note

¹<http://popia.ft.uam.es/AHF/Download.html>

Halo	N	$M (M_{\odot})$	r_s (kpc)	r_{vir} (kpc)
Main halo	4.46×10^8	1.89×10^{12}	60.4	400
Most massive subhalo	1.15×10^6	4.69×10^9	6.43	54.2
Least massive subhalo	150	6.15×10^5	0.411	2.75

Table 3.1: Main Halo and Subhalos in the $z = 0$ Snapshot of VL-2. The total number of particles (N), total masses (M), scale radii (r_s), and virial radii (r_{vir}) of three nominal halos extracted by the halo finder, which found a total of 11,523 subhalos inside the virial radius of the main halo.

that the virial radius, which is essentially the boundary of each subhalo, is defined by a rise in the radial profile, as opposed to an overdensity threshold for the main halo (Knollmann & Knebe, 2009). Table 3.1 summarizes the facts about our main halo, as well as the most and least massive subhalos. Note that the total number of particles and total mass of the main halo include all the particles of the subhalos, as returned by AHF. As we discuss in the following section, we remove the subhalo particles from the main halo, so the mass of the main halo in our simulations is slightly lower than the value stated in Table 3.1.

3.2.3 Modeling the smooth halo

In order to obtain a smooth halo from VL-2 that is a Λ CDM simulation, we remove all the subhalo particles from the main halo, leaving “voids” that were previously occupied by subhalos. When we construct the smooth halo’s potential, we use a low-order decomposition that only captures the overall shape of the main halo, but not the lumpiness due to the removed subhalos.

For convenience, for the smooth halo we only consider the cases where $n_{max} = l_{max}$, which we will refer to as the decomposition “order” collectively. Figures 3.2 and 3.3 show the accuracies of constructing the force field of the smooth halo using orders 10 and 20 by comparing against the force field that is obtained by directly summing up the force contributions from all the particles in the smooth halo. The force fields using both SCF and direct summation are computed in 94,747 randomly distributed positions inside a spherical shell of $r = [15, 40]$ kpc in thickness where our stream will be orbiting.

There are 660 and 4620 terms in the decompositions using orders 10 and 20, respectively (Equation 3.9). Figure 3.4 shows that the improvements in accuracy by increasing the order from 10 to 20 are marginal. For the purpose of this study, it is not necessary to model VL-2 with the highest possible accuracy. Our goal is to study the effects that a dark matter halo has on tidal streams in general, but not to model any particular objects that have been observed.

One alternative way to construct a smooth halo is to perform a decomposition with similar orders on all the main halo particles without removing the subhalo particles. We ran a similar analysis to Figures 3.2 and 3.3 using all particles, and we found that compared to having removed the subhalo particles, using all particles gave similar error levels except at positions near the subhalos, where the errors would typically be a few percent higher. This was expected because decompositions at orders 10 or 20 cannot model the forces inside the subhalos that were contributing to the directly summed forces. Removing the subhalo particles allowed us to confirm that our force errors were within 1% inside the smooth halo alone.

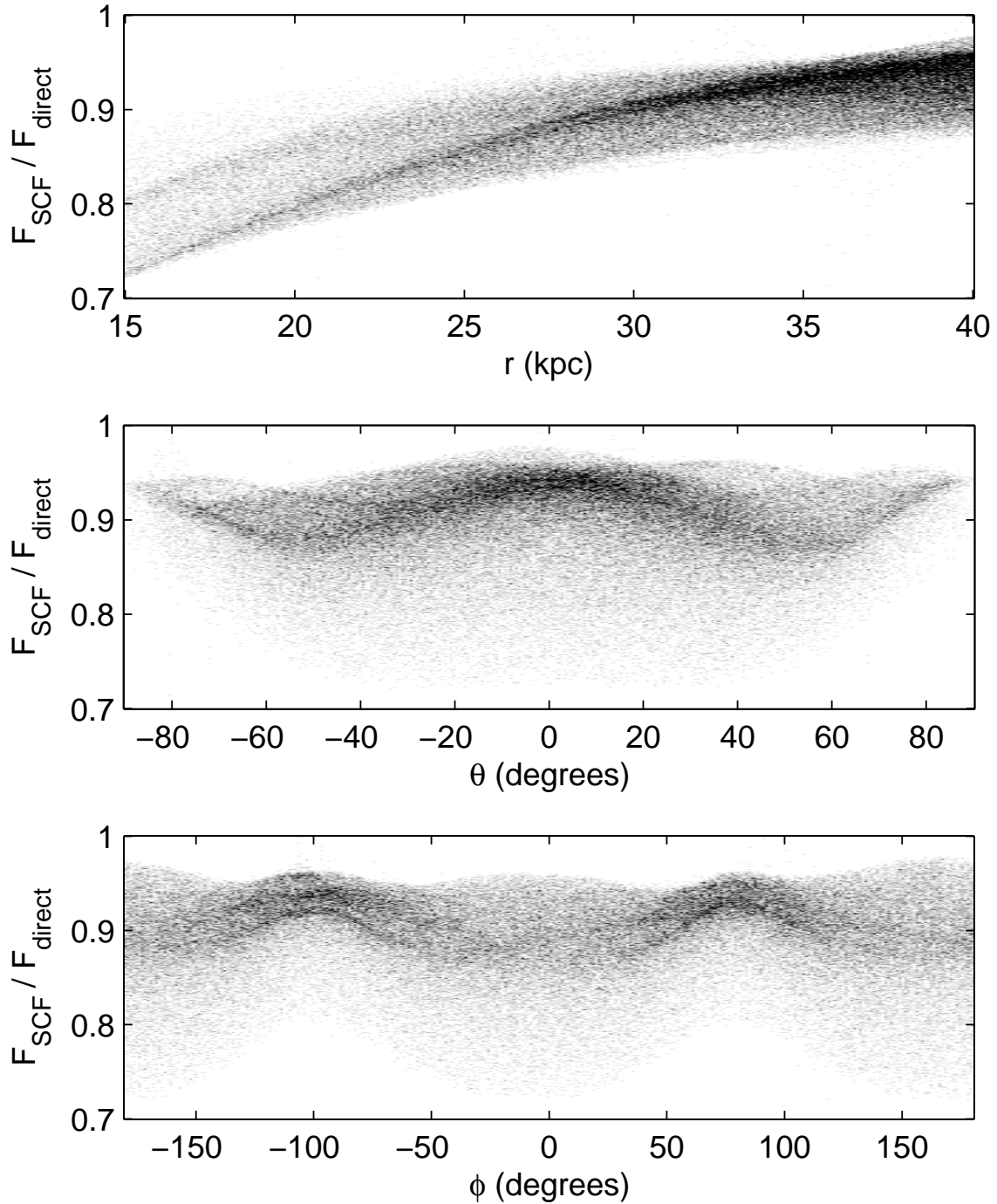


Figure 3.1: Comparing the magnitude of accelerations obtained from SCF ($n_{max} = l_{max} = 0$) against directly summing up the accelerations from all particles in the smooth halo. The accelerations are measured at 94,797 randomly distributed positions inside a spherical shell of $r = [15, 40]$ kpc. Top, middle, and bottom panels are the errors plotted against the (r, θ, ϕ) in spherical coordinates of the test positions.

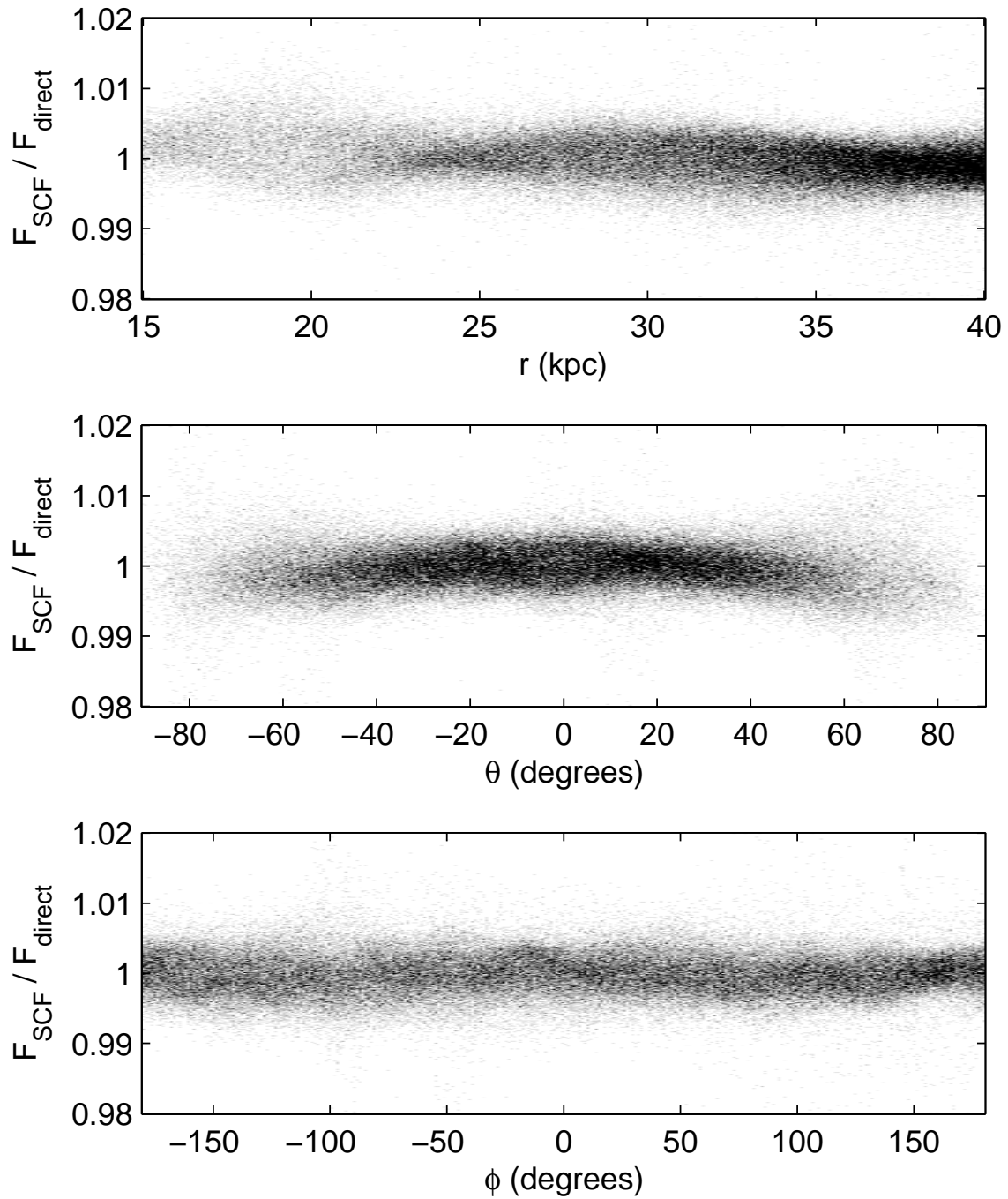


Figure 3.2: Same as Figure 3.1, but with $n_{\text{max}} = l_{\text{max}} = 10$. The accelerations are accurate to $\sim 1\%$ level everywhere. Note the change in vertical scale from Figure 3.1.

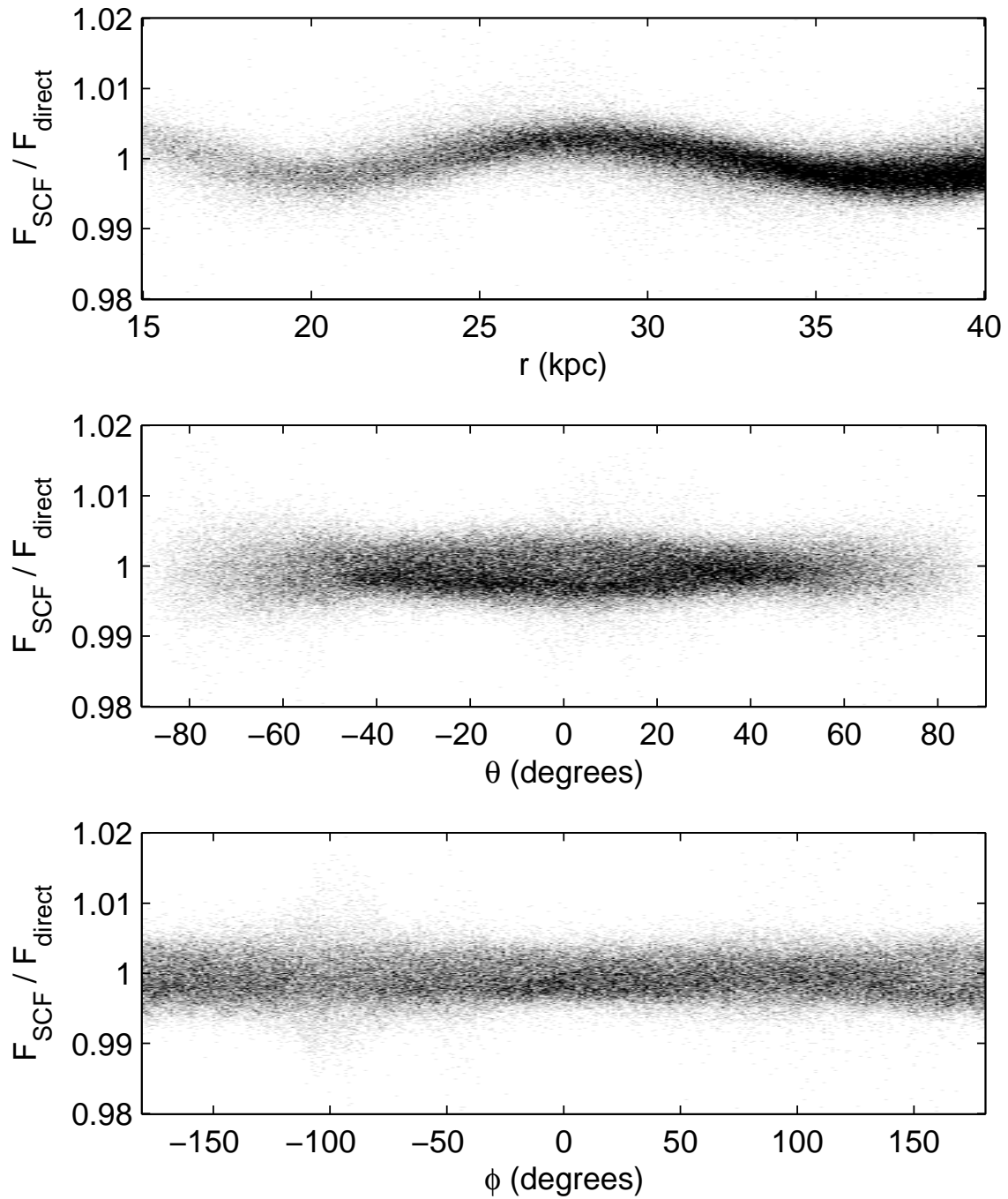


Figure 3.3: Same as Figure 3.2, but with $n_{max} = l_{max} = 20$. The top panel shows some correlation between the force error and radial position. This correlation is expected from basis functions whose radial components are polynomials. Nevertheless, the errors remain at the 1% level, so the correlation is not a concern.

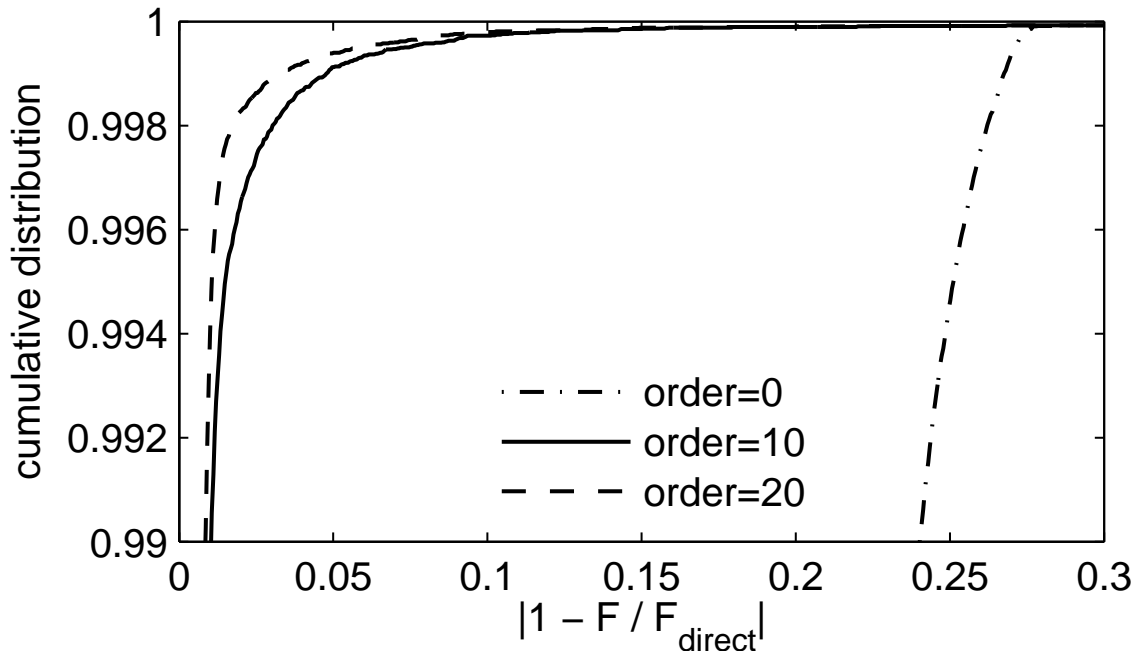


Figure 3.4: The cumulative distribution of the error at all the points in Figures 3.1–3.3. The $\sim 1\%$ level error is achieved more than 99% of the time for orders 10 and 20, but the errors for order 0 are much larger.

3.2.4 Adding Subhalos

For the lumpy halo, we now add the forces by the subhalos back into the smooth halo. We decompose each subhalo using $n_{max} = 4, l_{max} = 0$. In addition to being simpler to compute, we prefer not to decompose subhalos at higher orders because some low-mass subhalos can have only a few hundred particles, so a low n_{max} and spherically symmetric decomposition can avoid unphysical clumpiness in each subhalo. Also, subhalos’ effects on tidal streams are expected to be of short duration, so it is not necessary to model individual subhalos in detail.

Adding subhalos separately to the smooth halo provides two advantages. First, we can control the mass range of subhalos that are present in the galaxy. This can be used to test theories such as warm dark matter that suppress the formation of low-mass subhalos. Second, each individual subhalo can orbit freely around the smooth halo, so their encounters with tidal streams can be modeled realistically.

The separate subhalos introduce extra mass to the smooth halo when comparing lumpy and smooth halos. Our full range of subhalos have masses $1.067 \times 10^{11} M_{\odot}$ in total, which is about 6% of the mass of the smooth halo. In our simulations, we only use a subset of subhalos that (a) have pericentric distances of less than 40 kpc and (b) are less massive than $10^8 M_{\odot}$. The reason for requirement (a) is that subhalos that do not approach the stream will have minimal effects on our streams with apocentric distances at 30 kpc in their orbits. The reason for requirement (b) is that encounters with massive subhalos do not leave interesting signatures. As shown in Yoon et al. (2011), massive subhalos are rarer than low-mass subhalos, so massive subhalos mostly influence a stream by distant encounters that do not cause gaps in the stream. On the other hand, when a massive subhalo makes a close encounter with a stream, the effect

is likely catastrophic to the stream as opposed to leaving small gaps that have been observed (Carlberg et al., 2012; Carlberg & Grillmair, 2013). A separate study for the effects of massive subhalos on streams in a realistic potential is presented in Chapter 4. For this study, after imposing requirements (a) and (b), the lumpy halo has 3808 subhalos in our simulations, which have a total mass of $1.607 \times 10^{10} M_{\odot}$, or about 1% of the mass of the smooth halo. Therefore, the streams simulated with and without subhalos will only have slightly different orbits, and the difference can be safely ignored for our comparisons.

3.3 Stream simulations

3.3.1 Progenitor and Orbit

The streams’ progenitor is a star cluster following a King profile with core size 0.01 kpc and $w = 4.91$, where w can be thought of as the ratio between the depth of the potential and central velocity dispersion of the cluster. Its total mass is $4.29 \times 10^4 M_{\odot}$, central velocity dispersion is 2.4 km s^{-1} , and tidal radius is 0.103 kpc (identical to the one used in Ngan & Carlberg (2014)). We use $N = 1,000,000$ particles for the the main results of this study. Furthermore, as argued in Ngan & Carlberg (2014), the number of particles in the stream may be higher than the number of stars in the observed streams. Whether the effects we present in the following sections can be found in existing data requires more careful investigation, which is beyond the scope of this study.

We simulate the star cluster with two orbits shown in Figure 3.5—both start at $(x, y, z) = (30, 0, 0)$ kpc, but one orbit with $(v_x, v_y, v_z) = (0, 120, 0) \text{ km s}^{-1}$ (“Orbit 1”), and the other with $(0, 41.0, 113) \text{ km s}^{-1}$ (“Orbit 2”), which is the former with an initial velocity inclined at 70° from the xy -plane. The VL-2 main halo has not been aligned with any axis, so the directions of the initial velocities are arbitrarily chosen to explore the main halo as much as possible. Although neither orbit is confined in any orbital planes, both are tube orbits with apo- and pericentric distances at roughly ~ 30 kpc and ~ 17 kpc, which are chosen to be similar to the inferred values of the GD-1 stream (Grillmair & Dionatos, 2006; Willett et al., 2009).

3.3.2 Simulation Details

The SCF decomposition is performed using the procedure exactly described in Hernquist & Ostriker (1992). Since we consider decomposition orders that are much lower than the number of particles in VL-2, it is not necessary to apply a smoothing kernel to the VL-2 particles when computing the decomposition coefficients because a low-order decomposition, by construction, cannot capture the granularity of the VL-2 particles.

Our N-body simulations of streams are computed using GADGET-2 (Springel, 2005), which is available to the public². We modify GADGET-2 so it uses the precomputed SCF decomposition coefficients to construct the external accelerations, which are added to the particles in our stream simulations after the stream particles’ N-body forces have been computed. We impose a maximum time step of 1 Myr and softening of 5 pc for the particles so that they are essentially collisionless.

²<http://www.mpa-garching.mpg.de/gadget/>

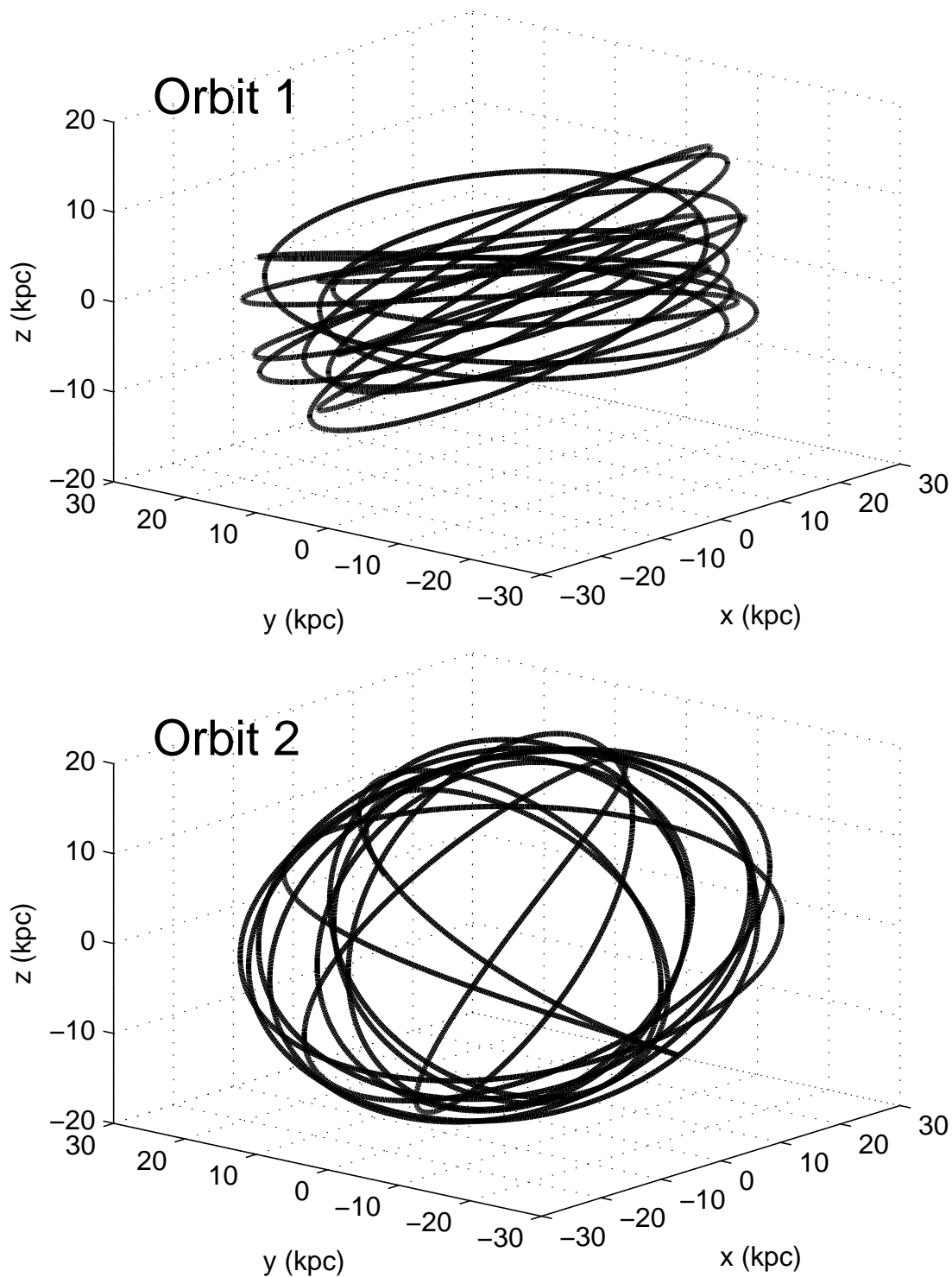


Figure 3.5: Two stream orbits in an SCF potential of the smooth halo using order 10 with initial positions at $(x, y, z) = (30, 0, 0)$ kpc, but with $(v_x, v_y, v_z) = (0, 120, 0)$ km s^{-1} (“Orbit 1”; top panel) and $(0, 41.0, 113)$ km s^{-1} (“Orbit 2”; bottom panel). Both are tube orbits with apo- and pericenters that roughly correspond to the inferred values of GD-1.

3.4 Results and Discussion

3.4.1 Decomposition Order

Orbital Convergence

The basis functions in the SCF method are complete, which means that the higher the decomposition order, the more accurate the constructed model will be. It is crucial to understand the decomposition order necessary for our purposes. Neither VL-2 nor our stream simulations are meant to be physical models of any observations, so it is not necessary for us to model the VL-2 main halo to the highest possible accuracy with a high decomposition order. In fact, since we have removed subhalos from the main halo, modeling these “voids” in the smooth halo may result in spurious forces. On the other hand, if the decomposition order is too low, then it compromises the value of using VL-2, which features shapes and profiles missing in idealized profiles. We require a decomposition order that is high enough to capture the shape and profile of the VL-2 smooth halo, but not high enough to capture the granularity of its substructures (the contribution by substructures will be added in after the smooth halo has been modeled).

The radial coordinates of the two progenitor orbits as functions of time for various decomposition orders are shown in Figure 3.6. Both orbits have converged to within a few percent everywhere for 10 Gyr. This is expected from Figures 3.2 and 3.3, which show that the forces almost everywhere are accurate to $\sim 1\%$ even at only order 10. Therefore, a decomposition order 10 is sufficient for our purposes. Using order 10 has the advantage that subhalo “voids” will not be captured. There are more than 10,000 subhalos found within the virial radius of the main halo, and the granularities of these subhalos cannot be modeled by polynomials of only the 10th degree in either the radial or angular components of SCF basis functions.

Lowing et al. (2011) showed that decompositions lower than order 10 give significant errors in the region less than a few kiloparsecs away from the halo’s center, so Lowing et al. (2011) adapted order 20 to suppress those errors. That region is not relevant for our streams because they orbit at galactocentric distances well beyond a few kiloparsecs. Nevertheless, our convergence results agree with Lowing et al. (2011), which showed that the acceleration errors compared to direct summation are at $\sim 1\%$ beyond 17 kpc, and that increasing from order 9 to 19 provides minimal gain in those regions.

Stream Density Convergence

As shown in Ngan & Carlberg (2014), signatures of subhalos can be detected in the linear density, or number of particles per unit length, along the stream. Even though the previous sections show that the accelerations and orbits have converged to within a few percent, we now investigate how well the stream density converges.

Figure 3.7 shows the linear density along four streams using 100,000 particles each and traced along a sky projection as seen by an observer at the galactic center (so the unit along the length of stream is angular) at 6.7 Gyr. The four streams started with identical progenitors in Orbit 1, but in the smooth halos that are constructed using orders 10, 15, 20, and 25. Although the overall profiles of the streams’ densities on large scales are similar among the four orders, the detailed fluctuations are quite different. To investigate the significance of these differences, we simulated a few additional streams with different random realizations of the progenitor, but with the same number of particles, physical parameters, and

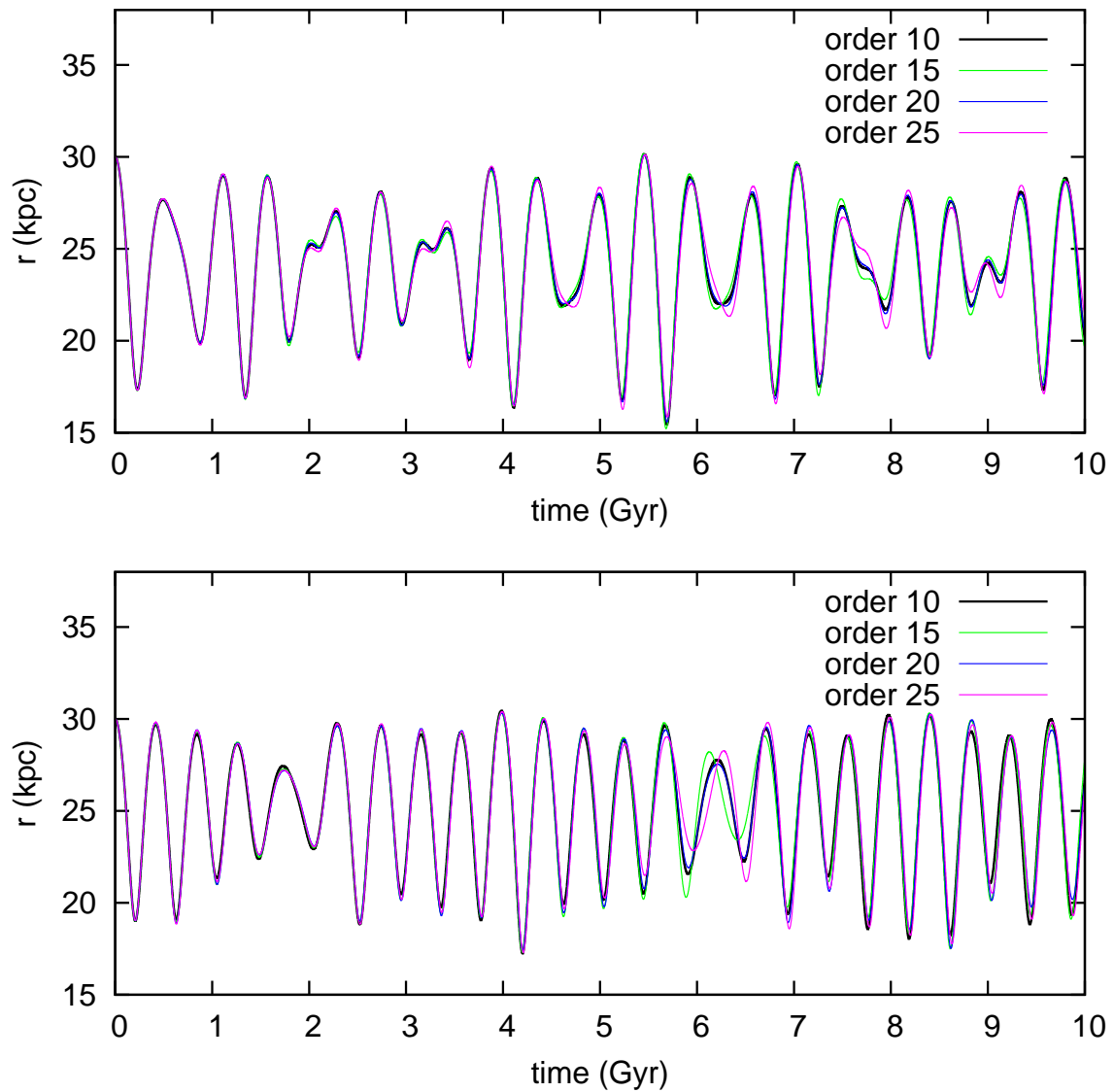


Figure 3.6: Radial coordinates of two progenitor orbits shown in Figure 3.5. Top and bottom panels show Orbits 1 and 2, respectively. These two plots show that their orbits have converged at order 10.

orbit, in the same smooth halo potential using order 10. We find that the small-scale differences between these additional streams are indistinguishable from the differences between the four panels in Figure 3.7. Therefore, the differences shown in the figure are simply due to stochastic noise of the particles, and our decomposition has sufficiently converged at order 10.

The convergence of our decomposition can also be seen in Figure 3.8, which shows the mass loss for each stream in Figure 3.7. Every large spike, or major mass loss event, in each stream is associated with a pericentric passage shown in the top panel of Figure 3.6. However, the minor mass-loss events do not occur at the same rate among the four orders. Our additional streams with different progenitor realizations as explained above show, again, that the small-scale differences for each decomposition order shown in Figure 3.8 are indistinguishable from stochastic noise.

We adapt order 10 for the smooth halo for the rest of our results. As we show in the next sections, gaps caused by subhalos are longer than the spurious gaps caused by changing the decomposition order as shown in Figure 3.7. This is similar to the result of Ngan & Carlberg (2014), where the gap size distribution can be used to distinguish “intrinsic” gaps from subhalo gaps. In the future, we aim to repeat similar analyses to Ngan & Carlberg (2014) using various SCF decomposition orders for the realistic halo.

3.4.2 Densities along the Streams

Stream 1 in the Smooth Halo

We first examine the intrinsic features in the stream in Orbit 1 (hereafter “Stream 1”) in the smooth halo without any subhalos. Figure 3.9 shows the surface density of the stream projected on the sky from 8 to 8.5 Gyr as seen by an observer situated at the galactic center, and Figure 3.10 shows the linear density along the stream at the same times. This time frame roughly corresponds to one radial oscillation (though it is not a “radial period”; see Figure 3.6), so it allows us to investigate the streams’ features as the streams stretch and compress during that oscillation.

The resulting stream is long and narrow, with a length-to-width ratio of about 50 (which is slightly lower than the observed values in GD-1 (Grillmair & Dionatos, 2006)), so it can simply be represented by its linear density. The most prominent feature in the linear density is the spikes located within 10° away from either side of the progenitor. Upon inspection, we find that new spikes develop immediately after pericentric passages, and each spike originates from the progenitor and migrates toward the ends of the stream. One possible cause of the density spikes is EOs, which are caused by the “piling up” of particles in their epicyclic orbits as they escape from the progenitor. In the original derivations in Küpper et al. (2008, 2010), the spacings between the EOs are calculated assuming an axisymmetric potential. Although the VL-2 halo has no spatial symmetry, we can approximate it by spherically averaging our potential model (ie. taking $l_{max} = 0$ in Equation (3.1)). Using a representative value of R for the angular frequency Ω and epicyclic frequency κ , we can estimate the spacing

$$|y_C| = \frac{4\pi\Omega}{\kappa} \left(1 - \frac{4\Omega^2}{\kappa^2} \right) x_L, \quad (3.10)$$

where $x_L = GM/(4\Omega^2 - \kappa^2)$, between the first EOs on either branch of the stream (Küpper et al., 2008). For $R = 24$ kpc (roughly the galactocentric radius of the progenitor at 8.3 Gyr), we obtain $\Omega \simeq 8 \text{ Gyr}^{-1}$ and $\kappa \simeq 12 \text{ Gyr}^{-1}$. This gives $|y_C| \simeq 0.77$ kpc, or 1.8° when projected onto the sky, which is almost a

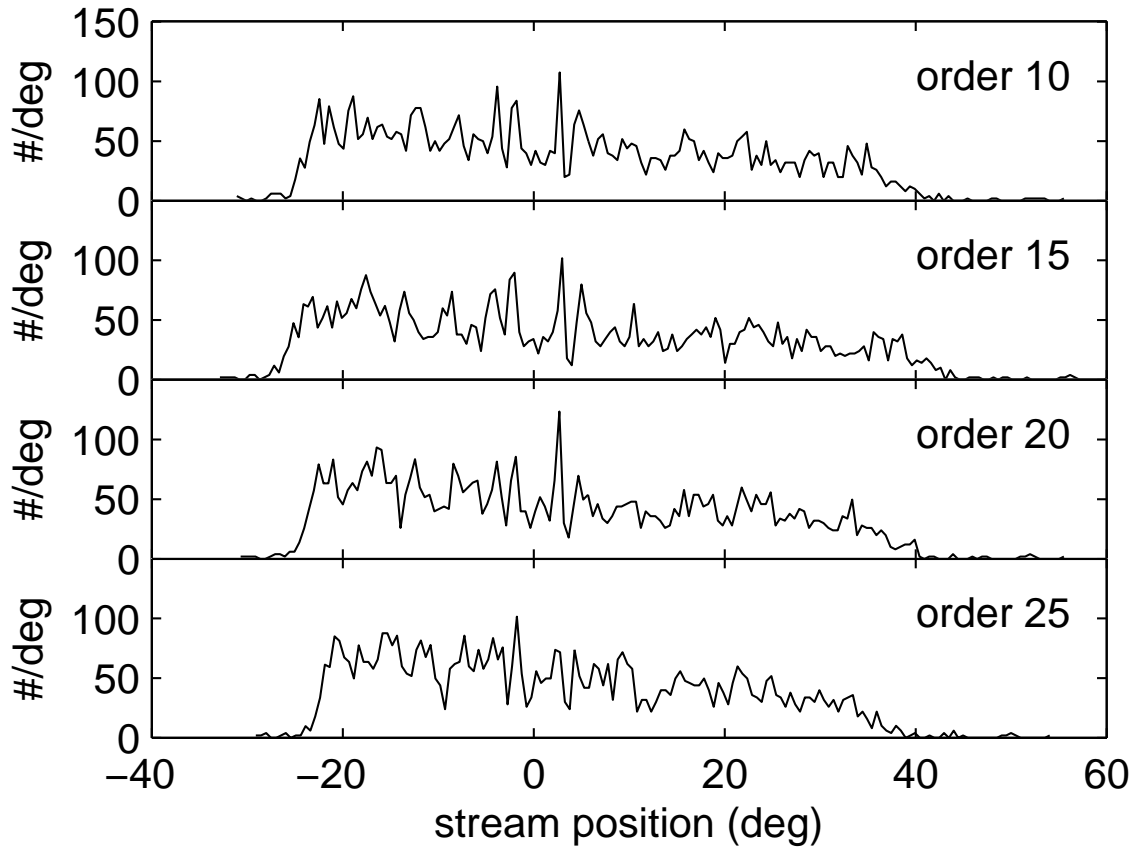


Figure 3.7: Four streams that start with the same initial conditions with Orbit 1 in the smooth halo that is constructed using different decomposition orders. The streams' overall profiles on large scales are similar, but the density fluctuations on small scales are different.

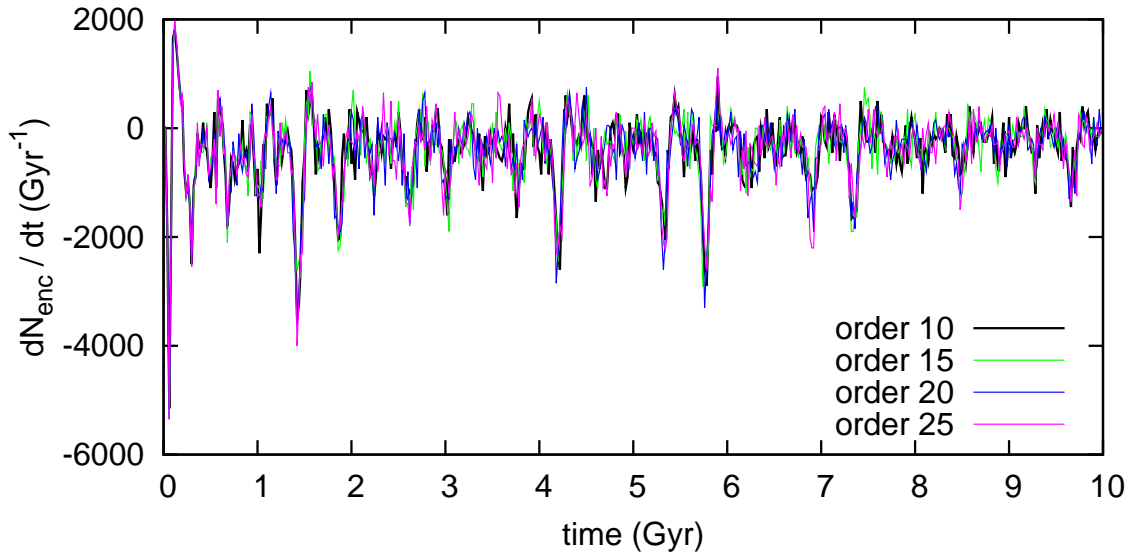


Figure 3.8: Rate of change in the number of particles enclosed in 0.1 kpc from the center of the progenitor as a function of time in Orbit 1. Every spike in mass loss is associated with a pericentric passage. Even though the major mass loss events occur at the same time at the same rate among all orders, the minor events do not.

factor of 2 smaller than the measured spacing at $\sim 3^\circ$ between the first two density spikes at 8.3 Gyr. Note that as the stream compresses and stretches as it oscillates radially, the spacing between the spikes can easily differ by factors of a few (eg. compare 8.2 and 8.4 Gyr in Figure 3.10).

The density profiles along the stream shown in Figure 3.10 indicate that the density spikes near the progenitor are very prominent inside the VL-2 potential and are similar to those in Ngan & Carlberg (2014) in a spherical potential—they are regularly spaced and appear very close to the progenitor. As we shall see in the next sections, gaps caused by subhalos are randomly spaced and can occur anywhere along the stream.

Stream 1 in the Lumpy Halo

Figures 3.11 and 3.12 show the sky projection and linear density of Stream 1 in a lumpy halo with 3807 subhalos. Compared to the same stream in the smooth halo, the density clearly shows gaps as local minima that are more pronounced and occur everywhere along the stream. The density spikes near the progenitor are still present with similar spacing to the stream in the smooth halo. This is not surprising, since the extra subhalos contribute only $\sim 1\%$ of the total mass of the smooth halo, so any effects due to the stream’s orbit would not be different from the smooth halo case.

Recall from Section 3.2.4 that our simulations in the lumpy halo contains 3808 subhalos. An interesting but rare event that occurred in the simulation with 3808 subhalos was that the progenitor had a close encounter at less than one half-mass radius from a $1.8 \times 10^7 M_\odot$ subhalo at an early time, which caused a sudden burst in mass loss for the progenitor. This resulted in a stream that was dominated by two large but smooth spikes, one in each branch of the stream. When this subhalo was eliminated, we were able to resolve the density fluctuations caused by close encounters between the tidal tails and

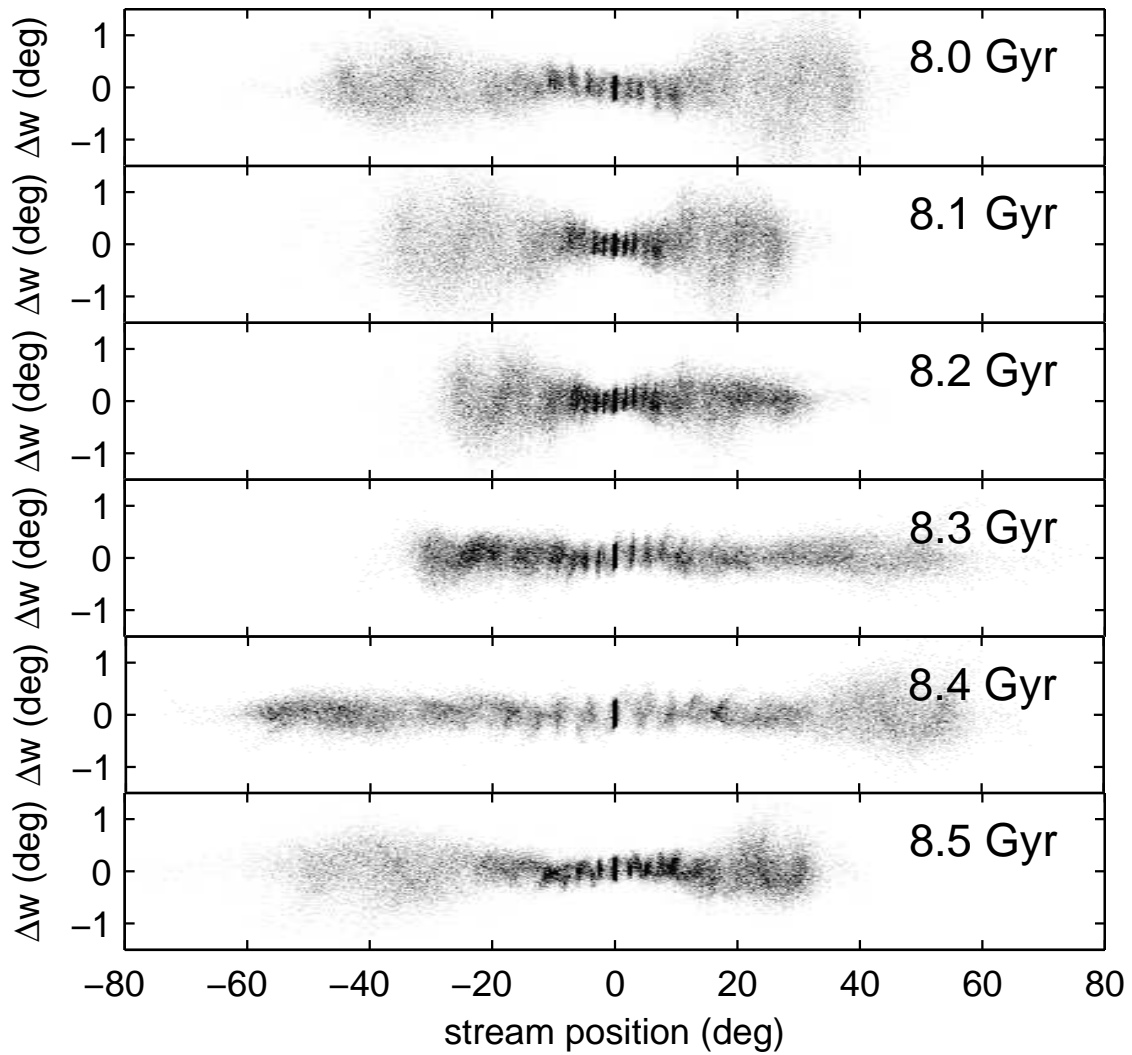


Figure 3.9: Sky-projected surface density of the stream in Orbit 1 in the smooth halo. The projection is seen from a hypothetical observer situated in the galactic center. Since the stream is extremely narrow compared to the size of its orbit, the curvature of the stream on the sky has been subtracted, and the progenitor has been shifted to have position at 0° . Note that the width of the stream (Δw on the y-axis) is about 50 times smaller than the length of the stream.

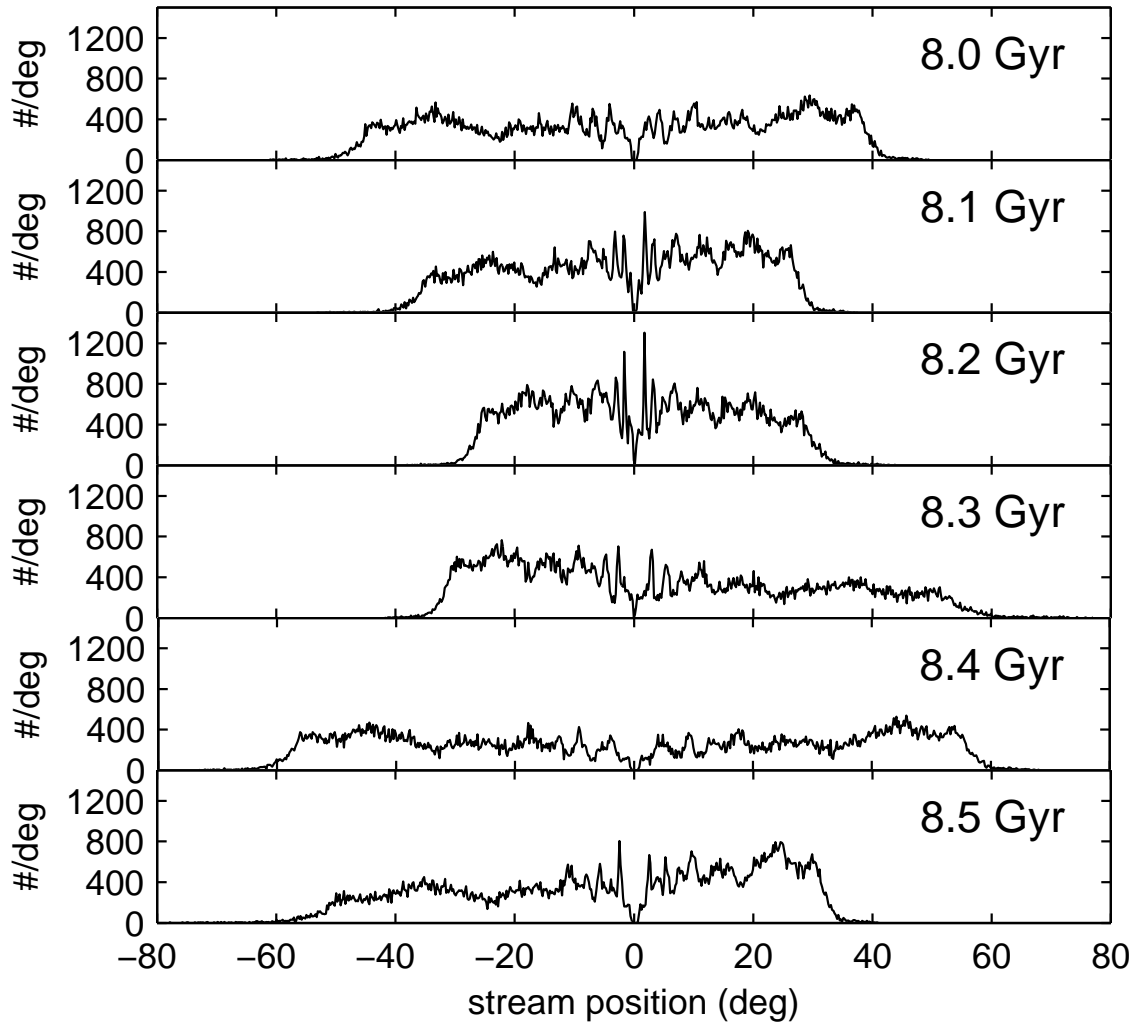


Figure 3.10: Linear density corresponding to the same stream shown in Figure 3.9. The progenitor at position 0° has been masked out. Epicyclic overdensities appear as the first few spikes within about 10° on either side of the progenitor (especially noticeable at 8.2 Gyr when the stream is compressed).

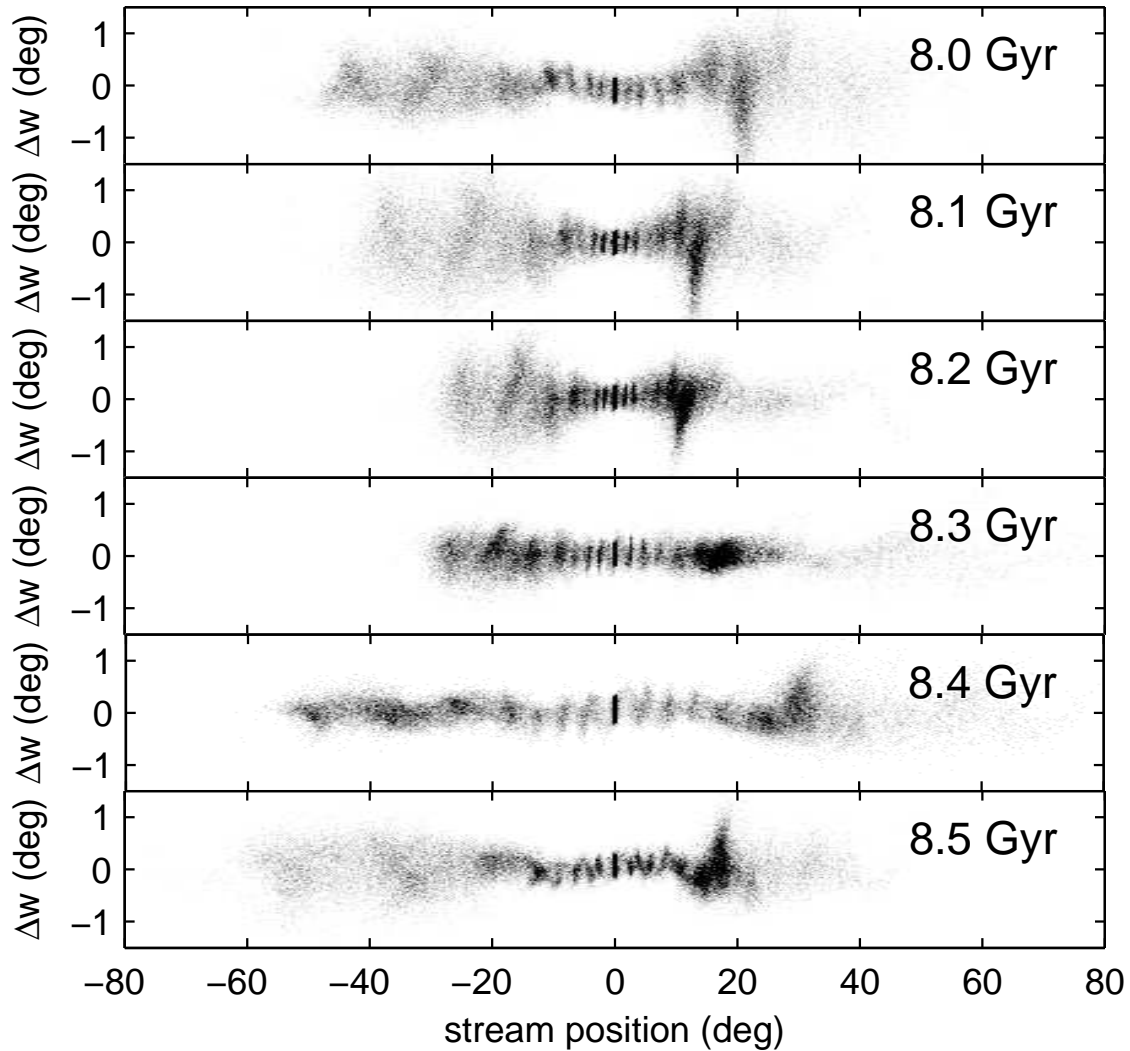


Figure 3.11: Same as Figure 3.9, but in a lumpy halo with 3807 subhalos.

subhalos as shown in Figures 3.11 and 3.12, rather than between the progenitor and subhalos. Chapter 4 illustrates the more pronounced effects that massive subhalos have on streams beyond density gaps.

Stream 2 in the Smooth Halo

Figure 3.13 shows the sky-projected density of the stream in Orbit 2 (hereafter “Stream 2”) from 6.0 to 6.7 Gyr in the smooth halo. Similar to our investigation for Stream 1, this time frame also covers roughly one radial oscillation even though a well-defined radial period does not exist in the VL-2 potential (Figure 3.6). Compared to Stream 1, Stream 2 becomes “fluffy” at the far ends of its tidal tails, with widths sometimes comparable to the length of the narrow part of the stream. This is very different from Stream 1 shown in Figure 3.9, which has a high length-to-width ratio throughout.

An important implication is that only the narrow segment of the stream may be dense enough to be observable, and the rest of the stream may be too diffuse. Simulations in Pearson et al. (2015) in triaxial potentials also showed similarly diffuse features dubbed “stream-fanning” in the tips of tidal tails, which

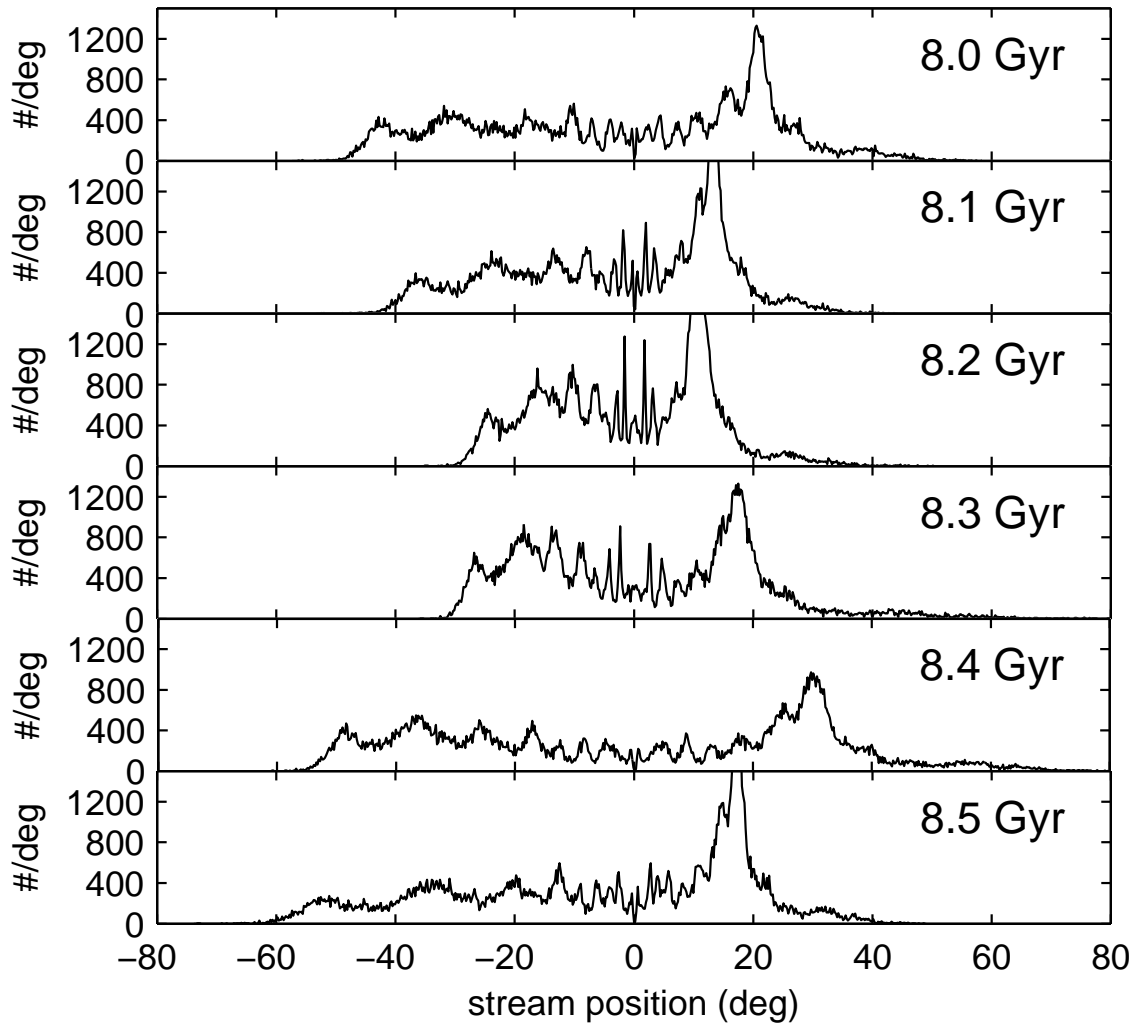


Figure 3.12: Linear density corresponding to the same stream shown in Figure 3.11. Compared to the smooth halo case (Figure 3.10), in a lumpy halo the stream appears clumpier with more local minima in density everywhere in the tails of the stream.

are not found in observations. Price-Whelan et al. (2015) argued that the physical origin of stream-fanning is the chaotic evolution of the frequencies of the stream particles’ orbits. Frequency analysis of orbits in the VL-2 potential warrants a separate study, and is beyond the scope of this chapter. It is not yet clear whether our Stream 2 is exhibiting stream-fanning.

Because of the diffuse tails, it is no longer appropriate to analyze the entire stream simply by the linear density. Nevertheless, we can trace the linear density along the narrow part of the stream out to about 10° – 20° away from the progenitor. Figure 3.14 shows the densities along the stream at each time shown in Figure 3.13. The density profiles show prominent density spikes next to the progenitor, and the spacings between those spikes are in rough agreement with the derivation in Section 3.4.2. Other than this, the density profiles fall off very quickly and smoothly toward the diffuse ends of the stream.

Stream 2 in the Lumpy Halo

Figure 3.15 shows the sky-projected density of Stream 2 from 6.0 to 6.7 Gyr in a lumpy halo with 3808 subhalos. The stream resembles the case in the smooth halo (Figure 3.13) with very fluffy ends, but in a lumpy halo they are even more prominent. In the fluffy regions the width can exceed the length of the narrow regions, which span only 10° – 20° .

The linear density along the stream can be plotted, but similar to the case in the smooth halo, it is only appropriate to the narrow regions near the progenitor. As seen in Figure 3.16, the density profiles in those regions are also smooth with the exception of the first or second density spikes. Therefore, for this stream, there are no distinguishable signatures in the linear density that traces the existence of subhalos.

Perhaps a more interesting aspect of this stream is the tips of its tidal tails. The wide and diffuse tails shown in Figure 3.15 are reminiscent of “shell”-like features found in satellite systems that plunge near the galactic center on very eccentric orbits. With apo- and pericentric distances at $r_a \simeq 30$ kpc and $r_p \simeq 17$ kpc, respectively, the stream’s eccentricity is $e = (r_a - r_p)/(r_a + r_p) \simeq 0.3$. This implies that satellites do not need to be on eccentric orbits to have significant parts of their tidal tails disrupted such that their surface brightnesses may be even lower than that of the narrow stream itself, which is already difficult to observe. In Ngan & Carlberg (2014), the same progenitor orbiting a spherical and idealized halo with similar eccentricity to Streams 1 and 2 here would be identical, and both would be very narrow streams. This indicates that using a realistic halo is important when studying the effects that subhalos have on GD-1-like streams. In Chapter 4, we simulate the tidal disruptions of globular-cluster type satellites in many orbits in both the smooth and lumpy halos in order to study the survival rate of tidal tails.

3.5 Chapter Summary

We constructed potential models using the high-resolution dark matter halo in the $z = 0$ snapshot of the Via Lactea II (VL-2) simulation. In the high-resolution “main” halo, we used a halo finder to remove and isolate subhalo particles. The potentials of the main halo and the subhalos were then constructed individually. This allowed us to simulate tidal streams in the main halo with and without subhalos. We investigated the difference in the stream between the two cases and showed that, even in a realistic potential without using idealized profiles, streams remain a valuable probe to detect subhalos whose existence is a crucial prediction of the Λ CDM model.

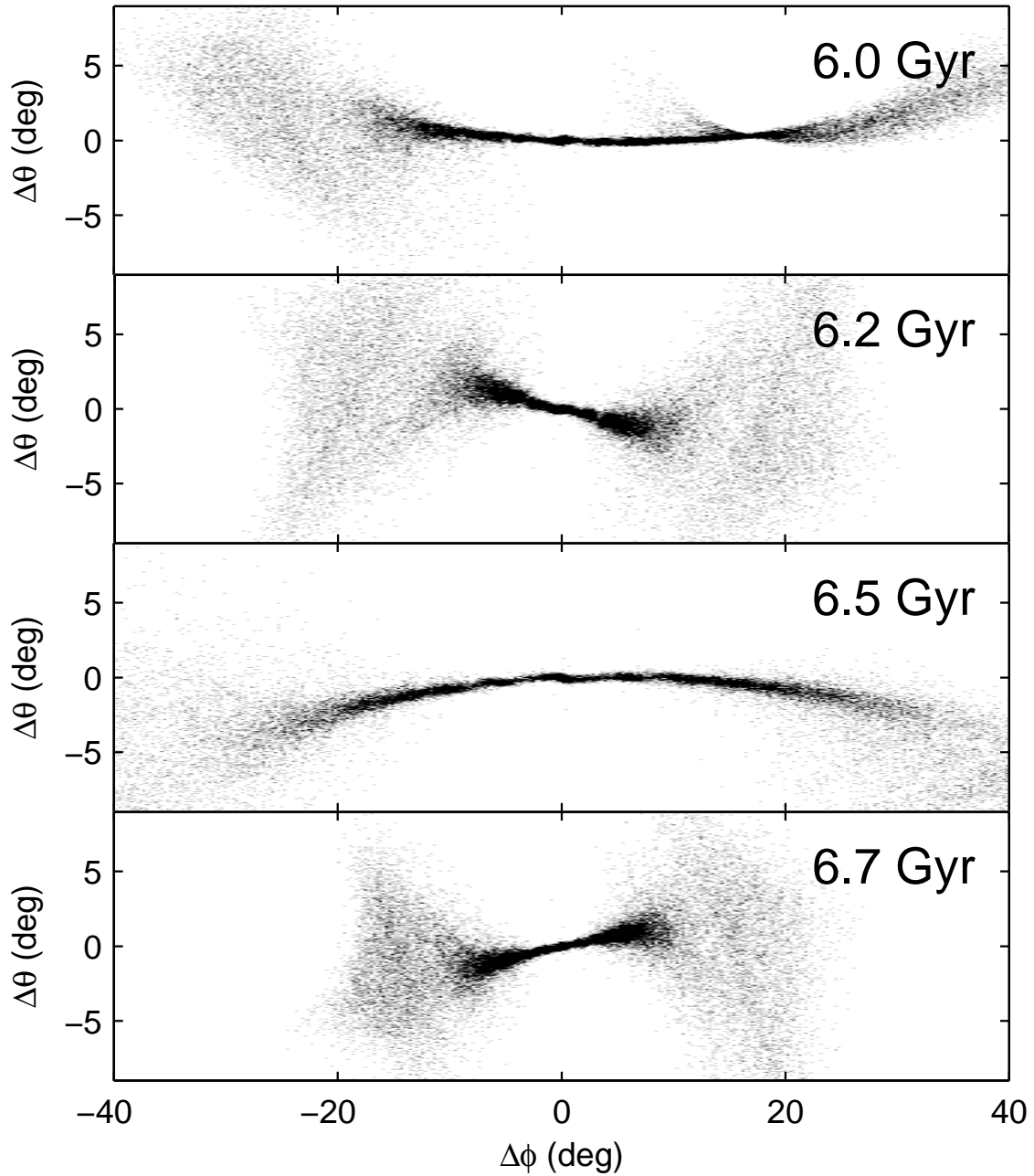


Figure 3.13: Sky-projected surface density of Stream 2 in the smooth halo. The projection is seen from a hypothetical observer situated in the galactic center. Compared to Figure 3.9, the streams here contain diffuse ends sometimes as wide as the length of the stream. Rather than tracing a line and subtracting their curvatures on the sky, the streams shown here are simply shifted so that the progenitors have $\phi = \theta = 0$, and then rotated so they appear roughly horizontal.

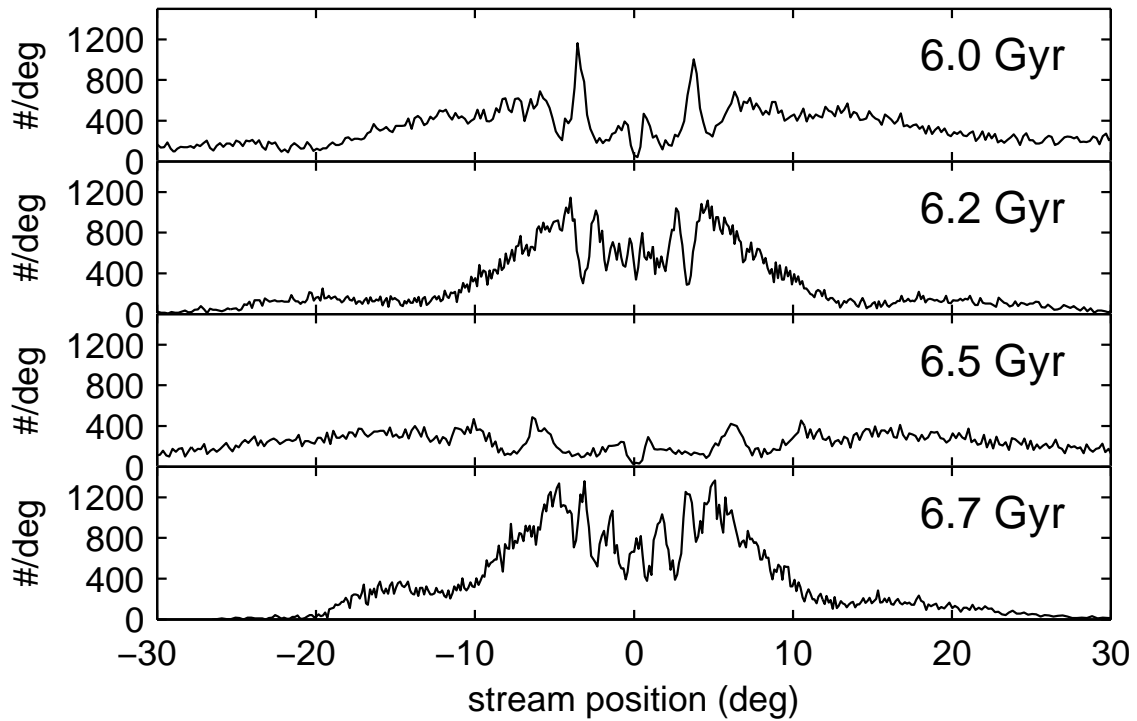


Figure 3.14: Linear density corresponding to the same stream shown in Figure 3.13. A line has only been traced along the regions up to 20° away from the progenitor. The progenitor at position 0° has been masked out. The density profiles show prominent density spikes near the progenitor, similar to Stream 1, but the profiles quickly fall off to the diffuse regions without many intrinsic features.

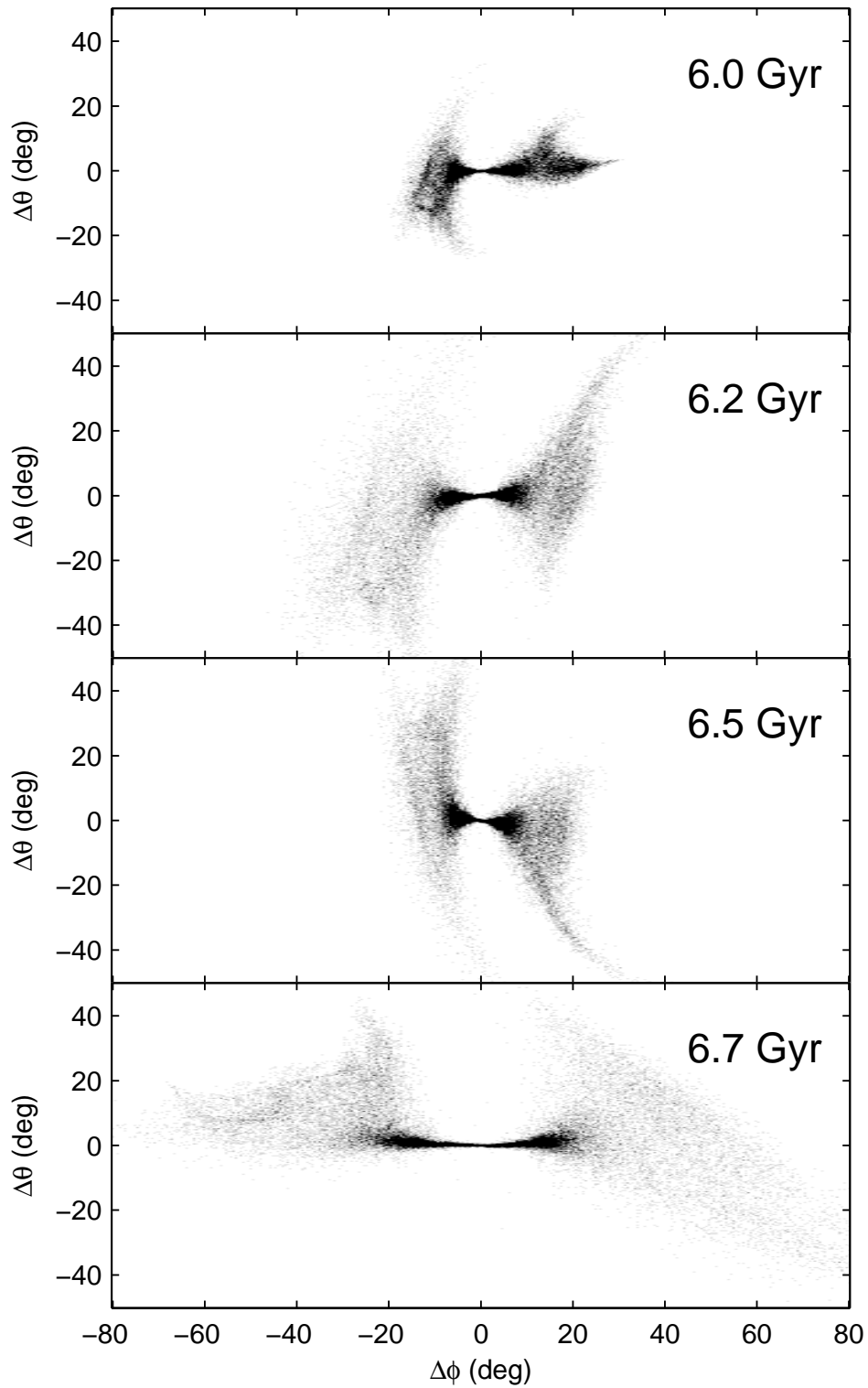


Figure 3.15: Same as Figure 3.13, but in the lumpy halo. The stream overall appears similar to the case in the smooth halo, but the diffuse ends of the stream are even more prominent, and sometimes even wider than the narrow part of the stream itself.

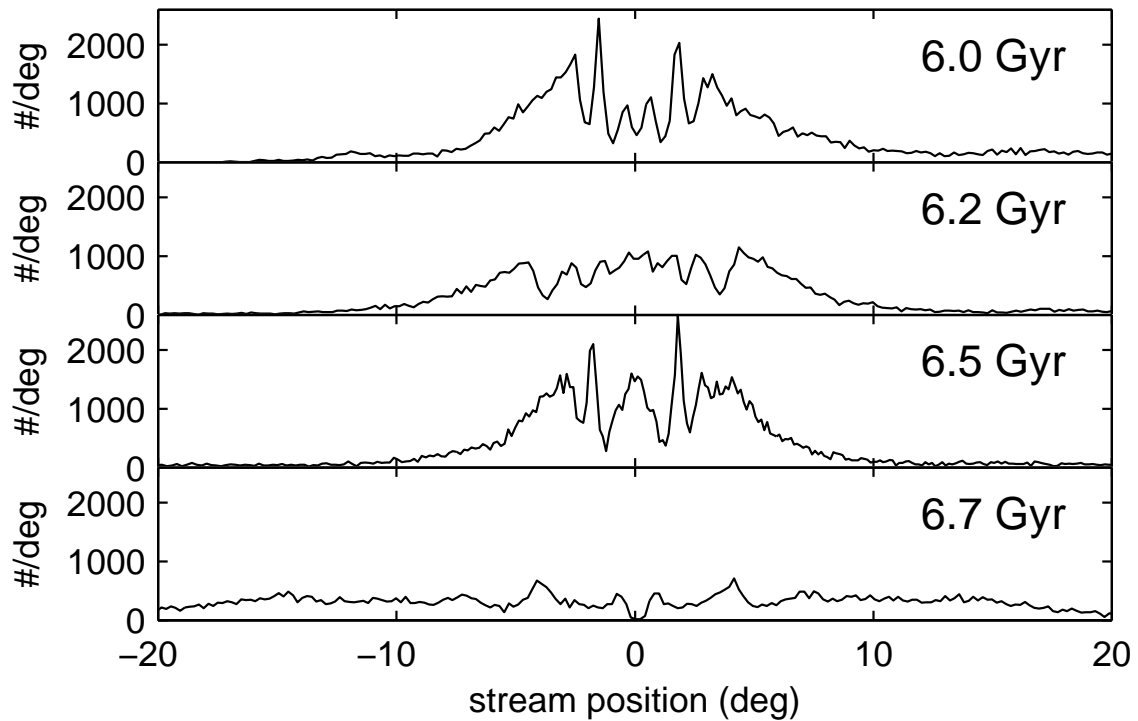


Figure 3.16: Linear density corresponding to the same stream shown in Figure 3.15. Similar to the case in the smooth halo, linear density is only appropriate at the regions near the progenitor where the stream is narrow. Aside from the density spikes near the progenitor, the density profile is smooth and featureless.

The SCF method (Hernquist & Ostriker, 1992) has previously been applied to the Aquarius simulations (Springel et al., 2008; Lowing et al., 2011) as a tool to study dynamics inside existing high-resolution simulations of dark matter halos. For the first time, we applied it to the VL-2 simulation to examine the subhalos’ dynamical influence on tidal streams. The SCF method is a powerful and parallelizable method that efficiently computes the potential to arbitrary accuracy using a set of complete and bi-orthonormal basis functions.

The potentials in the main halo and all the subhalos were constructed using the SCF method. When the subhalo particles were removed from the main halo, the main halo’s potential was constructed using an order 10 decomposition to ensure that the main halo remained smooth and contained no granularities due to the removal of its subhalos. After the subhalos’ individual potentials were also constructed, they were added to the smooth halo in orbits with the initial positions and velocities as found by the halo finder. This eliminated the need for any assumptions for the profiles and distributions for the subhalos in the lumpy halo.

We simulated the tidal disruption of a star cluster as an N-body system that used the main halo’s and subhalos’ potentials as external forces. The cluster followed two orbits, one with initial velocity with zero z component (“Stream 1”), and another with the same speed but inclined from the xy -plane by 70° (“Stream 2”). In a potential without spatial symmetry, neither orbit was confined to any orbital planes, but both orbits were chosen to have apo- and pericentric distances at about 30 and 17 kpc, respectively. These values are comparable to the inferred orbit of GD-1 from observations (Grillmair & Dionatos, 2006; Willett et al., 2009). We simulated each stream in both the smooth halo and the lumpy halo.

Stream 1 remained narrow for 10 Gyr, with length-to-width ratio $\simeq 50$, which was comparable to the observations of GD-1. Even though the smooth halo had no spatial symmetry, we still found density spikes that were similar to EOs near the stream progenitor. In the smooth halo, there were density fluctuations along the stream that were not found in a spherical halo, but the fluctuations were not as prominent as the ones found in the stream in the same orbit but in a lumpy halo. In the future we aim to repeat analyses similar to Ngan & Carlberg (2014), which used gap size distributions to distinguish “intrinsic” gaps and subhalo gaps in streams. Since gap size distributions are observable (Carlberg & Grillmair, 2013), understanding them for simulated streams in a realistic halo is an essential step for comparing simulations and observations.

Stream 2 was narrow only up to 10° – 20° away from the progenitor as seen by a hypothetical observer situated at the galactic center. Further along the stream from the narrow part, the stream developed fluffy features that were almost as wide as, if not wider than, than the length of the narrow part of the stream. We found that density spikes, similar to the ones in Stream 1, near the progenitor dominated the linear density along the narrow part without any distinguishable signatures of subhalos. However, in the lumpy halo, the stream featured wider and even more diffuse tails than in the smooth halo. This means that in the lumpy halo the stream may be even more difficult to observe than in the smooth halo.

Dynamics in the VL-2 halo potential is beyond the scope of this study. In this study we used only two streams in two arbitrary but similar orbits to illustrate the VL-2 halo’s complexity compared to idealized and spherical halo models that were used in previous studies (Yoon et al., 2011; Carlberg, 2013; Ngan & Carlberg, 2014). In a spherical halo, our two streams in this study would appear identical and would not reveal the complicated morphologies especially demonstrated by Stream 2. As concluded by Price-Whelan et al. (2015), Stream 2’s diffuse appearance is due to the chaotic behavior in frequency space, and applying that analysis to orbits in the VL-2 potential would be an illuminating exercise.

Nevertheless, in the next chapter we use this VL-2 model to simulate more streams in more orbits and to perform more empirical analysis to each stream.

Chapter 4

Dispersal of Tidal Debris in a Milky-Way-sized Dark Matter Halo

Abstract

We simulate the tidal disruption of a globular star cluster in 100 different orbits constrained to have apogalacticon radii less than 30 kpc. We compare the dispersal of the tidal debris in a spherical halo and a realistic halo. For each case, we also investigate the subcases with and without the presence of subhalos. We find that the overall halo's symmetry has a larger effect on the dispersal of tidal debris than subhalos do, consistent with previous studies of tidal debris of dwarf galaxies in larger orbits than ours in this study. On the other hand, subhalos in realistic potentials can locally enhance the densities along the streams, making the streams denser than their counterparts in smooth potentials. Of the 100 simulated streams in randomly distributed orbits in the realistic halos, we find that on average about 5 to 15 of them approach a volume of a few kiloparsecs at the solar circle, and some of those streams remain cold and thin. This suggests that upcoming surveys using both astrometry and high-resolution spectroscopy will likely uncover more cold and thin streams with velocity dispersion of a few kilometers per second, which may contain density gaps that have been shown to be promising probes for dark matter substructures.

4.1 Motivation

As shown in the previous chapter and recently in Pearson et al. (2015), streams inside the Via Lactea II (VL-2) and triaxial potentials, respectively, exhibit “fluffy” features in the tails of the streams which are not found in streams inside spherical potentials. This is evidence that spherical halos may not be sufficient for studies that simulate the disruption of satellite systems (e.g., Bullock & Johnston, 2005). The results of this chapter, as we will show, indicate that streams inside a realistic potential are more dispersed than streams inside a spherical halo.

The goal of this study is to investigate how dispersed tidal streams are in a realistic halo, and whether those streams would remain cold and thin for a Hubble time so that large stellar surveys in the near future might be able to observe them. We simulate 100 tidal streams as self-gravitating N-body simulations of the same globular star cluster orbiting inside a host halo, where each orbit has a different initial position and velocity. These star clusters are tidally disrupted to form streams in four different cases of host halos: (a) a spherical halo with no subhalos, (b) a spherical halo with subhalos, (c) the VL-2 halo with no subhalos, and (d) the VL-2 halo with subhalos. In all cases, the host’s and subhalos’ potentials are not evolving in time, although subhalos orbit around the host’s potential as test masses. A time dependent potential is an important step in the future, but we believe that the effects of a realistic potential itself is worth studying before including the additional complication of time dependence.

This chapter is organized as follows. Section 4.2 is the method section which contains several subsections. Section 4.2.1 reviews the SCF method to obtain the potential from the VL-2 halo and subhalos. Section 4.2.2 describes our spherical halo which will be compared against the VL-2 halo. Section 4.2.3 justifies the mass range of subhalos included in the lumpy halo cases. Section 4.2.4 describes the initialization of the stream progenitor, including its density profile and its orbits. Section 4.3 contains our results. In particular, Sections 4.3.1 and 4.3.2 compare the dispersal of tidal debris in the spherical and the VL-2 halos, and Sections 4.3.3 and 4.3.4 use our results from the VL-2 halo to predict the distribution of streams that will be uncovered in the near future. Section 4.4 summarizes our results.

4.2 Method

4.2.1 VL-2 Halo and Subhalo Potentials

The smooth and lumpy VL-2 potentials are obtained using the same method detailed in Ngan et al. (2015), which uses a combination of the self-consistent field (SCF) method (Hernquist & Ostriker, 1992) and a halo finder code to construct the gravitational potentials inside the host halo and subhalos. The SCF method has also been applied by Lowing et al. (2011) to the dark matter halos in the Aquarius simulations (Springel et al., 2008). In this section we summarize the method.

The method begins by specifying a set of basis functions $\Phi_{nlm}(\mathbf{r})$ and solves the Poisson equation in spherical coordinates $\mathbf{r} \equiv (r, \theta, \phi)$ for the potential in the form

$$\Phi(\mathbf{r}) = \sum_{n=0}^{n_{max}} \sum_{l=0}^{l_{max}} \sum_{m=0}^l A_{nlm} \Phi_{nlm}(\mathbf{r}). \quad (4.1)$$

Given a list of particle positions and masses stored in an existing snapshot of a high-resolution simulation, the SCF method provides a recipe to obtain the basis coefficients A_{nlm} , and then the force field $-\nabla\Phi$ can

be computed analytically by differentiating Equation (4.1). In this study, following Lowing et al. (2011) and Ngan et al. (2015), the zeroth order basis function (Equation 3.3) is in the form of a Hernquist profile (Hernquist, 1990), and the higher order radial and angular deviations are polynomials in r of degree n and spherical harmonics in (θ, ϕ) of orders l and m .

The smooth VL-2 potential is obtained by the SCF method using order 10 (where $n_{max} = l_{max} =$ order) on the VL-2 main halo after its subhalo particles have been removed. This order ensures that the overall shape of the main halo is captured without the lumpiness due to either the presence of subhalos or the voids after the subhalos are removed, since a polynomial of degree 10 is not sufficient to model more than 10,000 subhalos (Ngan et al., 2015). The details of subhalo abundance are discussed in Section 4.2.3.

4.2.2 Spherical Halo Potential

The spherical halo is modelled using a Navarro-Frenk-White profile (NFW, Navarro et al., 1997)

$$\Phi(r) = -v_h^2 (r/r_h)^2 \ln(1 + r/r_h) \quad (4.2)$$

where r_h and v_h are the scale radius and the circular velocity at r_h . Bonaca et al. (2014) performed fits to the VL-2 halo at various redshifts and enclosed masses inside the halo. Since we are comparing halo models at redshift zero and our streams orbit well inside $r \lesssim 30$ kpc (Section 4.2.4), we adopt the best fit results from Bonaca et al. (2014) inside 20 kpc at present day, where $v_h = 425 \text{ km s}^{-1}$ and $r_h = 18$ kpc.

Figure 4.1 shows that the enclosed masses for our VL-2 and spherical halos agree to within about 10% for the regions inside $r \lesssim 30$ kpc. This ensures that the dimensionless tidal scale s , which is the ratio between the star cluster’s tidal radius and its orbital perigalacticon radius, are comparable between the two types of halos in this study, for the same star cluster mass and similar orbits. In another form, s can also be written as

$$s \equiv \left(\frac{m}{M_p} \right)^{1/3}, \quad (4.3)$$

where m is the star cluster mass, and M_p is the mass of the host halo enclosed by the pericentric distance of the cluster’s orbit. Johnston (1998) and Johnston et al. (2001) found that in a spherical potential, s determines the spreads in energy and angular momentum, which in turn determine the width and length of a stream. As we show later in our results, however, in a VL-2 halo a stream can be wider and more dispersed than in a spherical potential.

4.2.3 Subhalo Finding

The lumpy host halos are simply the smooth host halos with extra subhalos orbiting in them. The subhalos of the host halos are identified and extracted from the zeroth redshift snapshot of VL-2. The potential inside each subhalo is then computed using the SCF method described above, but with $n_{max} = 4$ and $l_{max} = 0$. To ensure a fair comparison, all the subhalos in both the VL-2 and spherical host halos are modelled identically. The subhalos are assumed not to interact with each other and orbit the host halos as test masses, and they use the positions and velocities as reported by the halo finder as orbital initial conditions.

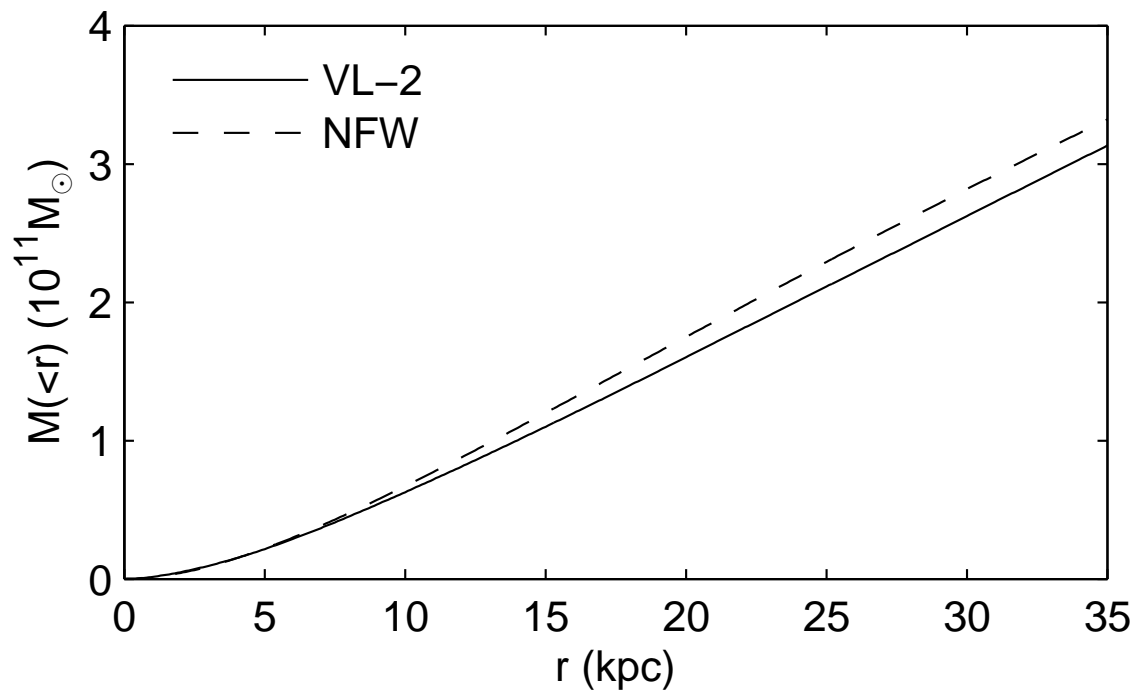


Figure 4.1: Enclosed masses of the two smooth halos used in this study. The mass of the VL-2 is computed by directly summing the masses of all the particles inside r , and the mass of the spherical halo is obtained analytically from the NFW profile. Their masses agree to within 10% for $r \lesssim 30$ kpc.

We identify 11,523 subhalos in total in the main halo in the zeroth redshift snapshot of VL-2, which is consistent with the abundance reported by Diemand et al. (2008). In each lumpy case, we further consider two sub-cases with two different mass ranges M_{sub} of subhalos: (i) all subhalos with $M_{sub} > 10^7 M_\odot$ and (ii) all subhalos with $M_{sub} > 5 \times 10^6 M_\odot$, where the most massive subhalo is $4.7 \times 10^9 M_\odot$ in both mass ranges. Our halo finder reports totals of 1087 and 2007 subhalos for the two mass ranges, respectively. As opposed to Ngan & Carlberg (2014) and Ngan et al. (2015), here we do not impose an upper limit for subhalo masses because our goal is to investigate the major perturbations on tidal streams, rather than small perturbations such as gaps in them (Yoon et al., 2011; Carlberg, 2012, 2013; Ngan & Carlberg, 2014; Ngan et al., 2015). Note that this means the subhalo with the highest mass in this study is more massive than those in Ngan et al. (2015).

Similar to Ngan & Carlberg (2014) and Ngan et al. (2015), in our actual simulations we do not include the subhalos which interact minimally with the streams, as some subhalos have pericentric distances that are greater than the streams' apocentric distances. As explained below, our stream orbits are restricted to a maximum apocentric distance of 30 kpc. Therefore, subhalos with pericentric distances greater than 40 kpc can be safely eliminated. For the mass ranges of subhalos mentioned above, only 381 and 674 subhalos, respectively, remain for the VL-2 potential, and 318 and 565 subhalos, respectively, remain for the spherical potential.

Because the lumpy halos are essentially the smooth halos with extra subhalos, lumpy halos are more massive than smooth halos. In the VL-2 halo, 381 and 674 subhalos are about 1.6% and 1.7% of the mass of the smooth halo, respectively. In the spherical halo, 318 and 565 subhalos are about 1.2% and 1.3% of the mass of the smooth halo, respectively. In Ngan & Carlberg (2014) and Ngan et al. (2015), stream progenitors with the same initial conditions travel in roughly the same orbit in both smooth and lumpy halos because each subhalo's mass is low enough that each subhalo individually does not affect the streams' orbits much. In this study, however, stream progenitors travel in very different orbits in smooth and lumpy potentials because most of the subhalo masses are concentrated in the most massive subhalos, which can affect the streams' orbits. As shown in Yoon et al. (2011), the characteristic energy that a $\sim 10^9 M_\odot$ subhalo deposits into a stream is $\sim 10^4 \text{km}^2 \text{s}^{-2}$, and this corresponds to the orbital energy $E \propto v_{orbit}^2 \sim (200 \text{km s}^{-1})^2$ of a GD-1-like stream whose orbit oscillates radially between 15 – 30 kpc. Therefore, subhalos more massive than $\sim 10^9 M_\odot$ can significantly affect the orbit of the stream progenitor, hence the entire stream itself. This is the reason the smooth and lumpy halos cannot be compared directly using only one stream in each case when simulations include high mass subhalos. Smooth and lumpy halos can only be compared by the statistics of many streams as we discuss in our results in Section 4.3.

4.2.4 Stream Progenitor and Orbits

The progenitor for all streams in this study is a self-gravitating N-body star cluster following the King profile with $w = 2$, where w is the ratio between the central potential and velocity dispersion of the cluster. We initialize the cluster with core radius $r_0 = 0.05$ kpc and mass $M = 5 \times 10^4 M_\odot$, and this yields a cluster with tidal radius ~ 0.15 kpc (beyond which the density is zero) and velocity dispersion $\sim 1 \text{km s}^{-1}$.

The random orbits in our simulations are selected as follows. We first place 10,000 random points following a uniform distribution inside a spherical shell between 15 and 30 kpc in radius. Each point is also assigned uniformly random velocities between -300 and 300km s^{-1} for each of the v_x, v_y, v_z

components. We then use these positions and velocities as initial conditions to integrate 10,000 test particle orbits for 10 Gyr inside both smooth VL-2 and spherical potentials.

In the VL-2 potential, we randomly select 50 orbits (hereafter “outer orbits”) such that their galactocentric distances r are bounded by $10 \text{ kpc} < r < 30 \text{ kpc}$ for 10 Gyr, and another 50 orbits (hereafter “inner orbits”) such that $r < 30 \text{ kpc}$ but $r_{min} < 10 \text{ kpc}$ in 10 Gyr. The resulting eccentricity distribution of these 100 orbits selected from this process is shown in Figure 4.2. Here eccentricity is defined as

$$e = \frac{r_{max} - r_{min}}{r_{max} + r_{min}} \quad (4.4)$$

where r_{max} and r_{min} are the maximum and minimum r attained by the test particle in 10 Gyr. The initial conditions of these 100 orbits serve as the stream progenitor’s initial conditions for the streams’ orbits inside the both the smooth and lumpy VL-2 potentials.

In the spherical potential, we repeat a similar process which also selects 100 orbits as “inner” and “outer” sets with the same limiting r . However, to ensure a fair comparison, the orbits are selected such that they produce identical eccentricity distribution, shown in Figure 4.2, as the VL-2 case. Similarly, these 100 orbits are the orbits for the streams inside both the smooth and lumpy spherical potentials.

Note that a star cluster with a density profile described above is completely disrupted after about a few gigayears in our orbits, as shown in Figure 4.3. This ensures that computational efforts are well spent, especially because each individual stream is a fully self-gravitating N-body simulation. Our goal is to study the dynamical evolution of tidal tails and not the progenitor, so N-body particles that remain bound to the progenitor are irrelevant to our study. Also demonstrated in Figure 4.3 is that for the same type of host halo and orbits, the median mass loss in smooth and lumpy halos are almost the same. This means that mass loss due to subhalo shocking is rare, and that particles inside the progenitor can be safely ignored. We have repeated our simulations with a more tightly bound progenitor with the same mass and tidal radius. We find that although the resulting streams are represented with fewer particles, our results are almost identical to the ones produced using the progenitor described above, which we will adopt for the rest of our results.

4.2.5 Simulation Details

The simulations of tidal streams and extraction of subhalos in this study use the same code as in Ngan et al. (2015). The N-body simulations are run using the public version¹ of GADGET-2 (Springel, 2005). The accelerations due to both the host halo and subhalos are added to the particles after their N-body forces have been computed. We impose a maximum time step of 1 Myr and softening of 5 pc on each particle.

The subhalos inside the VL-2 halo are identified using the AMIGA HALO FINDER². Inside the main halo of VL-2, we consider only the subhalos which are the immediate satellites of the main halo, such that all the satellites of a given subhalo (including all the hierarchically smaller satellites) are all considered part of that subhalo. For each subhalo, the halo finder returns the positions and velocities which are used to initialize the subhalo’s orbit around the main halo, as well as masses and radii which are used to construct the subhalo’s potential using the SCF method.

¹<http://www.mpa-garching.mpg.de/gadget/>

²<http://popia.ft.uam.es/AHF/Download.html>

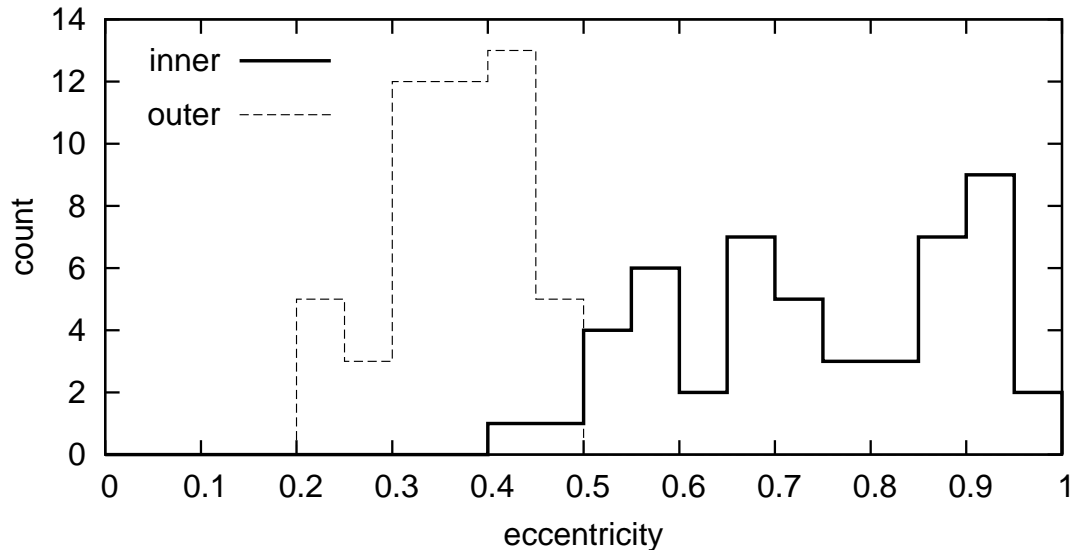


Figure 4.2: Eccentricities of the random orbits of the 100 streams used in each halo potential. The “outer” set contains 50 orbits whose galactocentric distances r are bounded by $10 \text{ kpc} < r < 30 \text{ kpc}$ for 10 Gyr. The “inner” set contains another 50 orbits bounded by $r < 30 \text{ kpc}$, but $r_{min} < 10 \text{ kpc}$ in 10 Gyr. The sets of orbits in the VL-2 and spherical potentials are different, but they have identical eccentricity distribution.

4.3 Results

4.3.1 Effects of the Underlying Halo

Figures 4.4 and 4.5 show the sky projection of 100 streams at 6 Gyr, as seen from the galactic center, combined into the same images for the four cases of interest in this study. The top panels of the two figures show that the shape of the smooth halo plays an important role in affecting the dispersal of the tidal debris. On the other hand, the top and bottom panels in each figure show that the effects that subhalos have on the streams are not as pronounced as the effect that the shapes of the underlying halos do. This finding is similar to the conclusion from Siegal-Gaskins & Valluri (2008) which simulated the disruption of satellite galaxies that were much more massive and orbited at larger galactocentric radii (ie. larger s from Equation 4.3) than our streams. In this study we simulate the disruption of a low mass globular cluster orbiting at smaller galactocentric radii, which result in streams (at least in the set of outer streams) that are $\lesssim 1^\circ$ as seen from the galactic center.

Figures 4.4 and 4.5 can also be thought of as the progress over the past decade or so in modelling the tidal disruption of satellite systems. For example, to simulate the build up of Milky Way’s stellar halo, studies such as Harding et al. (2001) and Bullock & Johnston (2005) used idealized potentials to simulate the disruption of satellite galaxies. Streams simulated using those models would be analogous to (but more sophisticated than) the the top panels of Figure 4.4. In other studies for detecting substructures in the CDM context of structure formation, Ibata et al. (2002); Johnston et al. (2002); Yoon et al. (2011); Ngan & Carlberg (2014) added extra subhalos on top of the host halo, where all potentials made use of idealized profiles. The streams in those studies are analogous to the bottom panels of Figure 4.4 which

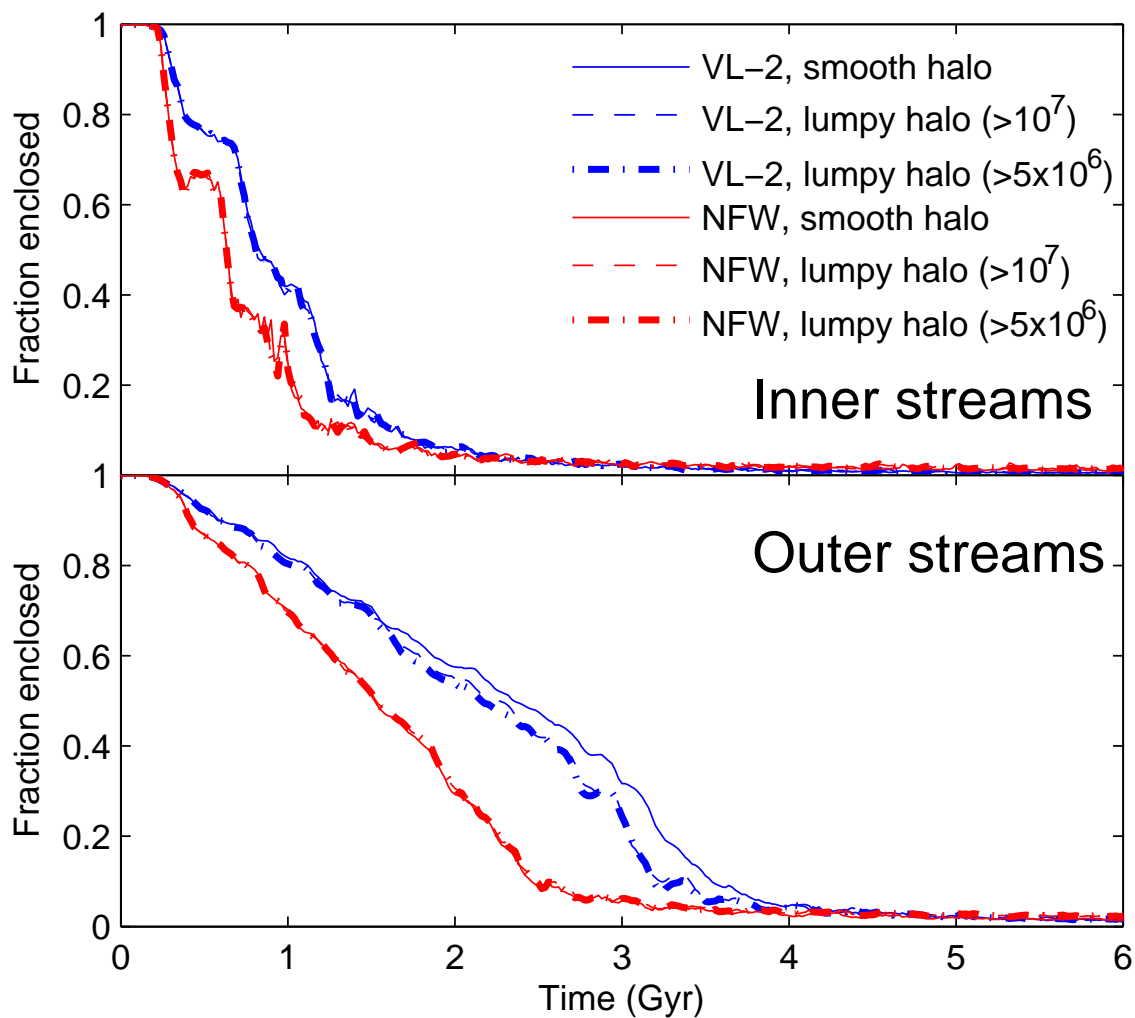


Figure 4.3: Fractions of particles enclosed in a radius 0.16 kpc of the progenitors as functions of time. Each line represents the median of 50 streams at each instant of time, where the dashed and the thick dash-dotted lines represent the lumpy halos with subhalo mass ranges indicated in solar masses. Top and bottom panels show the inner and outer sets of streams, respectively. In each case, the mass loss is primarily caused by the tidal stripping at the progenitors’ pericentric approaches, and not by subhalo shocking.

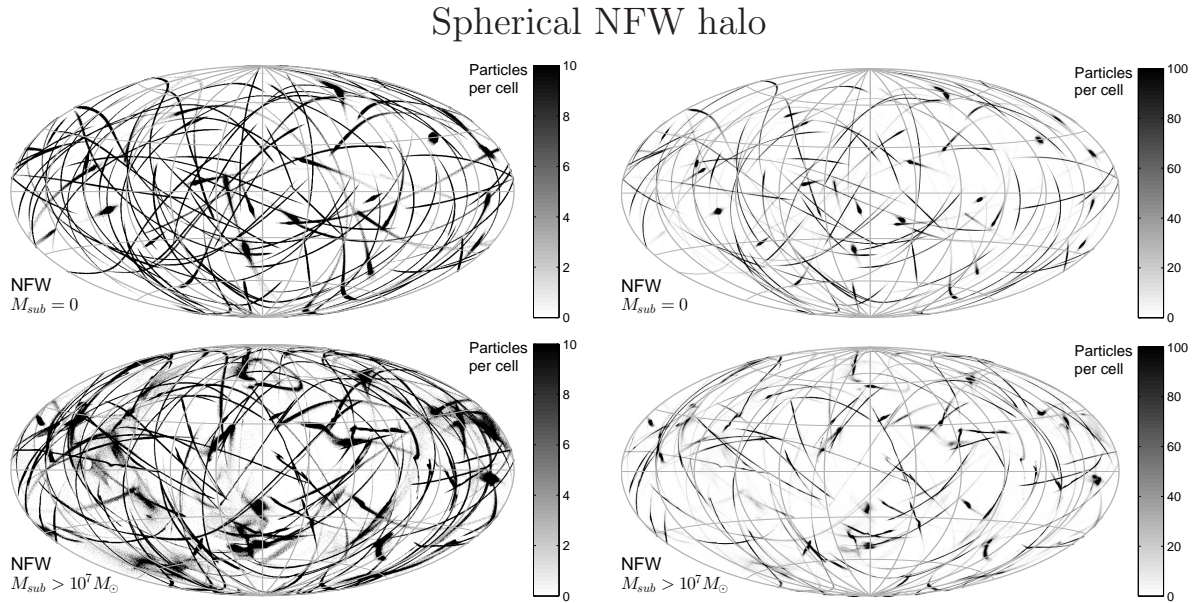


Figure 4.4: Hammer-Aitoff equal-area projections of 100 streams on the sky at 6 Gyr as seen from the galactic center. Each panel shows the combined surface density of particles in 0.3° cells. Top and bottom rows show the streams in a smooth spherical halo and a lumpy spherical halo with $M_{sub} > 10^7 M_{\odot}$, respectively. Left and right columns show the same maps, but their gray scales are adjusted to exaggerate the diffuse and dense cells, respectively. All stream orbits are chosen to have maximum galactocentric distances at less than 30 kpc (see text for details). The orbital initial conditions of the 100 streams are the same in top and bottom panels, but the streams travel in different orbits due to the influence of the subhalos. The case where $M_{sub} > 5 \times 10^6 M_{\odot}$, not shown here, produces similar maps to the bottom panels.

show that subhalos can disperse tidal debris to some extent. It was not until recently when Bonaca et al. (2014) and Ngan et al. (2015) simulated tidal streams inside the potential of the high-resolution halo of VL-2 directly without fitting the potential to any idealized profiles. Their results are analogous to the streams in Figure 4.5, which differ significantly from those in Figure 4.4. We quantify these differences in the following section.

4.3.2 Dispersal of Tidal Debris

We now present an empirical analysis of the streams in the four cases of halos of interest. For each stream, each particle is assigned into its nearest rectangular grid cell by its three-dimensional position. The occupancies η of the grid cells are similar to the number densities of the streams, but we caution that our grid cells with 0.1 kpc on each side may be too coarse to be interpreted as measurements of density. This grid size is similar to the width of GD-1 at 70 pc wide (Grillmair & Dionatos, 2006; Carlberg & Grillmair, 2013), which is considered a very narrow stream with a derived orbit similar to the streams in the outer streams in this study (Willett et al., 2009). Our grid size is chosen so that it is sensitive to the particles that have been dispersed away from the main track of the stream by more than that distance.

Note that even though the densities of streams with different orbits cannot be compared directly,

Via Lactea II halo

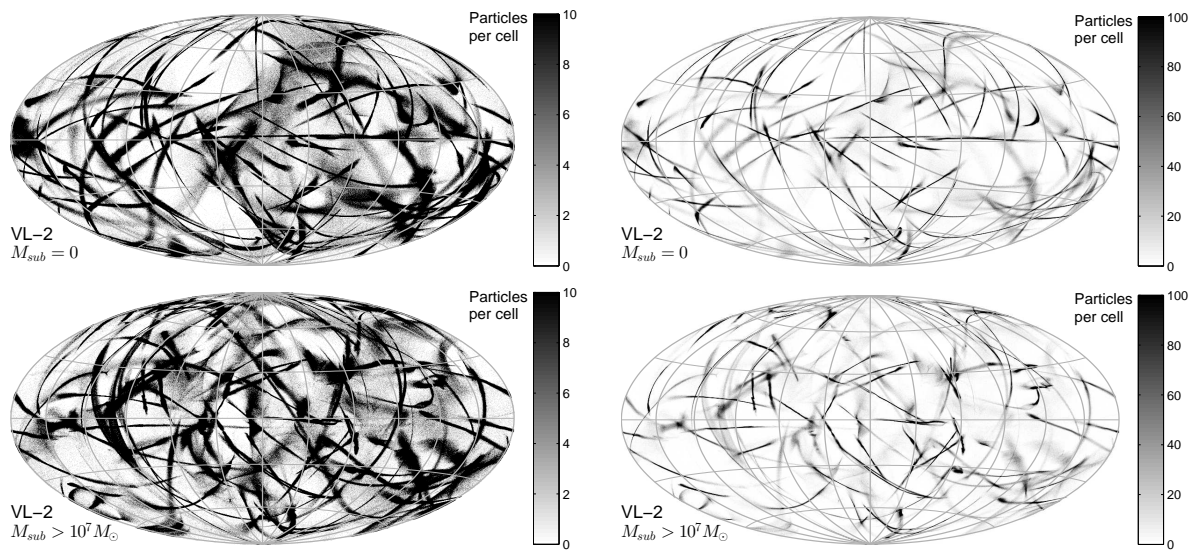


Figure 4.5: Similar to Figure 4.4, but the underlying halo is the VL-2 halo at redshift zero. Compared to the spherical halo in Figure 4.4, the streams in the VL-2 halo appear much more dispersed, especially in smooth halo (top panels). Note that the orbits of the streams in this figure are selected by the same criteria and result in the same eccentricity distribution as the orbits in Figure 4.4.

distributions of the cell occupancies $f(\eta)$ can tell us how dispersed each stream is. If a stream remains narrow without much dispersal, the occupancy of the grid would be dominated by a few densely occupied cells. On the contrary, if a stream is very dispersed, then the occupancy of the grid would be spread among many sparsely occupied cells.

Figure 4.6 shows the medians of the cumulative distributions of grid occupancies of 50 streams in each of our halo potential. The cumulative distributions have been weighted by the occupancies and then normalized by the total numbers of particles. More precisely, the y-axes are

$$F(\eta) = \frac{1}{N} \sum_{k>\eta} kf(k) \quad (4.5)$$

where $N = 50,000$ is the total number of particles in each stream. In the bottom left panel of Figure 4.6, the streams in the VL-2 halos clearly show a tail in the dense end of the distribution. This tail represents the progenitor, as seen in Figure 4.3 above. At 3 Gyr, the progenitors of all but the outer streams in the VL-2 halo have been dissolved, so the particles that remain in the progenitors clearly occupy a few cells which are denser than the rest of the streams. The differences in cell occupancies between the VL-2 and the spherical halo begin to show at 6 Gyr, and become prominent at 9 Gyr. At both times, the streams in the spherical halo (red lines) are consistently denser than the streams in the VL-2 halo (blue lines). The difference is especially large for the inner streams as we do not impose a lower limit in pericentric distances, so the inner streams can approach arbitrarily close to the halo’s center. In addition, even streams in only mildly eccentric orbits in triaxial potentials are also known to produce “fluffy” features which are not seen in spherical potentials (Ngan et al., 2015; Pearson et al.,

2015).

Perhaps a surprising result is the effects of subhalos (dotted lines in Figure 4.6). On one hand, subhalos can scatter stars away from a stream’s path, decreasing the overall density of the stream. This is the impression of Figures 4.4 and 4.5 where streams in the presence of subhalos tend to be fluffier, and this is indeed the case for the inner streams in the spherical halo (red lines in the upper panels in Figure 4.6). On the other hand, both the inner and the outer streams in the VL-2 halo (blue lines in Figure 4.6) indicate that streams in the presence of subhalos contain parts that can be denser than the streams in the smooth halo. Therefore, even though the presence of subhalos do not affect streams as much as the shape of the halo does, subhalos can potentially make streams slightly easier to detect.

The increase in density can be understood by the conservation of mass. Carlberg (2012) and Erkal & Belokurov (2015) showed that as a stream of particles encounters a subhalo, the stream’s longitudinal density profile not only produces an underdensity which is observed as a gap, but also overdensities in the immediate vicinities of the gap. As we show in the next section, the densest streams in the presence of subhalos are not necessarily narrow streams, but clumps due to subhalo perturbations.

Each panel in Figure 4.6 contains two broken lines, one for each subhalo mass range. The two broken lines are almost identical, which means that subhalos with $5 \times 10^6 M_\odot < M_{sub} < 10^7 M_\odot$ are not important for dispersing tidal tails. Rather, low mass subhalos can produce small scale gaps in streams as shown in Ngan et al. (2015) using the subhalos in the mass range $10^8 M_\odot < M_{sub} < 6.2 \times 10^5 M_\odot$ in the VL-2 halo.

4.3.3 The Densest Streams in the VL-2 Halos

Figures 4.4 and 4.5 have another interesting implication. In the VL-2 halo with subhalos (the most complicated case) some streams remain coherent and narrow. In observations, these streams with the densest parts would be much more easily detectable than streams which are more dispersed. For the rest of our results, we focus on the streams in the VL-2 halos. Our goal is to predict both the positional and kinematical distributions of the streams that will be uncovered by large surveys in the near future in the Milky Way, to which realistic halos can provide more insights than a spherical halo. In this section we investigate the densest streams in the VL-2 halos.

In order to avoid confusing the stream progenitors as trivially the densest points in the streams, we investigate the streams at 9 Gyr when almost all the stream progenitors have been dissolved. Similar to the previous section, we let all stream particles occupy the nearest 3D grid cell of 0.1 kpc on each side, and we consider the densest cell of each stream. In other words, we consider the streams which contain cells that are in the dense tail of the distributions in Figure 4.6. The sky projections of a few of the densest streams are shown in Figure 4.7.

In the smooth VL-2 halo, after the progenitor has been dissolved, the densest streams in the smooth halo are extremely narrow. In Figure 4.7 both streams A and B are compressed transversely as they undergo pericentric passages. In particular, stream B has peri- and apocentric distances at 5.2 and 23 kpc, respectively. This shows that streams in eccentric orbits inside the smooth VL-2 halo can remain narrow, particularly for the streams whose densities are enhanced as they pass through their orbital pericenters.

In the lumpy VL-2 halo, on the other hand, streams interact with subhalos and exhibit more complicated morphologies than in the smooth halo. For example, in stream D in Figure 4.7, the densest point is found inside the clump in the bottom end of its tail. This clump is clearly not the stream’s progenitor

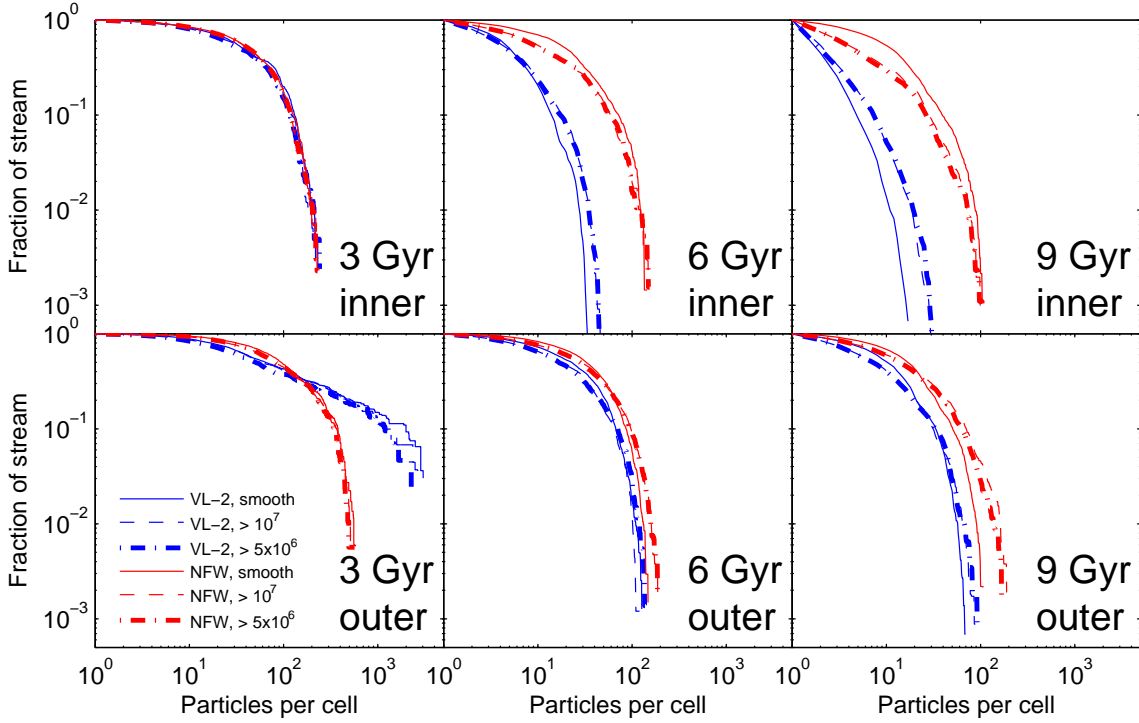


Figure 4.6: Cumulative fractions of the streams as functions of cell occupancy in the VL-2 and the spherical NFW halos. Each line represents the median of 50 streams in each of the “inner” and “outer” sets. The inner set contains streams whose orbits have $r < 30$ kpc and $r_{min} < 10$ kpc, whereas the outer set contain streams whose orbits are bounded by $10 \text{ kpc} < r < 30$ kpc. The thin dashed line and thick dashed-dotted lines represent lumpy halos with subhalo mass ranges indicated in solar masses. The stream particles are assigned to the nearest grid cell at 0.1 kpc on each side. The dense tail at 3 Gyr for the outer stream is the remains of the progenitors that have not been completely dissolved yet (Figure 4.3).

as it is located at the tip of its tail. Rather, it is the result of a previous interaction with a massive subhalo. In a more extreme case, stream F shows that all the tidal debris is compressed into a small clump and no longer appears as a long and thin “stream”. Note that both clumps in streams D and F are undergoing apocentric passages, which compress the clumps longitudinally to momentarily enhance their densities. Nevertheless, not all densest streams in the lumpy VL-2 halo are in the form of clumps. Stream E retains its long and narrow shape similar to streams A and B in the smooth halo. Stream C is a combination of having a narrow stream and a clump located in the bottom end of its tail, where the narrow part is denser than the clump.

Even though the streams in this study do not follow a realistic orbital distribution and are not meant to be physical models of observed streams, some streams in Figure 4.7 bear some resemblance. For example, the length, width, and eccentricity of stream A can be compared to GD-1 at 60° long and $\lesssim 1^\circ$ wide (Grillmair & Dionatos, 2006). In the other extreme, stream F resembles the recently discovered Ophiuchus stream (Bernard et al., 2014; Sesar et al., 2015) at only a few degrees in length, which is exceptionally short. Nevertheless, stream F is undergoing apocentric passage (at ~ 25 kpc away from the galactic center), so the stream’s shortness is because of longitudinal compression.

4.3.4 Streams in the Local Volume

We now investigate the distribution of streams inside a small observable volume centered at 8 kpc away from the galactic center. In addition to overdensities in positions, streams should also be observable as overdensities in velocities. Ongoing surveys such as Gaia will provide both astrometric and spectroscopic data for an unprecedented number of stars in the Milky Way. Our simulations allow us to predict the velocity distributions in streams in a realistic dark matter halo.

The drawback of measuring velocities, however, is that it is much more difficult than measuring positions. Accurate three dimensional velocities may only be available for stars no more than a few kiloparsecs away from the Sun. For example, a magnitude $M_V = +4$ star at 3 kpc away would have proper motion error of $\sim 0.3 \text{ km s}^{-1}$, as indicated by the pre-launch predictions of Gaia (de Bruijne, 2012). Even when combined with high-resolution spectroscopy from the ground, a velocity error of 0.3 km s^{-1} is needed to detect cold streams that have velocity dispersions of a few kilometers per second. For this reason, we study the velocity dispersions in the streams inside small volumes of radius d centered at 8 kpc away from the galactic center. Figure 4.8 shows how 25 spherical volumes with $d = 3$ kpc radius each are packed together such that all the volumes are centered at 8 kpc away from the center without significant overlap. This gives us 25 independent samples of local volumes in which we can study velocity dispersions. Note that some streams may only have very small numbers of particles inside some volumes. In the following analysis, in each volume we only consider streams which have at least 20 particles.

Numbers of Stream Segments

Figure 4.9 shows the sky projection of the stream segments inside one of the $d = 3$ kpc volumes, as seen from this volume’s center, at 6 Gyr in a lumpy halo. Each point is one stream particle, and the colors are chosen so that the points with the same color originate from the same stream. The large patch of dark blue particles in the left hemisphere in Figure 4.9 is a stream with an eccentric orbit. As it passes near the halo’s central cusp, the stream particles’ orbits become chaotic, and this causes the debris to spread across a large region of the sky. Stellar systems like that, in position space at least, would not be

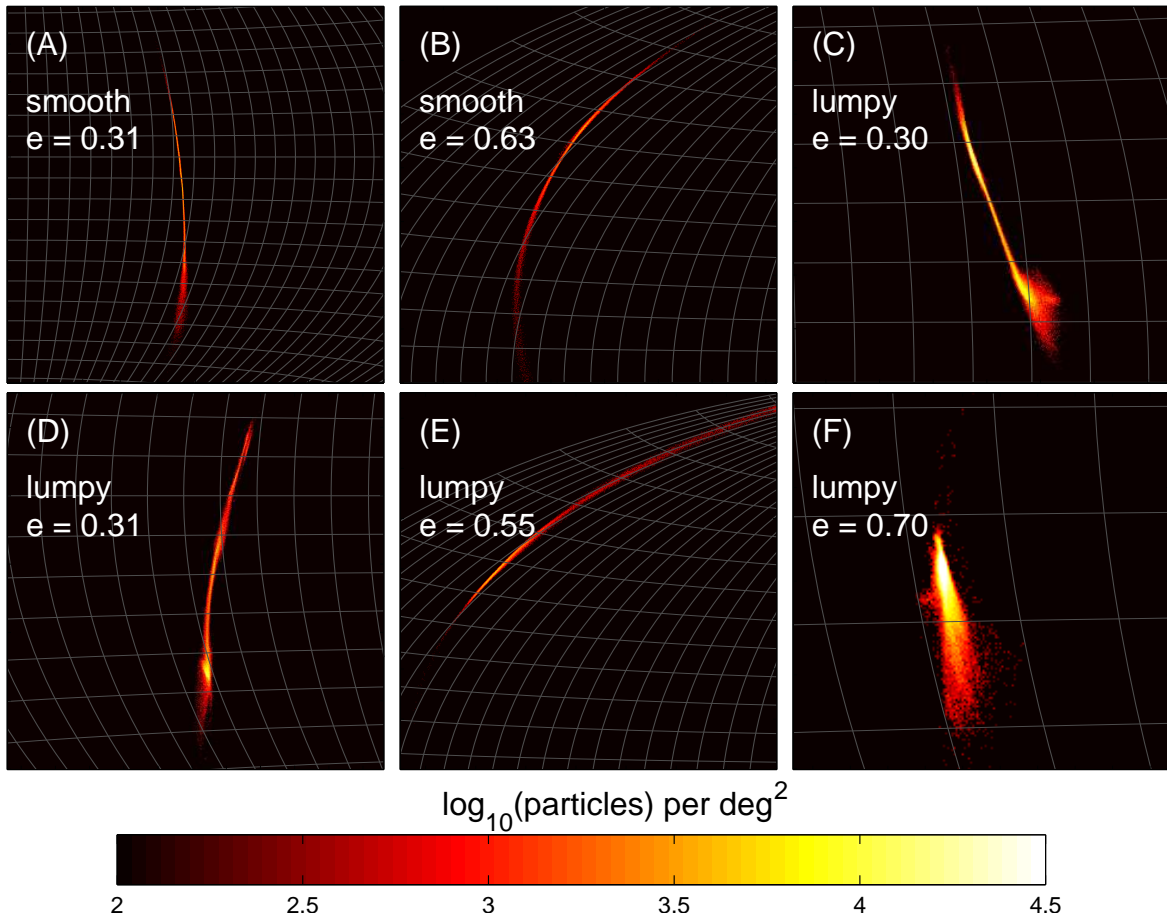


Figure 4.7: Six of the densest streams at 9 Gyr in the VL-2 halo. Each stream is projected onto the sky using Hammer-Aitoff equal-area projection as seen from the galactic center. Both latitudinal and longitudinal grid lines in all panels are spaced at 5° apart. Eccentricities e for the streams in the lumpy halo (C, D, E, F) are quoted for the streams' orbits without subhalos. Note that the color scale is the log of the number of particles in each bin at 0.1° on each side. In the smooth halo, streams A and B remain narrow and are compressed during pericentric passages, which enhance their densities. In the lumpy halo, the densest points of a stream can either be a narrow segment (C and E) or clumping due to subhalo perturbations (D and F).

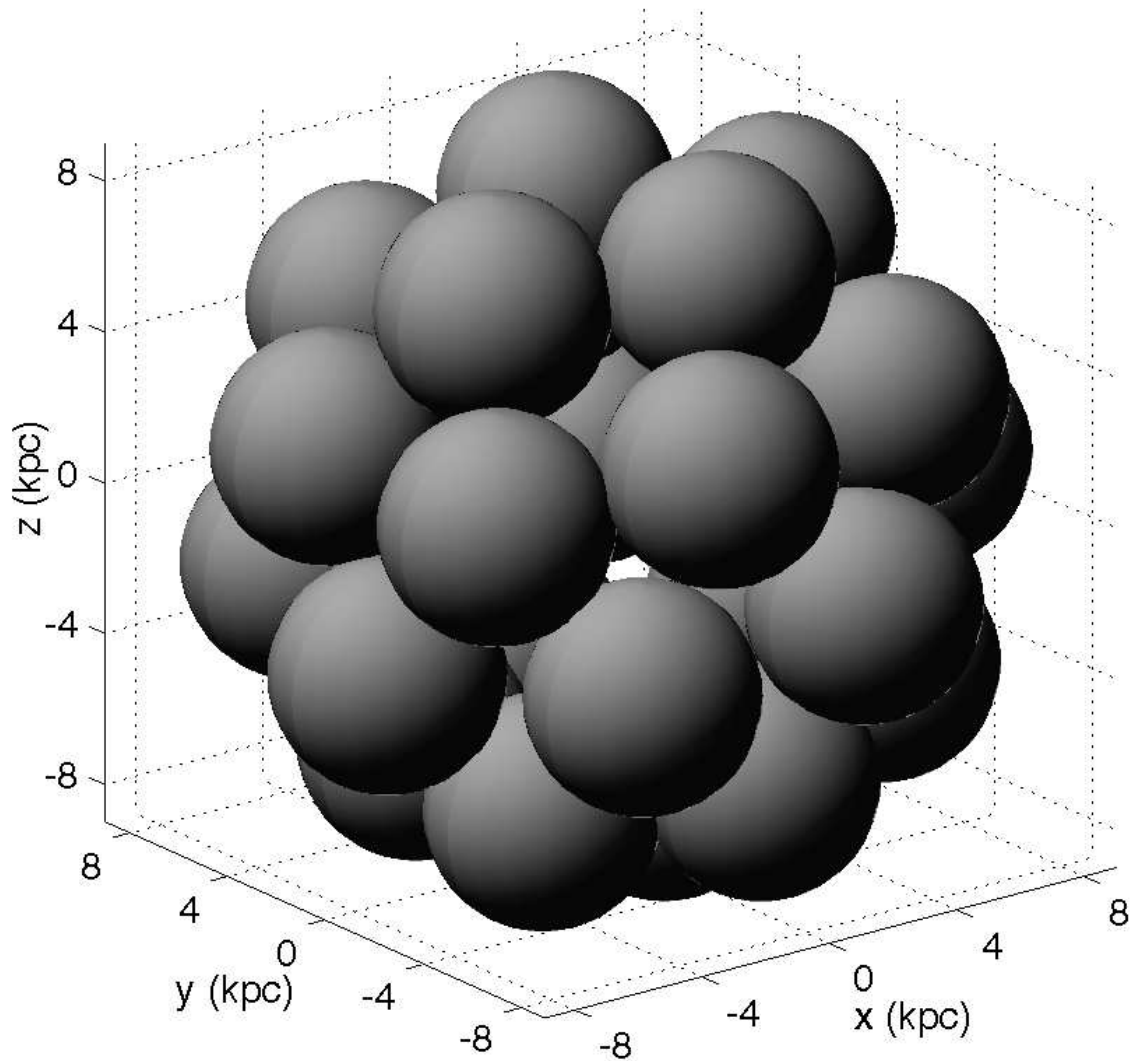


Figure 4.8: Spherical volumes of $d = 3$ kpc in radius packed in a way such that each volume is centered at 8 kpc away from the galactic center. The radius of the volumes is chosen to represent the largest distance which reliable three dimensional velocities can be observed, and the number of spheres are chosen such that the volumes can be packed together as densely as possible without significant overlapping.

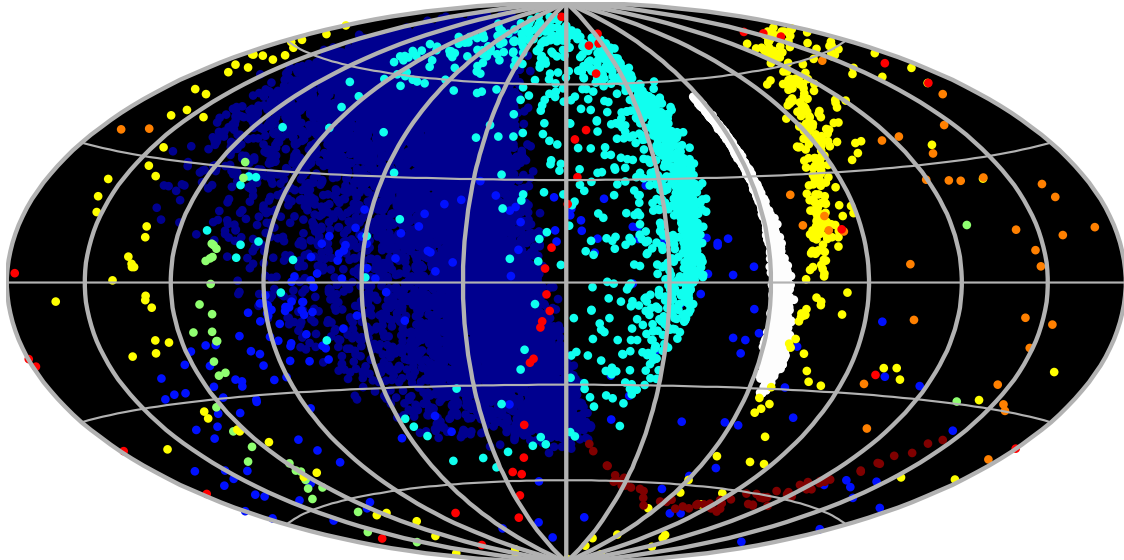


Figure 4.9: Sky projection of stream segments as seen from the center of one of the $d = 3$ kpc volumes in Figure 4.8 at 6 Gyr inside the VL-2 lumpy halo with $M_{sub} > 10^7 M_{\odot}$. Each color identifies the particle members of each stream. A total of 9 streams (with at least 20 particles) are found inside this volume.

identified as a “stream” because of the dispersal of the debris. On the other hand, the white, yellow, and brown streams in the right hemisphere of Figure 4.9 would be detectable as streams, where the brown stream is particularly narrow.

Figure 4.10 shows the cumulative fraction of volumes which contain more than the given numbers of streams. Note that, as discussed above, not all streams are long and narrow, so Figure 4.10 provides an upper limit to the probability of detecting GD-1-like narrow streams within a few kiloparsecs from the Sun. Between 6 to 9 Gyr, half of the volumes contain about 5 to 10 streams, out of the 100 streams selected with maximum galactocentric distance of 30 kpc (Section 4.2.4), in both smooth and lumpy halos. In general, each volume in the lumpy cases (both $M_{sub} > 10^7 M_{\odot}$ and $M_{sub} > 5 \times 10^7 M_{\odot}$) contains one or two more streams than in the smooth case.

We repeat the same analysis using $d = 4$ kpc volumes. Because the individual volumes are now larger than shown in Figure 4.8, we can only fit 15 of them at 8 kpc away from the galactic center without significant overlap. The results are shown in the bottom of Figure 4.10. Because each individual volume is bigger, the cumulative counts are slightly higher than the counts with $d = 3$ kpc volumes. We did not repeat with other volume sizes in order to ensure each volume is large enough to contain reasonable numbers of stream segments, while fitting a reasonable number of volumes at 8 kpc without overlapping.

Velocity distributions

Figure 4.11 shows the 3D velocities of each stream segment in the volume in Figure 4.9 where each stream segment retains their color identification. The large dark blue segment prominent in the left hemisphere in Figure 4.9 again shows a large velocity dispersion, whereas the white, red, and brown stream segments have much lower dispersions.

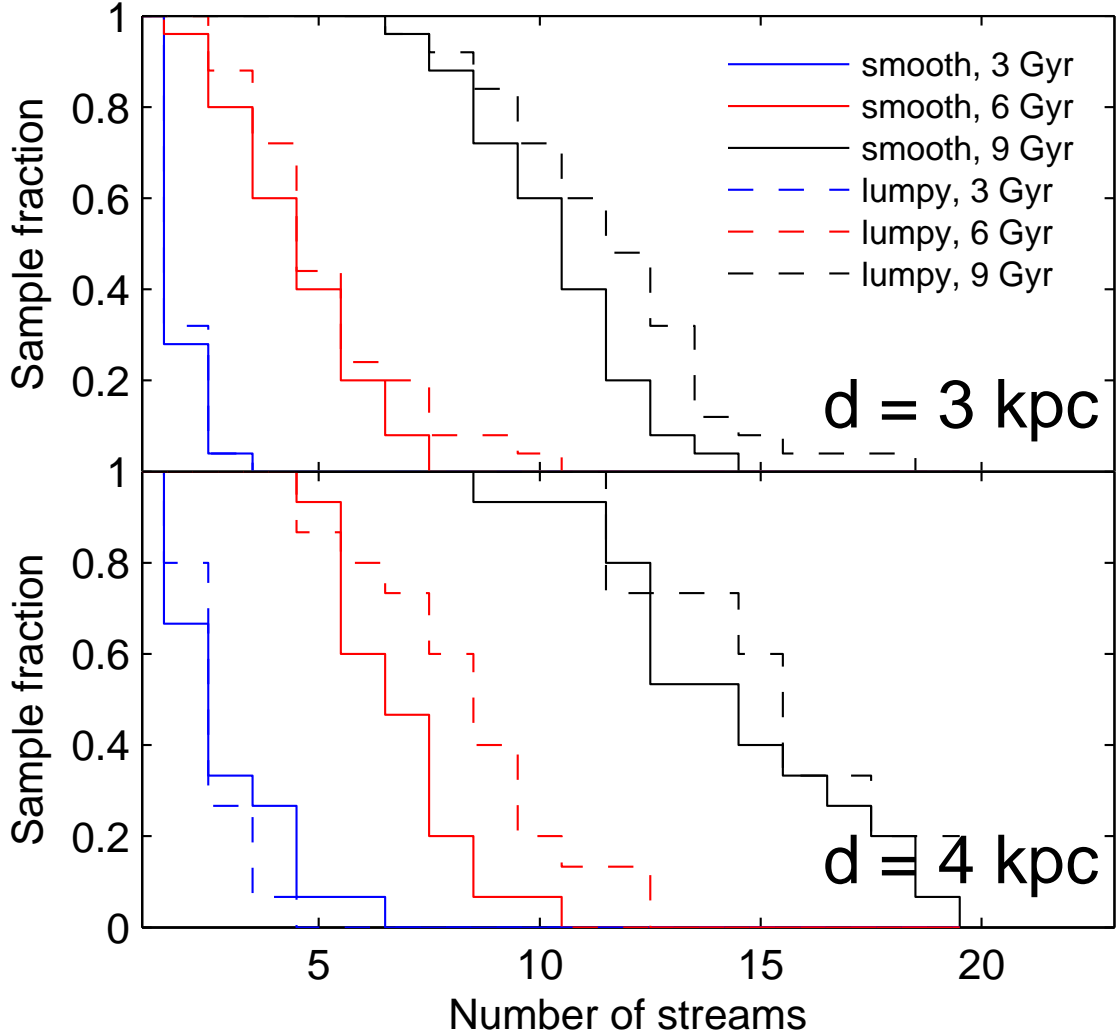


Figure 4.10: Cumulative fractions of spherical volumes as functions of the number of stream segments (with at least 20 particles) inside each volume. Note that in this study we only simulated 100 streams. The number of streams in observations will depend on the actual number of streams and their kinematical distributions in reality. Top and bottom panels use 25 volumes at $d = 3$ kpc each and 15 volumes at $d = 4$ kpc each, respectively. Solid and dashed lines represent the smooth and lumpy halos with $M_{sub} > 10^7 M_{\odot}$, respectively. The $M_{sub} > 5 \times 10^6 M_{\odot}$ case produces similar results to the $M_{sub} > 10^7 M_{\odot}$ case shown.

Each stream segment spans a finite volume of position space, so the velocity distribution of each stream has a gradient which is not aligned with the v_x, v_y, v_z axes in general, as shown in Figure 4.11. Instead of computing the velocity dispersions in v_x, v_y, v_z , we perform principal component analyses (PCA) on their 3D velocities. In three dimensions, PCA computes the three eigenvalues of the 3×3 covariance matrix of the three components in velocities. The eigenvalues represent the variances along the three principal components of the stream segment’s velocity distribution, so the square roots of the eigenvalues are the velocity dispersions along those components.

Figure 4.12 shows the distributions of the square roots of the smallest, second largest, and largest eigenvalues from the PCA of the 3D velocities of all the stream segments inside all the $d = 3$ kpc observable volumes in the lumpy halo ($M_{sub} > 5 \times 10^6 M_\odot$), which is the most complicated halo. Between 6 and 9 Gyr, the largest velocity dispersion (bottom panel) peaks at about 20 km s^{-1} . Approximating the halo with the spherical NFW profile with parameters mentioned in Section 4.2.2, the spread in orbital velocity in the halo at 8 ± 3 kpc is $\sim 36 \text{ km s}^{-1}$. Therefore, velocity dispersions on that order can be attributed to the velocity gradient along the stream. The smallest velocity dispersions (top panel of Figure 4.12), on the other hand, peak at below 10 km s^{-1} even at 9 Gyr. This suggests that cold streams with velocity dispersions at a few kilometers per second are likely to be found inside a local volume, even in a lumpy halo. The case of the smooth VL-2 halo, not shown in Figure 4.12, produces even lower velocity dispersions. This is expected as random encounters between a stream and subhalos would dynamically heat up the stream.

4.4 Chapter Summary

In this study we investigated the dispersal of tidal streams in both positions and velocities, which resulted from the disruption of a globular star cluster in four kinds of dark matter halos:

- (a) Spherical potential with no subhalos
- (b) Spherical potential with orbiting subhalos
- (c) Realistic potential with no subhalos
- (d) Realistic potential with orbiting subhalos

Both cases with subhalos (b and d) were further divided into two sub-cases with different subhalo mass ranges: (i) all subhalos with $M_{sub} > 10^7 M_\odot$, and (ii) all subhalos with $M_{sub} > 5 \times 10^6 M_\odot$. In all cases the main halo is a time independent potential constructed using the zeroth redshift snapshot of the high-resolution dark matter halo in the Via Lactea II (VL-2) simulation. The subhalos were extracted by a halo finder code from VL-2 and were also constructed as time independent potentials, but they orbited around the smooth potentials.

For each case above, we simulated 100 N-body streams whose progenitor orbits were restricted to be less than 30 kpc in the smooth potentials (while allowing subhalos to scatter the tidal debris to arbitrary distances) for 10 Gyr. Stream orbits were chosen randomly, but were divided into two groups: orbits that approached within less than 10 kpc from the galactic center (inner streams), and those that only orbit between 10 kpc and 30 kpc from the galactic center (outer streams).

For each stream we quantified the dispersal of the tidal debris by assigning all particles to their nearest grid cells, and we plotted the distributions of cell occupancies. We found that the shape of the

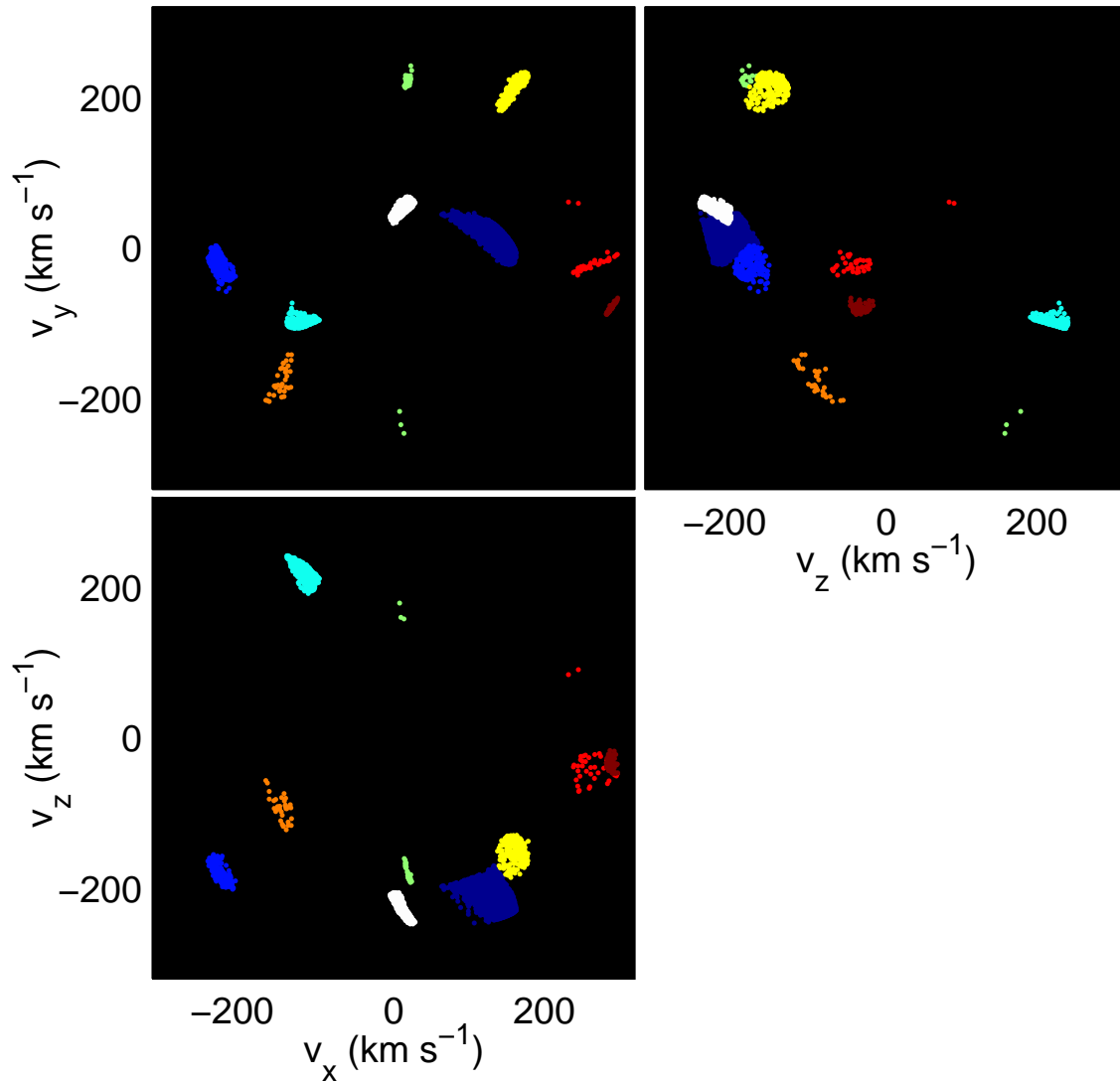


Figure 4.11: Projections of the 3D velocities of the 9 streams shown in Figure 4.9 with the same colors for each stream. The scatter of ~ 200 km s⁻¹ in the mean velocities of each stream is due to the variety in orbits. Clearly even very dispersed streams (eg. the dark blue stream in Figure 4.9) appear localized in velocity space of the local volume.

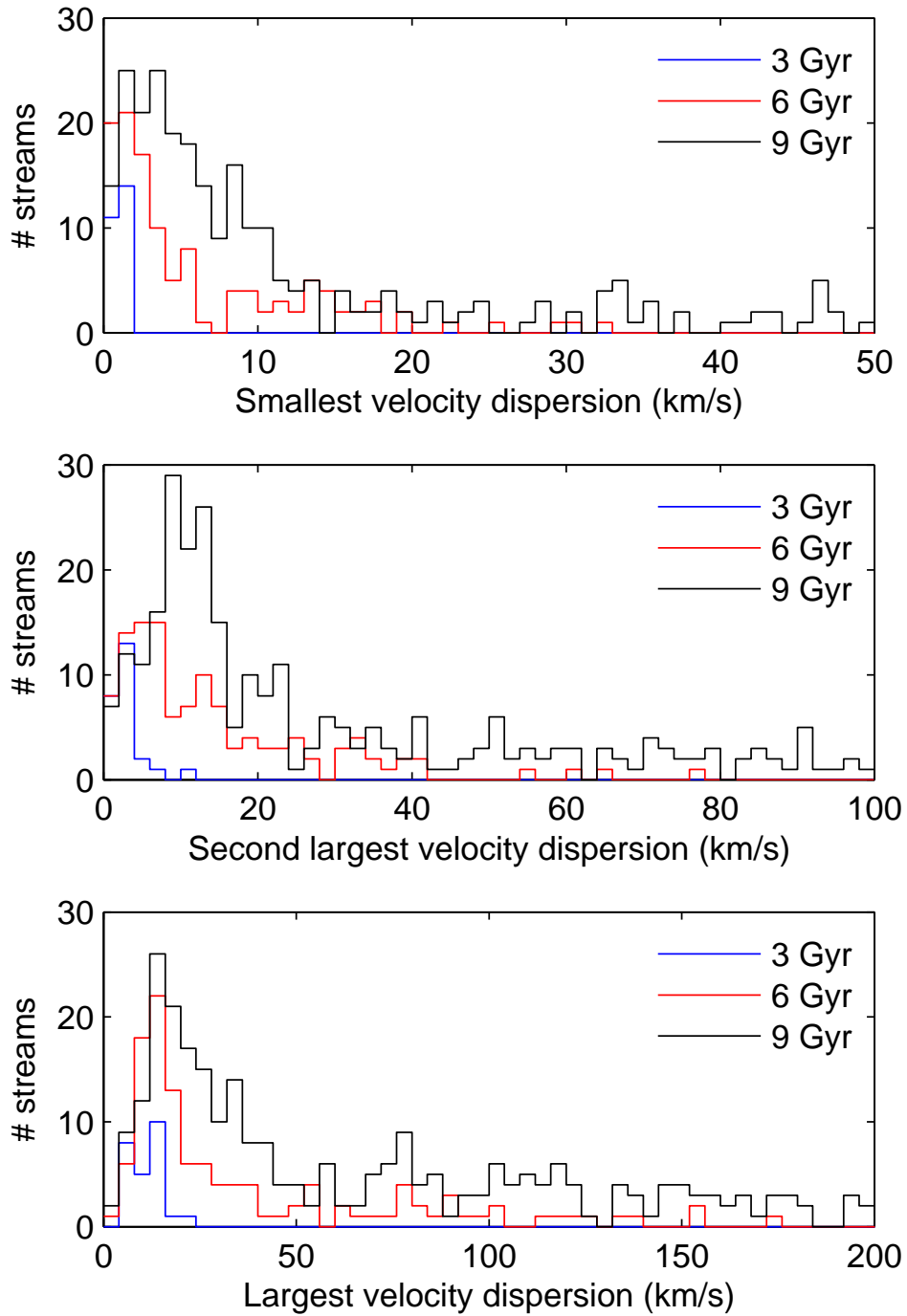


Figure 4.12: Distributions of the velocity dispersions in all stream segments inside all 25 $d = 3$ kpc volumes inside the lumpy VL-2 halo with $M_{sub} > 5 \times 10^6 M_{\odot}$. Top, middle, and bottom panels show the smallest, second largest, and the largest principal components (ie. square roots of the eigenvalues of the covariance matrix) of the 3D velocity distribution, respectively.

smooth halo affects the dispersal of tidal debris much more than subhalos do, similar to the conclusion of Siegal-Gaskins & Valluri (2008) which simulated the tidal disruptions of dwarf galaxies in larger orbits. Furthermore, we found that subhalos with $M_{sub} > 10^7 M_{\odot}$ can render streams denser, hence potentially more easily detectable, by bunching up stream stars into clumps which were denser than streams in the smooth halo. Meanwhile, subhalos with $M_{sub} > 5 \times 10^6 M_{\odot}$ produced almost the same distribution of cell occupancies as the $M_{sub} > 10^7 M_{\odot}$ case. Therefore, subhalos with masses below $10^7 M_{\odot}$ are not important for dispersing tidal debris.

We selected a few streams which produced the highest cell occupancies in the VL-2 halo in order to study the streams' morphologies. In the smooth halo, the densest parts of the streams were results of transverse compression as the streams passed through the pericenters of their orbits. In the lumpy halo, however, the densest parts of the streams can be either compressed segments similar to the streams in the smooth halo, but the densest parts can also be clumps of particles caused by subhalo perturbations. Evidently even streams with eccentricity of ~ 0.6 can retain their narrow shape.

Finally, we studied the velocity dispersions in stream segments inside small observable volumes, each centered at 8 kpc away from the galactic center of the VL-2 halos. These volumes, at $d = 3$ or 4 kpc in radius, represent the volume in which high-resolution 3D velocities of stars can be measured in the near future. Of the 100 streams in our orbital distribution, we found a median of 5 to 15 stream segments inside each volume. The velocity dispersions of these stream segments can also be as low as a few kilometers per second. Therefore, even in a realistic and lumpy halo, cold and thin streams similar to GD-1 can survive for a Hubble time and can be observed at 8 kpc away from the galactic center.

While our N-body streams are orbiting realistic halo potentials, our simulations are still missing a few effects. In addition to a dark matter halo, the Milky Way also has a baryonic galaxy which can be dynamically important near the galactic center. The inner streams, which approach within 10 kpc from the galactic center, are likely affected more severely than the outer streams beyond 10 kpc. Furthermore, other than the subhalos' orbits, all our potentials are static since we constructed them using only the redshift zero snapshot. In the hierarchical structure formation model, satellite systems are continuously accreted and merged into the main halo. Therefore, we expect both the main halo and the subhalos to be evolving in time. Finally, we selected our stream orbits randomly in both position and velocity, which likely resulted in an unrealistic distribution of orbits. Current surveys such as Gaia will be very valuable in providing detailed information of kinematics of globular clusters and streams in the Milky Way for future studies.

Chapter 5

Conclusions and Future Work

5.1 Conclusions

Gaps in stellar tidal streams can be a powerful probe to measure the abundance of dark matter subhalos, whose existence is a fundamental prediction of the Λ CDM model. The method relies on the dynamical influences of the subhalos, rather than directly detecting luminous content inside the subhalos which may be very little. Observations of tidal streams show that some streams indeed have longitudinal variations in density. However, numerical experiments prior to this thesis have only employed idealized models, which may have neglected many effects in realistic streams, making the results premature for direct comparison against observations. In this thesis we investigated some of those realistic effects.

Chapter 2 (Ngan & Carlberg, 2014) focused on isolating the intrinsic effects other than subhalo perturbations which can also produce gaps in streams. We simulated the disruption of a self-gravitating star cluster that forms a stream with and without interacting with subhalos. This allowed us to characterize the effects such as epicyclic overdensities which also appears as gaps in streams that can otherwise be confused with subhalo perturbations. We found that the distribution of gap lengths, or the gap spectrum, can be used to distinguished between intrinsic gaps and subhalo gaps.

Chapter 3 (Ngan et al., 2015) presented the method to construct the time-independent potentials directly from the zero redshift snapshot of a high-resolution dark matter halo, with and without its subhalos, inside a cosmological simulation. We then simulated self-gravitating star clusters inside these two realistic potentials. This allowed us to isolate the effects that the realistic halos have on the stream and its gaps. We found that streams in a realistic halo can exhibit more complicated morphologies than in an idealized halo.

Chapter 4 demonstrated the importance of using realistic potentials (Ngan et al., 2015) compared to the idealized potentials (Ngan & Carlberg, 2014) by simulating 100 self-gravitating streams in each case. We compared the spatial and velocity dispersions of the streams in idealized and realistic halos. Our results indicated that although streams are more dispersed in realistic halos, many cold and thin streams can still survive for a Hubble time and can be found near the solar circle.

Our findings in Chapter 4 is particularly important for the future of using stream gaps as a probe for subhalos. As discussed in the Section 4.3.4, a star that is dimmer than $M_V = +4$ at 3 kpc away would have high velocity errors, and this can impact the member identification of cold streams by Gaia kinematics. Therefore, in order to be able to use more streams to detect subhalos, we must either rely on

streams that are no more than a few kpc away from us, or be extremely careful at selecting streams with very low signal-to-noise ratios. The latter requires further studies, as we suggest in the next section.

5.2 Future Work

The contributions in this thesis consist of two improvements over the state-of-the-art of modeling stream gaps: self-gravitating streams and a realistic halo potential. One way to determine whether the longitudinal density variation along observed streams is truly due to subhalos or other unrelated effects is to see if the gap spectrum of simulation and observations match, as discussed in Ngan & Carlberg (2014). The gap spectrum for GD-1 has already been measured (Carlberg & Grillmair, 2013) and briefly compared against our simulations in Section 2.4.4, but the comparison was not conclusive because our models did not include some known effects, which we summarize in this section.

Progenitor modeling: Throughout this thesis, we simulated streams that originated from two progenitor star clusters. Although the star clusters were self-gravitating, they were collisionless models where the two body relaxation time scales are much greater than a Hubble time. Also, the mass per particle in the streams did not necessarily correspond to realistic masses of stars. Therefore, the resulting streams were only similar to but were not meant to be physical models of GD-1, whose gap spectrum has been measured. As illustrated by Carlberg (2012), Carlberg (2013), and Erkal & Belokurov (2015), dynamics of stream gaps depend sensitively on the velocity dispersion of the stream, which in turn depend on the progenitor. A rigorous prediction of gap spectrum likely requires understanding of how it depends on the stream progenitor.

Observational modeling: We have used all three positions and all three velocities in analysing our streams. However, as pointed out in Chapter 4, not all information is available to us with reasonable accuracy. It may be necessary to extend the observational considerations similar to Ngan & Carlberg (2014) by not only discarding particles, but also discarding phase space information (eg. without distances or proper motion). An even more realistic model would involve synthetically contaminating the information by adding foreground and background stars in order to test how well the streams itself and its gaps can be recovered.

Baryonic galaxy: The potentials throughout this thesis, be it the spherical halo in Ngan & Carlberg (2014) and Chapter 4 or the realistic halo in Ngan et al. (2015) and Chapter 4, are all based on dark matter halos which do not include the baryonic galaxy. For the Milky Way, the galaxy is represented by a disk and a bulge potential which can be important near the inner regions of the galaxy. Therefore, our stream models do not account for disk shocking, which can affect the dispersions and longitudinal density variations along streams (Dehnen et al., 2004). Since the gravity on a stream is dominated by the dark matter halo, and the bulge and the disk should only provide brief shocks to the stream, high resolution models of the bulge and the disk may not be necessary. Many studies have adopted the model described in Allen & Santillan (1991) which combine three analytical components representing a halo, a bulge, a disk such that the resulting potential is consistent with kinematics in the Milky Way. The bulge and disk components can be easily adapted into our simulations.

Time-dependent potential: The formation of a tidal stream takes roughly the same amount of time as the collapse of a Milky-Way-sized dark matter halo, which is of the order of a Hubble time. During that time, the entire potential in the halo is evolving. Although our realistic halo potentials in Ngan et al. (2015) and Chapter 4 are constructed from a cosmological simulation, they are only the redshift zero snapshots. As the underlying halo accretes mass, subhalos are also continuously accreted and disrupted. Therefore, not only is the underlying potential (hence the orbits of streams and subhalos) evolving, but the potentials of the subhalos as well as their abundance are also evolving. In order to construct a time-dependent potential from VL-2, the snapshots at higher redshifts must also be used. The dynamics of stream gaps in a time-dependent and realistic potential have yet to be explored.

Bibliography

- Allen, C., & Santillan, A. 1991, *Revista Mexicana de Astronomia y Astrofisica*, 22, 255
- Bardeen, J. M., Bond, J. R., Kaiser, N., & Szalay, A. S. 1986, *ApJ*, 304, 15
- Barkana, R., Haiman, Z., & Ostriker, J. P. 2001, *ApJ*, 558, 482
- Belokurov, V., Zucker, D. B., Evans, N. W., et al. 2006, *ApJL*, 642, L137
- Benson, A. J., Frenk, C. S., Lacey, C. G., Baugh, C. M., & Cole, S. 2002, *MNRAS*, 333, 177
- Benson, A. J., Farahi, A., Cole, S., et al. 2013, *MNRAS*, 428, 1774
- Bernard, E. J., Ferguson, A. M. N., Schlafly, E. F., et al. 2014, *MNRAS*, 443, L84
- Binney, J., & Tremaine, S. 2008, *Galactic Dynamics: Second Edition* (Princeton University Press)
- Blumenthal, G. R., Faber, S. M., Primack, J. R., & Rees, M. J. 1984, *Nature*, 311, 517
- Bode, P., Ostriker, J. P., & Turok, N. 2001, *ApJ*, 556, 93
- Bonaca, A., Geha, M., Küpper, A. H. W., et al. 2014, *ApJ*, 795, 94
- Boylan-Kolchin, M., Bullock, J. S., & Kaplinghat, M. 2011, *MNRAS*, 415, L40
- Bullock, J. S. 2010, *ArXiv e-prints*, arXiv:1009.4505
- Bullock, J. S., & Johnston, K. V. 2005, *ApJ*, 635, 931
- Bullock, J. S., Kravtsov, A. V., & Weinberg, D. H. 2000, *ApJ*, 539, 517
- Carlberg, R. G. 2009, *ApJL*, 705, L223
- . 2012, *ApJ*, 748, 20
- . 2013, *ApJ*, 775, 90
- Carlberg, R. G., & Grillmair, C. J. 2013, *ApJ*, 768, 171
- Carlberg, R. G., Grillmair, C. J., & Hetherington, N. 2012, *ApJ*, 760, 75
- Cole, D. R., Dehnen, W., & Wilkinson, M. I. 2011, *MNRAS*, 416, 1118
- Cole, S., Percival, W. J., Peacock, J. A., et al. 2005, *MNRAS*, 362, 505
- Comparetta, J., & Quillen, A. C. 2011, *MNRAS*, 414, 810

- Davis, M., Efstathiou, G., Frenk, C. S., & White, S. D. M. 1985, *ApJ*, 292, 371
- de Blok, W. J. G., Bosma, A., & McGaugh, S. 2003, *MNRAS*, 340, 657
- de Bruijne, J. H. J. 2012, *Ap&SS*, 341, 31
- Dehnen, W., Odenkirchen, M., Grebel, E. K., & Rix, H.-W. 2004, *AJ*, 127, 2753
- Diemand, J., Kuhlen, M., Madau, P., et al. 2008, *Nature*, 454, 735
- Diemand, J., & Moore, B. 2011, *Advanced Science Letters*, 4, 297
- Eisenstein, D. J., Zehavi, I., Hogg, D. W., et al. 2005, *ApJ*, 633, 560
- Erkal, D., & Belokurov, V. 2015, *MNRAS*, 450, 1136
- Eyre, A., & Binney, J. 2011, *MNRAS*, 413, 1852
- Grillmair, C. J. 2010, in *Galaxies and their Masks*, ed. D. L. Block, K. C. Freeman, & I. Puerari, 247
- Grillmair, C. J. 2014, *ApJL*, 790, L10
- Grillmair, C. J., & Dionatos, O. 2006, *ApJL*, 643, L17
- Harding, P., Morrison, H. L., Olszewski, E. W., et al. 2001, *AJ*, 122, 1397
- Harris, W. E. 1996, *AJ*, 112, 1487
- Helmi, A., White, S. D. M., & Springel, V. 2003, *MNRAS*, 339, 834
- Hernquist, L. 1990, *ApJ*, 356, 359
- Hernquist, L., & Ostriker, J. P. 1992, *ApJ*, 386, 375
- Hernquist, L., Sigurdsson, S., & Bryan, G. L. 1995, *ApJ*, 446, 717
- Hinshaw, G., Spergel, D. N., Verde, L., et al. 2003, *ApJS*, 148, 135
- Hu, W., & Dodelson, S. 2002, *Annual Review of Astronomy and Astrophysics*, 40, 171
- Hu, W., & Sugiyama, N. 1995, *ApJ*, 444, 489
- . 1996, *ApJ*, 471, 542
- Ibata, R. A., Lewis, G. F., Irwin, M. J., & Quinn, T. 2002, *MNRAS*, 332, 915
- Jing, Y. P., & Suto, Y. 2002, *ApJ*, 574, 538
- Johnston, K. V. 1998, *ApJ*, 495, 297
- Johnston, K. V., Sackett, P. D., & Bullock, J. S. 2001, *ApJ*, 557, 137
- Johnston, K. V., Spergel, D. N., & Haydn, C. 2002, *ApJ*, 570, 656
- Just, A., Berczik, P., Petrov, M. I., & Ernst, A. 2009, *MNRAS*, 392, 969
- Kamionkowski, M., & Liddle, A. R. 2000, *Physical Review Letters*, 84, 4525

- Klypin, A., Kravtsov, A. V., Valenzuela, O., & Prada, F. 1999, *ApJ*, 522, 82
- Knollmann, S. R., & Knebe, A. 2009, *ApJS*, 182, 608
- Koposov, S. E., Irwin, M., Belokurov, V., et al. 2014, *MNRAS*, 442, L85
- Koposov, S. E., Rix, H.-W., & Hogg, D. W. 2010, *ApJ*, 712, 260
- Koposov, S. E., Yoo, J., Rix, H.-W., et al. 2009, *ApJ*, 696, 2179
- Küpper, A. H. W., Kroupa, P., Baumgardt, H., & Heggie, D. C. 2010, *MNRAS*, 401, 105
- Küpper, A. H. W., Lane, R. R., & Heggie, D. C. 2012, *MNRAS*, 420, 2700
- Küpper, A. H. W., MacLeod, A., & Heggie, D. C. 2008, *MNRAS*, 387, 1248
- Law, D. R., Johnston, K. V., & Majewski, S. R. 2005, *ApJ*, 619, 807
- Law, D. R., Majewski, S. R., & Johnston, K. V. 2009, *ApJL*, 703, L67
- Lowing, B., Jenkins, A., Eke, V., & Frenk, C. 2011, *MNRAS*, 416, 2697
- Lux, H., Read, J. I., Lake, G., & Johnston, K. V. 2013, *MNRAS*, 436, 2386
- Macciò, A. V., Kang, X., Fontanot, F., et al. 2010, *MNRAS*, 402, 1995
- Madau, P., Diemand, J., & Kuhlen, M. 2008, *ApJ*, 679, 1260
- Madau, P., Shen, S., & Governato, F. 2014, *ApJL*, 789, L17
- Martin, N. F., Ibata, R. A., Rich, R. M., et al. 2014, *ApJ*, 787, 19
- Moore, B., Ghigna, S., Governato, F., et al. 1999, *ApJL*, 524, L19
- Navarro, J. F., Frenk, C. S., & White, S. D. M. 1997, *ApJ*, 490, 493
- Navarro, J. F., Hayashi, E., Power, C., et al. 2004, *MNRAS*, 349, 1039
- Navarro, J. F., Ludlow, A., Springel, V., et al. 2010, *MNRAS*, 402, 21
- Neto, A. F., Gao, L., Bett, P., et al. 2007, *MNRAS*, 381, 1450
- Ngan, W., Bozek, B., Carlberg, R. G., et al. 2015, *ApJ*, 803, 75
- Ngan, W. H. W., & Carlberg, R. G. 2014, *ApJ*, 788, 181
- Odenkirchen, M., Grebel, E. K., Kayser, A., Rix, H.-W., & Dehnen, W. 2009, *AJ*, 137, 3378
- Odenkirchen, M., Grebel, E. K., Rockosi, C. M., et al. 2001, *ApJL*, 548, L165
- Ogiya, G., & Burkert, A. 2015, *MNRAS*, 446, 2363
- Pearson, S., Küpper, A. H. W., Johnston, K. V., & Price-Whelan, A. M. 2015, *ApJ*, 799, 28
- Penzias, A. A., & Wilson, R. W. 1965, *ApJ*, 142, 419
- Perlmutter, S., Aldering, G., Goldhaber, G., et al. 1999, *ApJ*, 517, 565

- Planck Collaboration, Ade, P. A. R., Aghanim, N., et al. 2014, *A&A*, 571, A15
- Pontzen, A., & Governato, F. 2012, *MNRAS*, 421, 3464
- Price-Whelan, A. M., Johnston, K. V., Valluri, M., et al. 2015, ArXiv e-prints, arXiv:1507.08662
- Riess, A. G., Filippenko, A. V., Challis, P., et al. 1998, *AJ*, 116, 1009
- Schneider, A., Smith, R. E., & Reed, D. 2013, *MNRAS*, 433, 1573
- Sesar, B., Bovy, J., Bernard, E. J., et al. 2015, ArXiv e-prints, arXiv:1501.00581
- Siegal-Gaskins, J. M., & Valluri, M. 2008, *ApJ*, 681, 40
- Spergel, D. N., & Steinhardt, P. J. 2000, *Physical Review Letters*, 84, 3760
- Spergel, D. N., Verde, L., Peiris, H. V., et al. 2003, *ApJS*, 148, 175
- Springel, V. 2005, *MNRAS*, 364, 1105
- Springel, V., Frenk, C. S., & White, S. D. M. 2006, *Nature*, 440, 1137
- Springel, V., White, S. D. M., Jenkins, A., et al. 2005, *Nature*, 435, 629
- Springel, V., Wang, J., Vogelsberger, M., et al. 2008, *MNRAS*, 391, 1685
- Strigari, L. E., Bullock, J. S., Kaplinghat, M., et al. 2008, *Nature*, 454, 1096
- Swaters, R. A., Madore, B. F., van den Bosch, F. C., & Balcells, M. 2003, *ApJ*, 583, 732
- Tegmark, M., Blanton, M. R., Strauss, M. A., et al. 2004, *ApJ*, 606, 702
- Vogelsberger, M., Zavala, J., & Loeb, A. 2012, *MNRAS*, 423, 3740
- Vogelsberger, M., Zavala, J., Simpson, C., & Jenkins, A. 2014, *MNRAS*, 444, 3684
- Willett, B. A., Newberg, H. J., Zhang, H., Yanny, B., & Beers, T. C. 2009, *ApJ*, 697, 207
- Yoon, J. H., Johnston, K. V., & Hogg, D. W. 2011, *ApJ*, 731, 58
- Zemp, M., Diemand, J., Kuhlen, M., et al. 2009, *MNRAS*, 394, 641